



Technische Universität München

Fakultät für Physik

Nature of Space Charge Layers in Li^+ Conducting Glass Ceramics

Leon Markus Katzenmeier

Vollständiger Abdruck der von der Fakultät für Physik der Technischen Universität München zur Erlangung des akademischen Grades eines Doktors der Naturwissenschaften (Dr. rer. nat.) genehmigten Dissertation.

Vorsitzende: Prof. Dr. Nora Brambilla

Prüfer der Dissertation:

1. Prof. Dr. Aliaksandr S. Bandarenka
2. Prof. Dr. Ian Sharp

Die Dissertation wurde am 11.04.2022 bei der Technischen Universität München eingereicht und durch die Fakultät für Physik am 29.06.2022 angenommen.

Abstract

The nature of space charge layers (SCLs) formed in solid-state electrolytes (SSEs) at contact with different materials has been debated since the discovery of oxygen-ion conducting solids. With the advent of lithium-based all-solid-state batteries (ASSBs), the phenomenon regained attention in the scientific community as a possible origin of the high interfacial resistance between the SSE and the electrode. A variety of theoretical approaches based on thermodynamics or electrochemistry have not shown a conclusive picture of the SCL phenomenon. Moreover, experimental evidence is hard to come by, typically employing methods that require impractical sample sizes or geometries. In this work, the asymmetric growth of the SCLs upon increasing the bias potential at the SSE/electrode is directly observed with an optical method, namely spectroscopic ellipsometry, and further characterized by impedance spectroscopy. Further electrochemical and physical properties, such as ionic resistance, are determined. A physical model describing the impedance response of an SSE in blocking conditions has been elaborated. This model was further used to investigate the change of SCL resistance under temperature variation. This resistance reveals a significant increase in activation energy for the Li^+ transport compared to the bulk electrolyte. Finally, a kinetic Monte Carlo simulation was used to estimate the SCL thickness. The obtained results not only match the experimentally observed values, but the model also naturally reflects the asymmetry of the SCL formation.

Zusammenfassung

Die Formierung von Raumladungszonen in Festkörperelektrolyten bei Kontakt mit anderen Materialien wurde bereits mit der Entdeckung von Sauerstoff-Ionen leitenden Materialien debattiert. Heutzutage sind Lithium basierte Festkörperelektrolyte insbesondere für Festkörperbatterien von Interesse und das Phänomen der Raumladung wird als mögliche Ursache für den hohen Grenzflächenwiderstand zwischen dem Elektrolyten und der Elektrode diskutiert. Verschiedene Ansätze zur theoretischen Modellierung, thermodynamisch oder elektrochemisch, haben bisher nicht zu einer schlüssigen Darstellung geführt. Zudem waren experimentelle Beweise für Raumladungszonen bisher auf Proben beschränkt die keine elektrochemische Charakterisierung zugelassen haben. In dieser Arbeit wurde das asymmetrische Wachstum von Raumladungszonen in einem Modellmaterialsystem mit einer optischen Methode, spektroskopischer Ellipsometrie, direkt nachgewiesen und mit Impedanzspektroskopie weiter untersucht. Die elektrochemischen Eigenschaften, wie z.B. der Widerstand, wurden mittels elektrochemischer Impedanzspektroskopie bestimmt. Ein physikalisches Ersatzschaltbild für die Impedanzantwort der Raumladungszone in einem Festkörperelektrolyten wurde entwickelt und validiert. Der Einfluss der Temperatur auf den Widerstand lässt auf die eine signifikante Erhöhung der Aktivierungsenergie im Vergleich zum Bulkelektrolyten schließen. Abschließend wird ein kinetisches Monte Carlo Modell mit den physikalischen Messergebnissen parametrisiert, wobei sich sowohl die Asymmetrie als auch die Dicken der Raumladungszonen in den Simulationen unmissverständlich widerspiegeln.

List of Publications.

Horowitz, Y., Schmidt, C., Yoon, D. H., Riegger, L. M., **Katzenmeier, L.**, Bosch, G. M. & Golodnitsky, D. (2020). Between Liquid and All Solid: A Prospect on Electrolyte Future in Lithium-Ion Batteries for Electric Vehicles. *Energy Technology*, 8(11), 2000580.

Katzenmeier, L., Helmer, S., Braxmeier, S., Knobbe, E., & Bandarenka, A. S. (2021). Properties of the Space Charge Layers Formed in Li-Ion Conducting Glass Ceramics. *Applied Materials & Interfaces*, 13(4), 5853-5860.

Katzenmeier, L., Carstensen, L., Schaper, S. J., Müller-Buschbaum, P., & Bandarenka, A. S. (2021). Characterization and Quantification of Depletion and Accumulation Layers in Solid-State Li⁺-Conducting Electrolytes Using In Situ Spectroscopic Ellipsometry. *Advanced Materials*, 2100585.

Watzel, S. A., **Katzenmeier, L.**, Sabawa, J. P., Garlyyev, B., & Bandarenka, A. S. (2021). Temperature dependences of the double layer capacitance of some solid/liquid and solid/solid electrified interfaces. An experimental study. *Electrochimica Acta*, 391, 138969.

Gaddam, R., **Katzenmeier, L.**, Lamprecht, X., & Bandarenka, A. S. (2021). Review on physical impedance models in modern battery research. *Physical Chemistry Chemical Physics*, 23, 12926.

Katzenmeier, L., Carstensen, L., Bandarenka A.S. (2022). Li⁺ conductivity of space charge layers formed at electrified interfaces between a model solid-state electrolyte and blocking Au-electrodes. *ACS Applied Materials and Interfaces*, 14, accepted.

Conference Contributions.

Oral Presentation, Katzenmeier, L., Bandarenka, A. S., Space charge Layers in Solid-State Electrolytes: reconciling models and experiments., German-Isreali-Battery School, Berlin, Germany, May 13, 2019 – May 15, 2019.

Poster, Katzenmeier, L., Bandarenka, A. S., Space charges in Solid-State Electrolytes: negligible impact?, 9th Energy Colloquium of the Munich School of Engineering, Garching, Germany, Aug 1, 2019.

Poster, Katzenmeier, L., Bandarenka, A. S., Evidences of the Space charge Layer Formation in Li-Conducting Solid-State Electrolytes., 71st Annual Meeting of the International Society of Electrochemistry. Online event, Aug 31, 2020 – Sep 4, 2020.

Poster, Katzenmeier, L., Bandarenka, A. S., The Nature of Space charge in Solid-State Electrolytes., 72nd Annual Meeting of the International Society of Electrochemistry. Online event, Aug 31, 2021 – Sep 4, 2021.

Poster, Katzenmeier, L., Bandarenka, A. S., The Nature of Space charge in Solid-State Electrolytes., Suncat Summer Institute. Online event, Aug 16, 2021 – Aug 19, 2021.

Flash Presentation, Katzenmeier, L., Bandarenka, A. S., Space charge in Solid-State Electrolytes., International Center for Mechanical Science – Batteries., Udine, Italy. Sep 20, 2021 – Sep 24, 2021.

Oral Presentation, Katzenmeier, L., Kaye, M., Bandarenka, A. S., Space charge in Li-conducting Solid-State Electrolytes: the key to parameterize mobile ion concentrations?, 30th Topical Meeting of the International Society of Electrochemistry. Online event, Nov 22, 2021 – Nov 24, 2021.

Flash Presentation, Katzenmeier, L., Bandarenka, A. S., The Nature of Space charge in Solid-State Electrolytes, 12th International Symposium on Electrochemical Impedance Analysis. Online event, Nov 29, 2021 – Nov 30, 2021.

Poster, Katzenmeier, L, Carstensen, L., Bandarenka, A. S., Space charge in solid-state electrolytes – charge depletion at the metal/solid-state electrolyte interface, Batterieforum. Online event, Jan 19&25, Feb 2&8, 2022.

Table of Contents.

<i>List of Publications</i>	5
<i>Conference Contributions</i>	6
<i>Table of Contents</i>	8
1 Introduction and Literature Overview	10
2 Theory of Solid-State Electrolytes and Space Charge Regions	20
2.1 Solid-State Electrolytes and Ionic Concentrations.....	20
2.2 Fundamental Electrochemical Considerations.....	23
2.3 Space Charge in Semiconductors and Ionic Conductors.....	26
2.4 Semi-Analytical Space Charge Layer Modeling.....	32
2.5 Mott-Schottky Theory.....	38
3 Electrochemical Impedance Spectroscopy and the Importance of a Physical Model	40
3.1 Working Principle of Electrochemical Impedance Spectroscopy.....	42
3.2 Stationarity, Linearity and the Kramers-Kronig relations.....	46
3.3 Electrical Equivalent Circuits.....	48
4 Spectroscopic Ellipsometry and Optical Modeling	51
4.1 Light Polarization and Reflection.....	51
4.2 Optical Properties and Modeling.....	54
4.3 Working Principle of Spectroscopic Ellipsometry.....	57
5 Experimental Setups and Materials	59
5.1 A Model Solid-State Electrolyte: Ohara LICGC™.....	59
5.2 Electrode Fabrication.....	59
5.3 Impedance Setup and Analysis.....	60
5.4 Electrochemical Cell Setup.....	60
5.5 Optical Measurements.....	61
6 Investigation of Space Charge Layers in Solid-State Electrolytes	63
6.1 Measuring the Spatial Extent with Spectroscopic Ellipsometry.....	63
6.2 Determining Electrochemical Properties with Electrochemical Impedance Spectroscopy... 70	70
6.3 Temperature Dependence of Space Charge Layer Properties.....	79
6.4 Determining Ion Concentrations using a Modified Mott-Schottky Approach.....	86
6.5 Parameterization and Validation of a Kinetic Monte-Carlo Model.....	92

7	<i>Conclusion & Outlook</i>	98
8	<i>Acknowledgements</i>	101
9	<i>Appendix</i>	103
9.1	Copyright Clearances	103
9.2	Temperature Dependency of the Double Layer Capacitance	105
9.3	Visualizing SCLs with Spectroscopic Ellipsometry	111
9.4	Electrochemical Properties of Negative SCLs	118
10	<i>Table of Figures</i>	126
11	<i>Literature</i>	129

1 Introduction and Literature Overview.

In a world with ever-increasing energy demand and the climate crisis manifesting its dire consequences in global warming, the storage of energy is becoming more important every day. With renewable energy production, like wind energy and solar photovoltaic, on the rise (3 % from Q1 2019 to Q1 2020),¹ the question of energy storage has gained increasing attention over the last decade. Both stationary and non-stationary solutions are required, and consequently, the field of battery technology is growing rapidly. Stationary global energy storage facilities are expected to increase by a total storage capacity of 1000 gigawatt-hours by 2030, as reported by Bloomberg NEF.² While the emerging technologies for stationary storage are most likely no longer based on lithium,³ with more abundant elements such as sodium⁴ as a successor, the search for a suitable replacement for the lithium-ion battery (LiB) technology for non-stationary storage is still ongoing. Without a doubt, the requirements for mobile energy storage strongly depend on the application ranging from micro-batteries for implantable medical devices,⁵ across communication devices,⁶ to larger batteries for battery electric vehicles (BEVs).⁷

Batteries, conceptually speaking, store energy in chemical bonds, which can be turned into electrical energy during discharging. The electrical energy is supplied externally and converted to chemical energy during charging. All of this is accompanied by the movement of ions from one material to another, driven by an electrochemical potential difference. One can consider for many types of batteries that the anode, with a low redox potential, is filled with certain ions in the charged state, while the cathode, a material with a high redox potential, is depleted of those ions. The ions move from anode to cathode during discharging through a part of the battery, which selectively transports ions, but not electrons. The electrons are forced to move via the external circuit where a load can be inserted to employ the potential difference and the current flow to power the electrical devices. In almost all traditional battery technologies, the part of the battery separating the anode and cathode consists of two materials: a separator and the electrolyte. Together, these parts ensure the physical separation of the electrodes while maintaining an ionic pathway.

The invention of today's prevailing battery technology has recently been rewarded with the Nobel Prize in Chemistry.⁸ The LiB is often based on a graphite anode with a theoretical capacity of 372

mAh/g,⁹ an intercalation cathode,¹⁰ and a liquid electrolyte. Although the original technology was first described in 1991,¹¹ more than 30 years ago, the material types used for modern batteries are still the same.¹² Approaching the theoretical limits of today's LiB technology, researchers have started to explore alternative materials and cell concepts. For anodes, the "holy grail" of materials is the Li-metal anode with a theoretical specific capacity of 3861 mAh/g and the lowest redox potential of -3.04 V vs. standard hydrogen electrode.^{13,14} However, major safety concerns are associated with the use of lithium metal due to the formation of needle-like structures called 'dendrites' during plating and stripping reactions on the electrodes.^{15,16} Several mitigation strategies have been proposed, such as using specific charging and discharging profiles,¹⁷ alteration of the electrolyte composition,¹⁸ desolvation kinetics,¹⁹ and, most prominently, a replacement of the liquid electrolyte with a more rigid structure, such as a polymer or a solid-state electrolyte (SSE).²⁰ SSEs could effectively enable a Li-metal anode by posing an impenetrable barrier to dendrites.^{21,22} The concept of SSEs, although not for Li⁺, was introduced as early as 1853 with the discovery of the galvanic SSE gas cell by J. M. Gaugain.²³ Ceria-based SSEs were developed early on for use in Solid Oxide Fuel Cells (SOFCs).²⁴ For the application in All-Solid-State Batteries (ASSBs), the SSE must fulfill several requirements: (i) sufficient ionic conductivity,²⁵ (ii) impenetrability to lithium dendrites,²⁶ (iii) stability vs. cathode materials,²⁷ (iv) no degradation of the bulk electrolyte during the charge/discharge cycles,²⁸ and (v) stability vs. metallic Li.²⁹ Extensive research efforts have mitigated the issues caused by aspects (i) – (iv), e.g., recently found SSEs are approaching the ionic conductivity of liquid electrolytes.³⁰

Conduction mechanisms

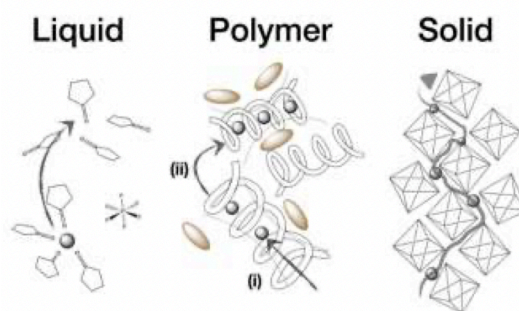


Figure 1. Schematic of the different ion conduction phenomena in liquid, (solid) polymer, and inorganic solid-state electrolytes. The ionic movement in polymers happens within (i) or between (ii) the polymer chains. In SSEs, ionic conduction often occurs via ion transport along crystallographic pathways. *Graph adapted from Energy Technology, 2020, 8(11), 2000580, The Authors. Energy Technology published by Wiley-VCH GmbH.*

For the application in ASSBs, three different material groups are relevant:³¹ inorganic sulfides or oxides and organic polymers. The different ion conduction mechanisms are sketched in **Figure 1**. In 2001, R. Kanno and co-workers introduced a new crystalline material family, the thio-LISICON (Lithium Super Ionic Conductor),³² which has been treated as one of the most promising candidates for ASSBs.³³ This is one of the prime examples of sulfide electrolytes,³⁴ which can form stable interfaces with anode and cathode materials³⁵ and exhibit good ionic conductivities.³⁶ However, they are typically too soft to effectively prevent dendrite penetration,³⁷ leading to various efforts to prevent the dendrites from forming in the first place.^{38,39} Oxide-based materials, such as the NASICON (Sodium Super Ionic Conductor)-type, originally developed for sodium-ion conductors,⁴⁰ are another class of SSEs that could be used in ASSBs.^{41,42} Vithal and co-workers⁴³ reviewed a range of NASICON materials with glassy and crystalline structures. With the higher mechanical stability of oxide SSEs,⁴⁴ cells suffer from mechanical contact loss between electrode materials and the SSE upon cycling, which significantly impacts battery performance.⁴⁵ However, the oxides have excellent stability characteristics in terms of air and moisture resistance⁴⁶ – a clear advantage over the unstable sulfide electrolytes.⁴⁷ Polymer electrolytes, although prone to dendrites due to their soft nature, have recently gained attention as they circumvent the rather complicated manufacturing and handling that sulfide and oxide electrolytes present.^{48,49}

The SSE/Li(s) interface is still one of the major obstacles for ASSBs for all three material classes. Consequently, this problem has gained significant attention over the last two decades. On the one

hand, the interface instability can lead to the formation of an interphase or mixed layer, which grows upon electrochemical cycling. This layer can have various electronic and ionic conductivity, a phenomenon that has been thoroughly investigated in the dissertation of R. Koerver⁵⁰ and associated publications.^{51,52} On the other hand, the high interface resistance can already be present upon cell assembly.⁵³ Typically, this resistance is associated with the formation of a thin layer depleted of Li^+ close to the electrode.⁵⁴ In ASSB applications, the depletion of mobile charge carriers has been found to significantly impact the performance of the cells.⁵⁵ This depletion layer is a part of the space charge layer (SCL) concept in SSEs, a fundamental phenomenon occurring at the interface between two materials with different electrochemical potentials, e.g., an electrode and an electrolyte.⁵⁶ While the SCL effect has received quite some attention in the early days of SOFC research in ceria-based electrolytes,^{57,58,59} the formation of such layers in solid Li^+ conductors still lacks fundamental understanding. With a more elaborate description of the theoretical understanding of SCLs in SSEs following in chapter 2, the following considerations are important to understand the formation of SCLs: (i) two materials of different chemical or electrochemical potential are in contact, (ii) the occurring potential difference is accounted for by a rearrangement of charges, (iii) the only mobile species are cations, and (iv) the SSE crystal lattice poses constraints on the maximal concentration of accumulated and depleted cations. Suppose the electrochemical potential of the electrode is lower than that of the electrolyte. In that case, a Li^+ accumulation layer will form in the SSE, while a depletion layer will form at an interface towards an electrode of higher electrochemical potential. The excessive charge in SCLs can therefore be negative and positive, depending on the concentration of the only mobile species – the Li^+ .⁶⁰

The space charge phenomenon is strongly dependent on the (electro-)chemical potential difference between the two materials, which makes direct experimental evidence hard to come by. *Ex-situ* experiments are mostly unable to distinguish SCLs from other changes in the stoichiometry or chemical composition of the material, which is well known to occur at the interfaces of ASSB.^{61,62} *In situ* experiments often require a special cell design and the possibility to contact the electrode to control the formation of an SCL, which is naturally hidden beneath the electrode material.

One of the first investigations into the phenomenon of space charge in SSEs was led by Kornyshev and Vorotyntsev around 1980,⁶³ who developed a phenomenological theory for the polarization of SSEs with a single mobile charge carrier.⁶⁴ Almost two decades later, J. Maier summarized the

efforts to describe the solid ion conductor, i.e. an SSE, and a metal.⁶⁵ The conductivity in boundary layers was investigated regarding the defect chemistry, which forms the basis for any ion conductivity in solids. However, the concept of SCL formation in SSEs has recently gained more attention correlating to the spiking interest in the ASSB technology. In 2010, C. R. Mariappan et al. found high interfacial capacitance values in glassy electrolytes, which were significantly larger than in liquid electrolytes.⁶⁶ Ion adsorption on the surface of the electrode was suggested as the origin of a pseudocapacitive effect. With the accumulation of charges accompanied by a drop in electric potential, Yamamoto et al. were able to investigate the SCL formation in a working ASSB cell using electron holography on a miniaturized cell setup.⁶⁷ While drawing clear conclusions about the presence of such a charged layer, the authors avoided using the term “space charge layer”. In another publication, the accumulation of Li⁺ around the SSE/electrode interface during initial charge and discharge was found to manifest within the electrolyte.⁶⁸ Between an oxide cathode and a sulfide electrolyte, Tateyama and co-workers found using Density Functional Theory (DFT) that an SCL grows during the charging, leading to an increased interface resistance.⁶⁹

With the suspected elusive nature of SCL formation and its electrochemical properties, only a limited number of experimental investigations exists, which vary drastically in their conclusion about the size of the SCLs. For ASSB applications, the most important question is whether the formation of an SCL leads to an increase in interface resistance.

Very low resistance of 8.6 Ωcm^2 at the cathode/SSE interface was reported by Haruta et al.⁷⁰ in an electrochemical study of sputtered LiPON (Lithium Phosphorus Oxynitride) films. Although the low interface resistance contrasts with older literature on thin-film ASSBs, that report significantly higher resistances.^{71,72} With electrochemical measurements pointing to a low interface resistance, no measurements, in which the SCL is actively formed or its existence has proven, were performed. Another work by Cheng et al. on a cathode/SSE interface used NMR (Nuclear Magnetic Resonance) exchange measurements in combination with an electrochemical setup to tune the SCL formation.⁷³ By varying the Li⁺ content in the cathode material, the authors were able to control the electrochemical potential between 2 and 4 V vs. Li/Li⁺. They report significantly higher activation energy, and thus energy barrier, for the Li⁺ exchange over the interface between a Li_xVO₂O₅ and a Li_{1.5}Al_{0.5}Ge_{1.5}(PO₃)₄ (LAGP) SSE of 0.515 eV compared to 0.315 eV when no SCL

is present. While not involving *in situ* electrochemical measurements, the tuning of the cathode potential allows a selective study for the influence of the electrochemical potential difference across the interface and its consequences for the cation diffusion coefficient, which is reported 17 times lower than the bulk diffusion coefficient. The authors, therefore, conclude that the SCL has a detrimental impact on cell performance.

While a real cathode or anode material is naturally more relevant for ASSB applications, the fundamental physical and electrochemical properties of SCLs can be investigated on a simpler model system. For a metal/SSE interface, the SCL is tunable by applying a bias potential that allows *in situ* experiments. This approach was used by Nomura et al. to visualize the Li^+ and potential profiles around the interface of an oxide SSE and a copper electrode.⁷⁴ The application of a bias potential of up to 1.95 V leads to a thick (up to 420 nm) negative SCL formation. Using phase-shifting electron holography,⁷⁵ the SCL was approximated to be roughly 10 nm thick at the Cu/SSE interface without any additionally applied potential. Fuller et al. recently investigated a full ASSB cell with spatially resolved Kelvin probe force microscopy to measure the contact potential difference across a miniaturized ASSB cell consisting of a Si anode, a LiPON electrolyte, and a LiCoO_2 cathode.⁷⁶ Additionally, they employed neutron depth profiling to measure the Li^+ concentrations *in situ*. The authors concluded that the largest potential drop occurs at the anode/SSE interface, which is accompanied by a performance-limiting interfacial process for the charge transfer of Li^+ . The SCLs are approximated to extend several hundred nanometers into the bulk SSE. In summary, the experimental findings qualitatively conclude that the cathode/SSE interface exhibits a smaller, less pronounced SCL compared to the anode/SSE interface, but the quantitative analysis of its thickness is inconclusive.

The formation of SCLs can also be viewed from a theoretical perspective with two major viewpoints: a continuum model for thermodynamics and an electrochemical model with analytical equations. A thermodynamic model by Braun et al.,⁷⁷ introduced in detail in section 2.4, comprises a semi-analytical equation for the charge carrier concentration in the SSE and two boundary conditions for the charge concentration at the interfaces towards the electrodes. Derived from the free energy functional of mixing enthalpy, polarization energy, and linear elastic energy, the chemical potentials are stated separately for cations, vacancies, and anions. Notably, the Coulomb interaction is neglected, and only the stationary case with vanishing time derivatives is regarded.

The physical boundary conditions include blocking electrodes with no charge transfer, making the applied bias potential the most important physical parameter. The applied bias potential and, therefore, the voltage drop across the two interfaces is the driving force for the formation of SCLs. The study concludes that the SCL formation is highly dependent on the available vacancy sites and the cation concentration with thick (up to 2 microns) asymmetric layers growing plane-parallel to the electrodes into the electrolyte. However, the neglect of the Coulomb interaction within the highly charged layers suspected leads to an underestimation of the thicknesses.

In a study by de Klerk et al., an electrochemical model based on the chemical potentials of the cations was developed.⁷⁸ While this model considers Coulomb interactions and uses a solid solution model⁷⁹ for the cation distribution in the SSE, the underlying SSE crystal structure constraints are neglected. Especially, no boundary conditions for cation and vacancy concentrations are set – leading to a prediction of very thin layers with negligible impact on the interfacial resistance, a result in strong contrast with the thermodynamic model.

With neither experimental investigations nor theoretical models leading to a conclusive picture of the SCL formation in SSEs, the scope is now widened to the more elaborate and widely accepted models for the diffuse double layer formation in liquid electrolytes. In liquid electrolytes (LEs), the charges accumulation near the electrode interface is called an electrical double layer (DL) with investigations dating back to the 19th century with a first description by H. Helmholtz in 1853.⁸⁰ He proposed a simple model of two layers of opposite charge, one in the electrode, another one in the electrolyte, with the stored charge linearly dependent on the voltage dropping across the interface. The DL, treated as a layer of a molecular dielectric, exhibits a differential capacitance that is measurable through, e.g., electrochemical impedance spectroscopy (EIS). With observations in the early 1900s, L. Gouy and D. Chapman developed a model introducing a diffuse part of the DL structure, which decays exponentially away from the interface. O. Stern united the two theories into a two-layer model in 1924.⁸¹ While further elaborations of the description of the DL, especially for ionic liquids, exist,^{82,83} the simple model of a compact Helmholtz layer and a diffuse Stern layer suffices for the comparison to the SCL structure in SSEs. **Table 1** compares some systems in which charges accumulate at the interface between two materials. The close similarity of SSEs to semiconductors, which will be explained in detail in section 2.3, will later be

used to develop an approach analogous to the common Mott-Schottky analysis of semiconductor junctions, see section 2.5.

Table 1. Comparison of physical and electrochemical properties underlying the interfacial charge layers in different systems.

	semiconductor	liquid electrolyte	solid-state electrolyte
mobile species	electrons or holes	multiple (cations, anions, etc.)	cations
charge concentration	high	low	high
limit in concentration	low (lattice)	high (volume)	low (lattice)

The current understanding of the SCL formation in SSEs, as described above, does not involve a diffuse and a compact part as the description of the DL in LEs. Compared to LEs, two main differences can be pointed out: (i) the SSE lattice's vacancy concentration, i.e., the maximum in cation concentration, and (ii) higher overall charge concentration in SSEs. While the impact of aspect (i) can easily be conceived considering that the same number of cations can only be stored in a much wider layer, aspect (ii) might mitigate this effect for a charge depletion.

With some early research on the DL structure in LEs fundamentally based on EIS, a technique that will be used extensively in this work to investigate the SCL formation and properties in SSEs, the following introduces the concept of EIS and the impedance of SSEs. An in-depth description of the working principle and possible fallacies in the analysis and evaluation of the data will be presented in section 3. An EIS measurement is based on the application of a sinusoidal voltage perturbation to the electrochemical system at hand and measuring the current response. Assuming a linear and stationary system, the complex impedance can be calculated for a range of different frequencies – hence the term spectroscopy. With electrical equivalent circuits representing physical and electrochemical processes, the resulting impedance spectra can be analyzed, and information about the electrochemical system can be obtained.

The impedance of SSEs can be separated into two major contributions: the bulk of the electrolyte and the interfaces towards the electrodes. The bulk electrolyte contains grains of variable sizes,

which are small crystalline structures. The ionic conductivity is typically best within the grains⁸⁴, with the boundaries between grains forming an energetic barrier for the ions. While some single-crystal SSEs have been reported in the literature,⁸⁵ polycrystalline materials make up most of the relevant literature. One of the first descriptions of the grain-boundary impact on the electrochemical response of such a system was published in 1969 by J. Bauerle.⁸⁶

While the conductivity, and therefore impedance, in a structure consisting of crystallites can be simplified to a single bulk resistance, EIS is a common tool to study the impact of grain-boundary resistances on the overall electrolyte resistance.^{87,88} The impedance of microstructures, e.g., grains and their respective boundaries, has been previously investigated by J. Fleig and J. Maier for less specific materials and systems.^{89,90,91,92} With the description of the impedance of the bulk by a single resistance and the possible elaboration with grain boundaries, the more complicated interface structure and impedance can now be introduced. Importantly, the difference between non-blocking and blocking conditions must be considered. Suppose no charge transfer can happen at the interface between SSE and electrode, either due to the material of the electrode or the electrochemical difference. In that case, the electrode is called ion-blocking or simply blocking. This is the case for electrodes of Gold⁹³ and some other metals. The interfacial impedance of an SSE in blocking configuration was modeled by J. Wang and J. Bates, considering the effect of surface roughness.⁹⁴ A comparison between the interface impedance of single-crystal and polycrystalline SSEs can be found in a work by R. Armstrong and R. Burnham.⁹⁵ More recently, Levasseur and co-workers found that the impedance response of a glassy SSE in different electrode conditions (non-blocking and blocking) can be well described using charge transfer resistances.⁹⁶ In the case of non-blocking electrodes, the energetic barrier for the exchange of Li⁺ between SSE and electrode is described by the charge transfer resistance – extensively investigated and described for the polarized interfaces in other systems, such as polymers,⁹⁷ cathode materials,⁹⁸ and the Silicon/LE interface.⁹⁹ As the SSE/electrode interface is regarded as the major bottleneck¹⁰⁰ to the ASSB performance, the interface has gained much attention in recent years. Most studies focus on phenomenological observation of the interface impedance of cathodes^{101,102,103} and anodes^{104,105,106} and the respective SSEs. Interface modification in terms of artificial protection layers and interphase formation has been shown to decrease the interface resistance significantly.^{107,108} However, the electrochemical origin of the observed interface impedances and

the causality of the mitigative effects of interlayers between SSEs and electrode materials lack a conclusive and elaborate theory.

This work explores the nature of SCL formation in a model SSE, and the physical implications of highly Li⁺-depleted layers are investigated. An Ohara LICGCTM (Lithium Ion Conducting Glass-Ceramic) electrolyte is extensively investigated towards impedance response and optical properties. In a first step, the spatial extent of the SCL in SSEs will be optically determined using spectroscopic ellipsometry, a method known for high depth resolution in the investigation of thin films. An advanced optical model for the SSE is proposed, and the accumulation and depletion of Li⁺ are modeled using an effective medium approximation (EMA). The EMA is not only used to determine the thickness of the layers and analyze a possible asymmetry between accumulation and depletion layer, but also to study the corresponding concentration change of the Li⁺.

Investigations using EIS at different applied bias potentials (and thus different SCLs), are used similarly to the analysis of DLs in LEs to determine the capacitance of SCLs and the dependence on the applied bias potential. A physical model is developed to facilitate the analysis of the impedance spectra and carefully validated using different external conditions, such as different electrode metals, bias potentials, and temperatures. The impact of the SCL formation on the interface resistance will be investigated, and a temperature variation is used to calculate the activation energy from the Arrhenius equation. Furthermore, a model like the Mott-Schottky equation for semiconductors will be proposed, and the charge carrier concentration in SSEs calculated. At last, a kinetic Monte Carlo model is used to close the loop from the physical understanding through experimental results to theoretical predictions.

2 Theory of Solid-State Electrolytes and Space Charge Regions.

As described above, most research in solid-state electrolytes (SSEs) focuses on chemical and electrochemical phenomena, and even research on the interface remains of chemical nature in most cases. Space charge layers are – in principle – a simple phenomenon, but still the origin of inconclusive results in the literature. The following chapter provides an overview of the environment in which the SCL occurs (the SSE crystal lattice), the driving force (the electrochemical potentials), an introduction to the thermodynamic model and a common model for semiconductor junctions, which will be adapted to SSEs in the course of this work.

2.1 Solid-State Electrolytes and Ionic Concentrations.

SSEs and the conductivity phenomena dominating the ion transport are best understood from a crystal lattice point of view. While the assumption of an isotropic, uniform lattice, i.e., perfect crystal, is a rough approximation for any solid ionic conductor, we will see during this thesis that these assumptions are sufficient to derive models describing the SSE in different electrochemical states.

For most of the relevant SSEs for ASSBs introduced in the last section, the conductivity origins in defects in an otherwise highly ordered crystal lattice allowing ions to hop between point,¹⁰⁹ linear¹¹⁰ or planar¹¹¹ defects. Common classification of point defects, which are present in the majority of Li^+ conducting materials, can be made by the source of charge. An anion vacancy, i.e., a missing anion in the otherwise periodic crystal lattice, is called a Schottky defect, whereas an interstitial, i.e., a cation where, e.g., no regular lattice site is present, is called a Frenkel defect. Independent of the defect type, the conductivity process is dominated by the cations with transference numbers close to 1.¹¹² The fact that the anions are considered immobile^{113,114,115} will become important for the considerations of charge accumulation. The energy landscape in SSEs can therefore be described as a periodic well of the defect and anion potentials with cations moving across the defect lattice with a thermally activated process. The whole electrolyte is assumed to stay electroneutral^{116,117} if no additional sources of cations or excessive potentials outside of the

electrochemical potential window are applied. At an atomistic level, this view is almost complete and – together with a thermodynamic framework – would allow simulations of the ionic conduction process. However, reports on single-crystal SSEs remain rare in the literature^{118,119} and inhomogeneities must be considered. These could be either grain boundaries in between two crystallites¹²⁰ of the same material or even different phases within the same material.¹²¹ The grain-boundary effect has been long discussed to have a detrimental impact on overall ionic conductivity,¹²² where conductivity can happen across or along these boundaries. However, for the considerations in this work, the grain boundaries and their electrochemical properties are considered not important as they are not dominating in the impedance response in our material system, which will be explained in detail later.

A thorough definition of charge carrier concentrations is important to be able to discuss the SCL formation as a displacement of the existing cations in a fixed lattice of anions, vacancies, and cations. In the following, c_α and z_α denote the concentration and charge of species α , respectively. The anions, denoted by the subscript a , in the SSE form a constant background concentration of negative charge, $z_a c_a = \text{const}$, and immobility is a classical assumption in theoretical considerations^{123,124} that has been experimentally validated.^{125,126}

The Li^+ is now considered the only cation in the SSE lattice. We define the cation concentration as a sum of the mobile and immobile cations $c_{\text{Li}} = c_{\text{Li},\text{mobile}} + c_{\text{Li},\text{immobile}}$, which for the bulk SSE without any electrochemical driving force must match the stoichiometric cation concentration of the material. Under blocking conditions, the total Li^+ content inside of the SSE is fixed, and therefore the volume integral must be constant, $\int_{\text{SSE}} c_{\text{Li}} = \text{const}$. However, as a thermally activated process, the concentration of mobile Li^+ $c_{\text{Li},\text{mobile}}$ might depend on temperature, which will be investigated in this work, see section 6.3. While stoichiometric concentrations are known for most SSE materials, the actual fraction of mobile Li^+ remains an open question.¹²⁷

The vacancy concentration requires a careful introduction, as it is important for the upper limit of Li^+ concentration. At a given equilibrium state of the system, the total number of vacancies is constant and consists of the occupied vacancies and free vacancies, $c_v = c_{v,\text{occ}} + c_{v,\text{free}}$. However, the total number of vacancies c_v accessible to Li^+ is subject to vary with temperature and other thermodynamic variables. The vacancies are assumed to be massless and chargeless and

therefore do not contribute to the overall charge. In electrochemical equilibrium with no applied bias potential or other driving force, the electrolyte is electroneutral. Therefore, the total cation concentration must match the anion concentration $c_{Li} = c_a$.

The natural boundaries for the cation concentration are therefore given by the maximal concentration where all accessible vacancies are filled $c_{Li} = c_v$ and the minimal concentration where all mobile Li^+ are depleted, $c_{Li} = c_{Li,immobile}$. Here, it is important to differentiate the cation concentration from the net charge. The net charge in a lattice fully depleted of mobile cations will match that of the excess anions, no longer compensated by the missing cations. In other terms, the net charge is $z = -z_{Li}c_{Li,mobile}$ under the assumption of the equal absolute value of the charge of anion and cation. In the opposite case, a lattice fully accumulated with cations, the net charge will equal that of the total number of vacancies $z = z_{Li}c_v$. For the sake of simplicity, the bulk concentration of mobile Li^+ will be denoted as $c_{Li,bulk}$. A simplified view of such lattice with the different lattices sites is shown in **Figure 2**.

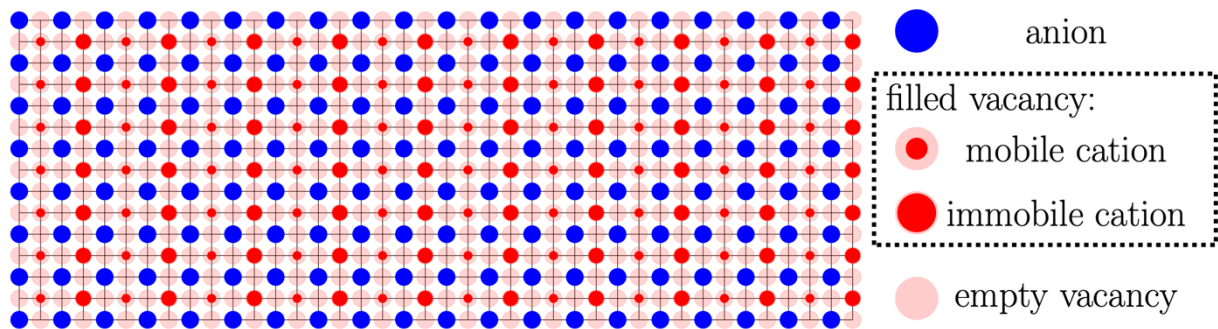


Figure 2. Idealized crystal lattice with mobile and immobile cations, filled and free vacancies, and a fixed anion background. In this example, the number of mobile and immobile cations is equal, and the number of vacancies is double the number of cations. Any cation accumulation or depletion is therefore limited by the immobile cation concentration and the vacancy concentration.

The inherent difference of negative and positive charge in the maximal absolute charge storable within a volume will become important later when a certain amount of charge within the SSE is displaced. The displacement of charge in SSEs at the interface towards the material of different electrochemical potential is nothing less than the SCL formation, which will be explained in detail

in section 2.3. First, we need to define and discuss the driving force for any movement of Li^+ , which is a difference in electrochemical potentials between the electrolyte and electrodes.

2.2 Fundamental Electrochemical Considerations.

As an electrochemical system, the state of the SSE will change as soon as it is brought into contact with any other material or subjected to an electric field. Understanding the SSE's behavior with changing external conditions requires a background in general electrochemistry.

The chemical potential μ_i is a measure of how much energy is required to add or remove a certain species to a certain point in space.¹²⁸ The straightforward definition is by deriving the free energy G_i with respect to the particle number n_i .

$$\mu_i = \frac{\partial G_i}{\partial n_i} \quad \text{Equation 1}$$

In the system defined above, the addition of an ion can be interpreted as the replacement of a free vacancy with an occupied vacancy. The removal is replacing an occupied vacancy with a free vacancy, thus removing the cation.

In an electrical field, e.g., caused by an externally applied electrical potential, the chemical potential becomes an electrochemical potential for a particle of charge z_i in an electrostatic potential ϕ :

$$\tilde{\mu}_i = \mu_i + z_i F \phi \quad \text{Equation 2}$$

where F is the Faraday constant.

From a thermodynamic standpoint, for the bulk electrolyte, a (meta-) stable energy state of the system is achieved by minimizing the sum of electrochemical potentials of the different charge species in the system.

$$0 = \sum_i d\tilde{\mu}_i = \sum_i d\mu_i + F d\phi \sum_i z_i \quad \text{Equation 3}$$

The driving force for a particle of species i is given by the spatial derivative of the electrochemical potential:

$$\nabla\tilde{\mu}_i = \nabla\mu_i + z_i F \nabla\phi \quad \text{Equation 4}$$

This derivative is a local property of the electrochemical system, and the fact that a minimum in electrochemical potential can be achieved by balancing the electrical with the chemical potential or vice versa will become essential when a certain region of the SSE effectively shields an external potential by a non-zero charge distribution.

In thermodynamic equilibrium ($\nabla\tilde{\mu}_i = 0$), the Nernst-Einstein equation¹²⁹ for particle species i can be derived, which links the diffusion coefficient D_i and the mobility u_i :

$$\frac{D_i}{k_B T} = \frac{u_i}{z_i e} \quad \text{Equation 5}$$

where e is the electron charge, k_B the Boltzmann constant, and T the temperature.

In the presence of an electrical field, the movement of ions is typically described using a Poisson-Nernst-Planck (PNP) model. Typically, these models are of limited use for SSEs due to the high ion concentrations.^{130,131}

Therefore, a modified PNP equation has been recently developed to describe the ion dynamics in SSEs.^{132,133}

$$J_i = -\frac{D_i}{1 - \tilde{c}_i} \nabla c_i - \frac{z_i F D_i}{RT} c_i \nabla \Phi \quad \text{Equation 6}$$

Here, c_i is the ion concentration, \tilde{c}_i the vacancy concentration (both for the ion i), R the universal gas constant, J_i the flux of ion i , and Φ the external field.

The ionic conductivity of ion species i can then be expressed with the electron charge e :

$$\sigma_i = z_i e c_i u_i \quad \text{Equation 7}$$

As the conductivity is directly dependent on the concentration and mobility, it is a thermally activated process in which the temperature dependency can be described using the Arrhenius equation:¹³⁴

$$\sigma_i = \frac{A}{T} \exp\left(-\frac{E_a}{k_B T}\right) \quad \text{Equation 8}$$

Here, E_a is the activation energy and A the pre-exponential factor. The activation energy for the conductivity process is the amount of energy required to promote an ion to take part in the conduction process, or in other words, to overcome the potential well of the anion lattice. All other contributions to the ionic conductivity are contained in the pre-exponential factor.

2.3 Space Charge in Semiconductors and Ionic Conductors.

A theoretical understanding of the SCL formation can be approached in two different ways: (i) from a semiconductor point of view, but with ions and vacancies taking the role of electrons and holes, and (ii) from a liquid electrolyte perspective, but with fixed anions, no solvent and different ion concentrations. In this thesis, we will discover that both approaches are useful to describe the nature of SCL formation.

In semiconductors, the space charge phenomena at the interface of two materials with different Fermi levels, e.g., a semiconductor junction, are well described and formulated as follows. Note that no complete description of the physics of semiconductors will be given, but only the most important ideas are presented. A detailed description of the physics of semiconductors can be found in most good textbooks on that topic, e.g., by Balkanski and Wallis.¹³⁵

When two semiconductors of different electron concentrations are brought into contact, the Fermi levels will align¹³⁶ by a current of electrons from the n-type to the p-type semiconductor and an increase of hole concentration on the opposite side. The region in which the concentration of electrons and holes effectively changes is then called the space charge region. As the Poisson equation dictates, the electric field and potential are also non-zero in this region.

$$\nabla^2 \phi = -\frac{\rho}{\epsilon}, \text{ with } E = -\nabla \phi \quad \text{Equation 9}$$

Here, ρ is the charge distribution, ϕ the electrical field, and ϵ the permittivity.

For the case of electroneutrality outside the space charge and a continuous electric field, the electrostatic potential can be calculated to:¹³⁷

$$\phi(x) = -\frac{q}{2\epsilon} N_D (x - l_n)^2 + \frac{q}{2\epsilon} (N_D l_n^2 + N_A l_p^2), \text{ for } -l_n \leq x \leq 0 \quad \text{Equation 10}$$

$$\phi(x) = -\frac{q}{2\epsilon} N_A (x - l_p)^2, \text{ for } 0 \leq x \leq l_p \quad \text{Equation 11}$$

Here, the SCL width is given by l_n and l_p inside the n-type and p-type semiconductors, respectively. The donor and acceptor densities are given by N_D and N_A , and q denotes the electron

charge. The vacancy density is denoted as N_V . As overall electroneutrality across the device must hold, $N_A l_p = N_D l_n$ can be assumed and used to calculate further properties.

The potential drops quadratically to either side of the junction in this approximation, which is an important result for the analysis of the electrical properties of these layers. With the definition of the bandgap E_g , one can calculate the built-in potential to:

$$V_{bi} = \frac{k_B T}{q} \ln(N_A N_D / (N_C N_V \exp\left(-\frac{E_g}{k_B T}\right))) \quad \text{Equation 12}$$

The built-in potential is a measure of how the charge carrier concentration of the two semiconductors leads to an electrical field across the interface even without applying a bias potential. For the considerations of SCL formation in SSEs, an estimate of the thickness will become important. For a pn-junction in semiconductors, the SCL width can be written as:¹³⁸

$$W = \left(\frac{2\epsilon}{q} V_{bi} \left(\frac{1}{N_A} + \frac{1}{N_D} \right) \right)^{\frac{1}{2}} \quad \text{Equation 13}$$

Besides having different charge carriers, these layers in semiconductors can now be considered analogous to the situation in which an electrode and an electrolyte are brought into contact. While – of course – the Fermi level of the electrons will play a role in the electrode, the electrolyte is usually assumed to have negligible electronic conductivity. Therefore the effect of electron charge will only be a background potential (combined with the anion background).

Furthermore, based on the theory developed for semiconductors, a theory linking the applied bias across an electrolyte/semiconductor interface to the space charge capacitance has been developed: The Mott-Schottky theory.¹³⁹ As this thesis also aims at developing a similar theoretical approach for the metal/SSE interface, an elaborate discussion can be found in section 2.5.

The other point of view relies on theory to describe the double layer structure in liquid electrolytes, resembling the same electrochemical system only with the restrictions of a crystal lattice for the electrolyte. As described above, the modern theory on DLs in LEs describes two different layers. A compact and dense Helmholtz layer next to the electrode is combined with a diffuse Stern layer, ranging further into the electrolyte with an exponential potential drop.

For the Helmholtz layer, the potential perpendicular to the (perfectly planar) electrode is assumed to decrease linearly due to the step-like charge distribution. The electrolyte and metal potentials are given by ϕ_L and ϕ_M , whereas the double layer width is d .

$$\phi(x) = (\phi_L - \phi_M) \frac{x}{d} + \phi_M \text{ for } 0 < x < d \quad \text{Equation 14}$$

The capacitance is easily calculated using the contact area A , the thickness d , and the dielectric constant ϵ_R :

$$C_{DL} = \frac{\epsilon_0 \epsilon_R A}{d} \quad \text{Equation 15}$$

Here, ϵ_0 is the dielectric constant of vacuum.

The more diffuse and wider part of the double layer structure is usually described by the Debye length, which originates in the Debye-Hückel theory.^{140,141} In this theory, a characteristic length scale is derived, which provides a measure for the distance in which the electrostatic force drops to 1/e of the initial value around a charged particle or interface.¹⁴²

The Debye length can generally be expressed using the ion concentration c , the charge q , Temperature T , dielectric constant of vacuum and bulk ϵ_0 and ϵ_R , and the Boltzmann constant k_B :

$$\lambda_D^2 = \frac{\epsilon_0 \epsilon_R k_B T}{q^2 c} \quad \text{Equation 16}$$

Although this theory is only valid for low electrolyte concentrations, as the direct Coulomb interaction between ions is neglected in the Poisson-Boltzmann theory used to derive the Debye length and typically underestimates the length scale, the theory is useful for a first approximation.¹⁴³

Considering the SSE with a crystal lattice as described in section 2.1 and the electrochemical potentials as described in section 2.2, the theory to describe an SCL in SSE can now be approached.

The driving force for a charge accumulation at the interface between the SSE and an electrode is the electrochemical potential difference and we define it as follows:

$$\Delta\tilde{\mu} = \tilde{\mu}_{SSE,bulk} - \tilde{\mu}_{electrode} \quad \text{Equation 17}$$

Note that the potential of the SSE is defined at some point in the bulk of the electrolyte, which is not affected by an accumulation or depletion of charges and therefore is electrically neutral. The electrode potential assumes that the electrode is ideally polarizable, implicating that no charge transfer reactions can take place. This assumption is equal to the blocking conditions in which the SSE is investigated in this work, as described in section 5.3.

As in the case of semiconductors described above, this potential difference leads to an accumulation of charge, either by an accumulation or a depletion of Li^+ , which are the only mobile ion species in the SSE. For the sake of simplicity, a single SSE/electrode interface is described first, and the second interface will be introduced later.

No conclusive and generally accepted theory for the description of SCLs at the SSE's interface towards other materials exists so far. As described in the literature review in chapter 1, a variety of models has been proposed, which are valid for the specific material system and approach.

For the case of an interface at which the electrode is more electrochemically negative, i.e., $\Delta\tilde{\mu} > 0$, an accumulation of Li^+ , equivalent to a depletion of free vacancies, will occur. The net charge in this layer is positive, and we call this layer an accumulation layer or positive space charge layer (p-SCL). As the accumulation of Li^+ is limited by the number of accessible vacancies, once the maximum concentration is reached, the layer must grow perpendicular to the electrode into the electrolyte to hold an additional charge. For large enough potentials, the concentration profile is assumed to take a step-like form with a height equal to the maximal concentration and a sufficient thickness to account for the charge accumulation. The step-like form is a common approximation in semiconductors, also known as the *abrupt approximation*.¹⁴⁴ Assuming a nearly rectangular shape of the SCL, the charge Q_{p-SCL} held inside can be formulated with the vacancy concentration $c_{v,bulk}$, the thickness d_{p-SCL} , and electrode area A .

$$Q_{p-SCL} = Ac_{v,bulk}d_{p-SCL} \quad \text{Equation 18}$$

As the bulk of the electrolyte is shielded from the electrochemical potential of the electrode, the potential must drop across the p-SCL. For the sake of simplicity and better visualization, the

electrochemical potential difference is now replaced by an electrical potential which is applied by blocking electrode and referred to as the bias potential ϕ_{bias} .

As soon as a bias potential comes into play, the second SCL becomes non-negligible as the bias potential is applied through a second electrode – with opposite polarity and thereby creating a layer of opposite charge. At the interface where the electrode is more (electrochemically) positive, the SSE will now see a depletion of mobile Li^+ as the electric field will drive the charges away from the interface. Again, assuming a rectangular shape and a perpendicular growth into the electrolyte, the charge Q_{n-SCL} and thickness d_{n-SCL} of this effectively negative charge SCL is given by:

$$Q_{n-SCL} = Ac_{Li,bulk}d_{n-SCL} \quad \text{Equation 19}$$

This equation represents the fact that the number of depletable Li^+ is limited by the concentration of mobile Li^+ in the electrolyte. In blocking conditions, where no ion transport across the interfaces happens and the SCL formation is a mere redistribution of Li^+ , the charge of the layers must be opposite if the vacancies carry the opposite charge of the cations:

$$Q_{n-SCL} = Q_{p-SCL} \quad \text{Equation 20}$$

This yields a relation for a fraction of thicknesses and concentrations:

$$\frac{c_{Li,bulk}}{c_{v,bulk}} = \frac{d_{p-SCL}}{d_{n-SCL}} \quad \text{Equation 21}$$

As with the double layer in liquids, the SCL exhibits a capacitance, which we later show is measurable. The capacity for a layer of thickness d_{SCL} under the *abrupt approximation* is given by its geometric capacitance, based on the equation for a parallel plate capacitor:

$$C_{SCL} = \frac{\epsilon_o \epsilon_R A}{d_{SCL}} \quad \text{Equation 22}$$

Here, ϵ_R is the relative dielectric constant of the bulk and A the electrode area.

As the SCL is considered to have a major role in interface resistance, defining a space charge layer resistance and conductivity is important. The conductivity of Li^+ inside the SCL can be calculated based on the resistance R_{SCL} :

$$R_{SCL} = \frac{d_{SCL}}{\sigma_{SCL}A}$$

Equation 23

The SCL in the *abrupt approximation* can be treated as a “separate” SSE with a separate conductivity and possibly different activation energy due to the shift in electrochemical potentials. The activation energy can be calculated from the Arrhenius equation as introduced before. While several models have been described in the literature, one thermodynamic model was found to be very helpful in building an understanding of the SCL properties and their formation in SSEs.

2.4 Semi-Analytical Space Charge Layer Modeling.

The thermodynamic model by Braun et al.⁷⁷ is used for some of the numerical simulations in this work and will be briefly described here to understand its capabilities and limitations. The concentration profiles, the major result of this model, can be described by a semi-empirical equation, which is derived later in this section.

In addition to the SSE lattice, which defines the concentrations and their boundaries for the different species, the model relies on conservation equations for mass and momentum. As described, the anions are immobile and the vacancies are mass- and chargeless. In the stationary case, the particle conservation law can be written with the velocity of each particle v_α for $\alpha = c, a, v$, which denotes the cations, anions, and vacancies, respectively.

$$\text{div}(n_\alpha v_\alpha) = \text{div}\left(\frac{\rho}{\rho - \rho_\alpha} J_\alpha\right) = 0 \quad \text{Equation 24}$$

Here, J_α is the flux of species α , n_α the particle density, and using $\rho_\alpha = m_\alpha n_\alpha$, $\rho = \rho_c + \rho_a$ is the mass density.

The momentum conservation can be formulated with the Cauchy stress tensor found in an article by Dreyer et al.¹⁴⁵ and using the free charge carrier density $n^F = z_c n_c + z_a n_a$:

$$-n^F \Delta \phi = \text{div}(\rho v \otimes v) + \nabla p \quad \text{Equation 25}$$

, where p is the pressure, v the velocity vector and Δ the Laplace operator.

Note that the free charge density n^F is zero in the electrical neutral bulk and assuming $z_c = -z_a$ represents the same limits as defined above: A minimum of $n^F = -z_c n_a$ and a maximum of $n^F = z_c n_c$ can be reached, limiting the charge concentration in the SCLs.

The electric field E is correlated to the free charge density by the Poisson equation, now restated as:

$$\text{div}(\epsilon_0 \epsilon_R E) = -n^F \quad \text{Equation 26}$$

As this defines the most important physics governing the SCL formation and the derivation of the free energy functional and the entropy production equation are rather lengthy, the reader is referred to the original work by Braun et al.⁷⁷ for a complete derivation of the equations below. The authors introduce a characteristic length of the SCL, like the Debye length in liquids, defined as follows:

$$\lambda^2 = \frac{k_b T \epsilon_0 \epsilon_R}{e_0^2 n_R L_R^2} \quad \text{Equation 27}$$

In this equation, the reference length L_R and bulk density n_R are used, with e_0 being the electron charge. The reference length L_R is the sample length in the direction of the applied electrical field, which implies that the SCL length depends on the sample geometry.

With the use of some minor approximations, the authors derive a single equation for the charge density n^F in the SSE.

$$\lambda^2 (F(n^F) \partial_{xx}^2 n^F + (\partial_x (F(n^F))) (\partial_x n^F)^2) = -n^F \quad \text{Equation 28}$$

with the definitions: $F(n^F) = \sum_i \frac{\gamma_i}{n^F + \beta_i}$, $\gamma_1 = -\frac{1}{z_c}$, $\gamma_2 = -\gamma_1$, $\beta_1 = z_c n_a$, $\beta_2 = 1 - \beta_1$.

The function $n^F(x)$ is defined on the open interval $x \in (0,1)$ with the electrodes at the coordinates 0 and 1. The boundary conditions of global charge neutrality (in blocking conditions) and the potential difference $\phi_{bias} = \phi(x=1) - \phi(x=0)$ complete the algebraic system.

The partial differential equation and its boundary conditions were implemented in a COMSOL MultiphysicsTM runtime environment to calculate the charge and potential profiles in one dimension with an unevenly distributed mesh to account for the narrow SCLs at either side of the electrolyte.²³¹

As the computation of the PDE is quite time consuming and often runs into singularities around the boundary conditions, an empirical equation using Sigmoid functions was developed.

A logistic function is a sigmoidal function to describe a transition between two states, concentrations, or energies used in a large variety of fields.^{146,147} It is usually defined using a lower boundary A, an upper boundary K, a growth rate B, and Q the value for argument zero.

$$f(t) = A + \frac{K - A}{(1 + Q \exp(-Bt))^{\frac{1}{\nu}}}$$

Equation 29

The factor ν describes the asymmetry of the function, and a typical graph for this kind of function can be seen in **Figure 3**.

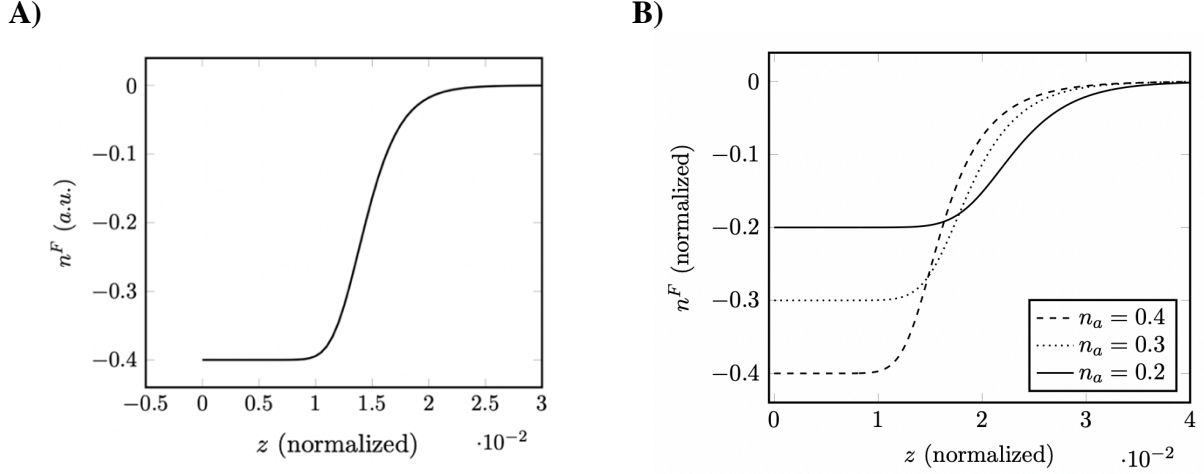


Figure 3. A) A general logistic function for a realistic set of parameters, which closely resembles the charge carrier concentration of a single SCL shown in **B)**. Standard parameters for the simulations are $\Delta\phi = 4V$, $\lambda^2 = 1.5 \cdot 10^{-3}$. The lower boundary for charge concentration is given by the parameter n_a , which resembles the anion concentration and is the maximum charge accumulable by depletion of ions.

As two SCLs must be accounted for, each is individually described by a general logistic function used to fit the original results from the thermodynamic model:

$$n_{empirical}^F(z) = -n_a + \frac{n_a}{(1 + Q_1 \exp(-B_1 x))^{\frac{1}{\nu_1}}} + \frac{1 - 2n_a}{(1 + Q_2 \exp(-B_2(x - 1)))^{\frac{1}{\nu_2}}}$$

Equation 30

This empirical equation contains 6 independent parameters: Q_i, B_i, ν_i for $i \in \{1, 2\}$.

The initial PDE system contains 3 independent variables: the applied bias potential ϕ_{bias} , the anion concentration n_a , and the characteristic length λ . Additionally, the boundary conditions for the potential drop across the SSE must be fulfilled. The boundary conditions for the concentration near

the electrodes are $n^F(x = 0)$ and $n^F(x = 1)$, in the case of a normalized concentration where $n^F \in (-n_a, 1 - 2n_a)$. The two boundary conditions can be formulated by introducing two deviation parameters δ_i .

$$n^F(z = 0) = -n_a + \delta_0, \text{ for } \delta_0 > 0 \quad \text{Equation 31}$$

$$n^F(z = 1) = 1 - 2n_a - \delta_1, \text{ for } \delta_1 > 0 \quad \text{Equation 32}$$

With these boundary conditions, the parameters Q_1 and Q_2 can be eliminated if $B_i \gg 1$ holds:

$$Q_1 = \left(\frac{n_a}{\delta_0}\right)^{v_1-1} - 1 \quad \text{Equation 33}$$

$$Q_2 = \left(\frac{1 - 2n_a}{1 - 2n_a - \delta_1}\right)^{v_2} - 1 \quad \text{Equation 34}$$

Next, the empirical equation, combined with the equations for Q_1 and Q_2 , is used to fit the modeling results for the semi-analytical PDE for a standard set of parameters λ , ϕ , and n_a .

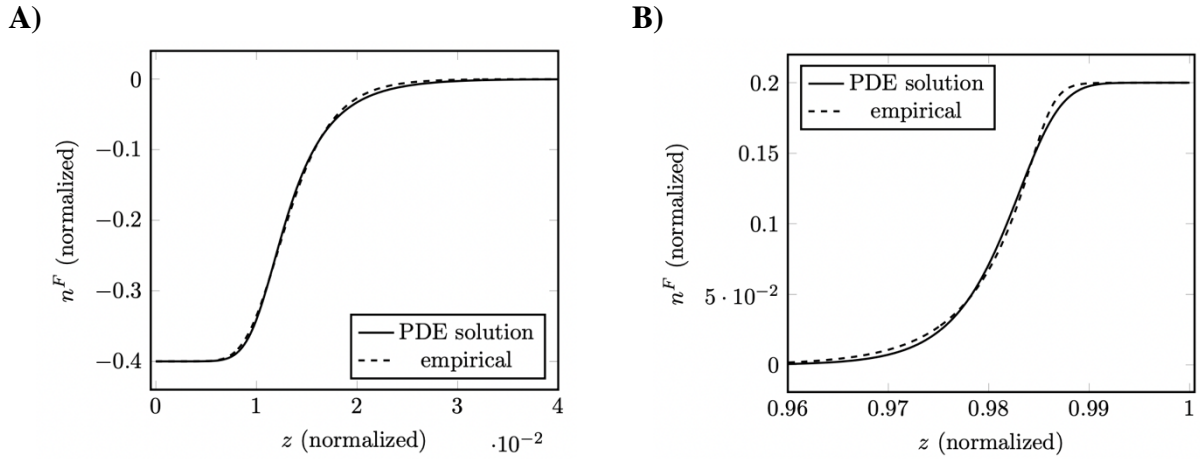


Figure 4. Charge carrier concentration profiles in the depletion layer **A)** and accumulation layer **B)** for $\lambda = 1.5 \cdot 10^{-3}$, $\Delta\phi = 4 V$, $n_a = 0.4$. The empirical fits using the sigmoid function are the dashed lines, which show very good agreement with the numerical solution to the PDE. In both the accumulation and depletion layers, the empirical fit overestimates the numerical solution to a small degree.

As shown in **Figure 4**, both the accumulation and depletion layers can be well described by the empirical equation. The regions of constant concentration are exactly reproduced with little to no deviation in concentration and spatial extent, whereas the transition is not precisely reproduced with a bit of overestimation, especially for the accumulation layer. However, numerical integration of the equation shows that the empirical equation adheres to the overall boundary condition of charge neutrality.

In the next step, the parameters of the empirical model can be fitted to the parameters of the original equation to be able to calculate a concentration profile based on the natural parameters λ . As this is the most critical parameter and the effect of $\Delta\phi$ is included in the boundary condition and therefore implicitly present in the calculation of the parameters Q_1 and Q_2 , it does not have to be calculated explicitly. A range of simulations for $\lambda \in [1.5 \cdot 10^{-6}, 1.5 \cdot 10^{-2}]$ which covers most sets of physical parameters is completed, shown in **Figure 5**, to be able to determine the impact of λ on B_1, B_2 and v_1, v_2 .

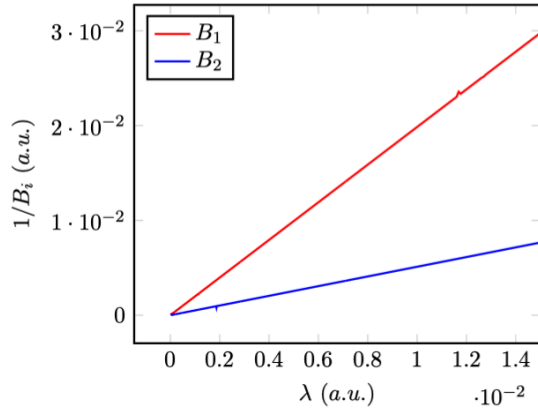
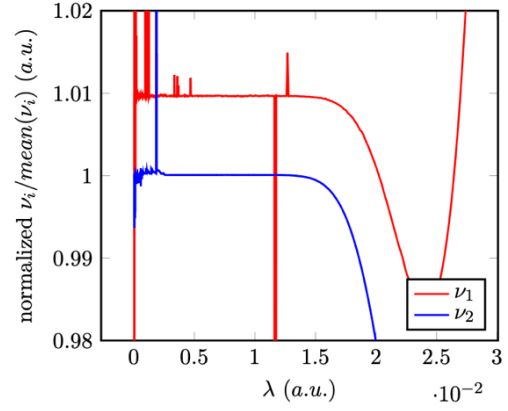
A)**B)**

Figure 5. Empirical parameters are determined by fitting the equation to numerical simulations. The parameters B_1, B_2 are inversely proportional to λ , whereas ν_1, ν_2 are constant for a wide range of $\lambda \in [1.5 \cdot 10^{-6}, 1.5 \cdot 10^{-2}]$. Note that the outliers present in **B)** are due to errors in the numerical calculations and are not filtered or removed here for the sake of completeness.

The empirical equation combined with the parameter dependencies sums up the analysis of the thermodynamic model and will be later used to visualize the impact of temperature on the SCL formation.

2.5 Mott-Schottky Theory.

The Mott-Schottky theory describes the thickness of the space charge region at semiconductor junctions. The theory has been long-standing and used for a variety of applications, such as the determination of carrier concentrations in oxide films¹⁴⁸ and the determination of flat band potentials.^{149,150} A short recap of the derivation is provided here to help the reader with understanding the derivation of the ionic Mott-Schottky theory presented in section 6.4.

The derivation is based on the book “The Physics of Semiconductors” by M. Grundmann found in reference 151. As explained in section 2.3, the SCL at the interface of a semiconductor is assumed to follow a step-like shape, which is called the *abrupt approximation*. Using the Poisson equation, one can write the charge carrier density n_D as:

$$-\frac{\partial^2 \phi}{\partial x^2} = \frac{\rho(x)}{\epsilon_R \epsilon_0} = \frac{en_D}{\epsilon_R \epsilon_0}, x \in [0, d_{SCR}] \quad \text{Equation 35}$$

Here, ϕ is the electrical potential, $\epsilon_R \epsilon_0$ the permittivity, $\rho(x)$ the charge distribution and d_{SCR} the thickness of the space charge region.

Using the next correlations and the electric field E , the applied bias potential ϕ_{bias} and electrode area A , the capacitance can be easily calculated:

$$\int_{\phi(0)}^{\phi(d_{SCR})} \frac{\partial^2 \phi}{\partial x^2} d\phi = \int E dE \quad \text{Equation 36}$$

$$C = A\epsilon_R \epsilon_0 \frac{\partial E}{\partial \phi_{bias}} \quad \text{Equation 37}$$

The Mott-Schottky equation, linking the capacitance and the applied potential ϕ_{bias} is obtained by deriving the expression for the electric field E to the potential ϕ_{bias} :

$$\frac{1}{C^2} = \frac{2(\phi_{bias} - U_{bi})}{A^2 \epsilon_R \epsilon_0 en_D} \quad \text{Equation 38}$$

Importantly, the integration constant U_{bi} determines the capacitance without any applied potential ϕ_{bias} , which is the built-in potential of the semiconductor junction. The MS equation combined with capacitance measurements at different applied potentials at the semiconductor/electrolyte interface is, therefore, a readily available tool to determine the mobile charge carrier density n_D .

3 Electrochemical Impedance Spectroscopy and the Importance of a Physical Model.

The application of electrochemical impedance spectroscopy (EIS) requires a thorough understanding of its working principles, its inherent limitations, and most importantly, the art of building a physical model to extract quantitative system parameters from the obtained impedance spectra.

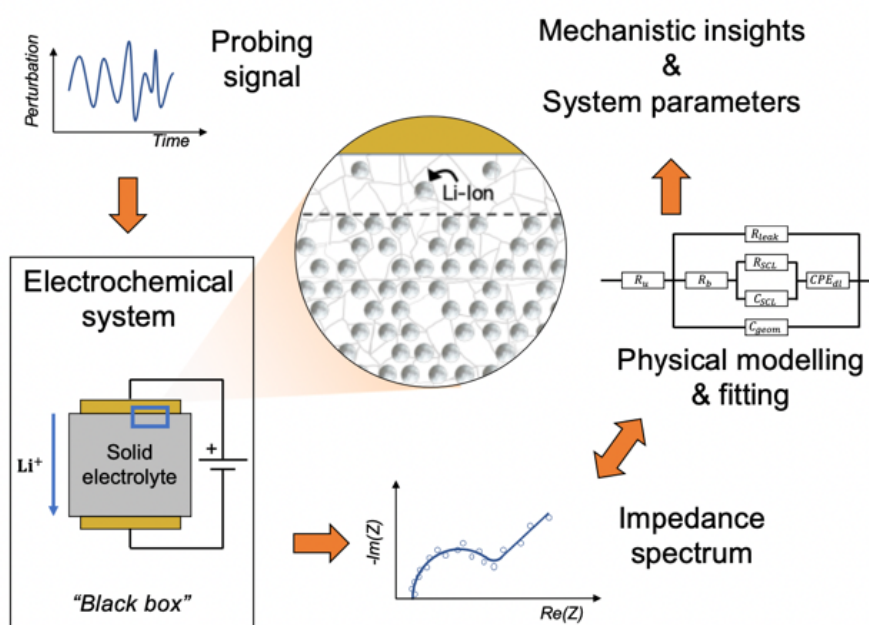


Figure 6. Overview of an EIS study. The impedance spectrum is recorded by probing the electrochemical system with a perturbation signal and measuring the response. The resulting impedance spectrum is then fitted using a physical model in the form of an electrical equivalent circuit to extract system parameters and gain mechanistic insights. *Graph adapted from Phys. Chem. Chem. Phys., 2021, 23, 12926, The Authors. Physical Chemistry Chemical Physics published by Royal Society of Chemistry.*

The process of recording, analyzing, and interpreting an impedance spectrum is shown in **Figure 6**, where a probing signal is used to test an electrochemical system and its processes. The recorded impedance spectrum is subsequently fitted with a physical model to gain mechanistic insights and

extract system parameters (such as the conductivity of the SSE). This section first explains the measurement principle of electrochemical impedance spectroscopy, secondly highlights criteria for data reliability, and finally explains the importance of the development of an equivalent circuit with a physical meaning.

While many well-written books on electrochemical impedance spectroscopy and its application in electrochemistry exist,^{152,153,154} the following section is based on “Electrochemical impedance spectroscopy and its applications” by A. Lasia, 2002.¹⁵⁵

3.1 Working Principle of Electrochemical Impedance Spectroscopy.

Recording an impedance spectrum is nothing more than measuring the system response upon applying an electrical excitation signal. If one applies a current and measures the resulting potential, the measurement is called galvanostatic. However, in this work, the measurements are done in the potentiostatic mode, where the current response of the system is measured while applying a potential, which consists of a constant term plus an overlaid disturbing signal. The technique of potentiostatic electrochemical impedance spectroscopy (PEIS) is commonly used in battery applications.¹⁵⁶

The gold standard in electrochemistry is the use of a reference electrode, which ideally requires a three-electrode configuration. However, most setups for investigating batteries are limited to two electrodes. Therefore, a short discussion of the two vs. three-electrode setup is given in the following. In a three-electrode setup, the working electrode potential is applied with regard to the counter electrode. The potential of the counter electrode must be constant, such that the applied potential to the working electrode is exact. This proves difficult, since the counter electrode is also the sink or source of current, and a common solution is to use a reference electrode. This reference electrode does neither take part in any electrochemical process nor pass any current and is solely used as a potential reference for the applied potential to the working electrode. With a two-electrode setup, which is used throughout this work, it is important to keep in mind the limitations. A high current flow through the counter electrode could lead to an unstable potential at the counter electrode and thereby distort measurements.^{157,158}

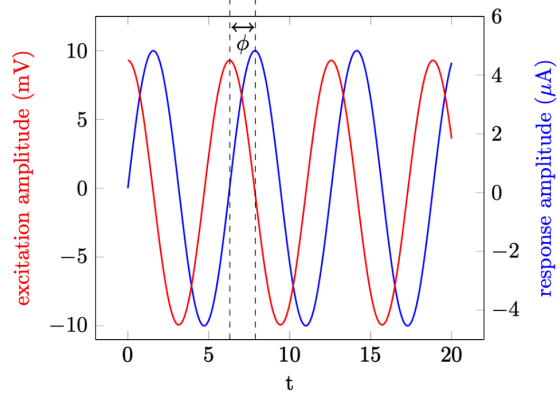


Figure 7. Working principle of a PEIS with a sinusoidal excitation voltage (red) and the system response in the form of a sinusoidal current (blue). If the assumptions of a linear and stationary response are fulfilled, the response frequency will match the excitation frequency with a phase shift ϕ between the curves. The excitation amplitude of 10 mV is a typical value, and the amplitude ratio gives the absolute value of the impedance.

In a PEIS, the potential is applied in the form of a sinusoidal signal with an amplitude E_0 and a frequency ω in a set frequency range ω_{min} to ω_{max} . As depicted in **Figure 7**, the excitation of the system can be written as $E(t) = E_0 \sin(\omega t)$. The current response of a linear and stationary system, which will be explained in detail in section 3.2, will then take the form of $I(t) = I_0 \sin(\omega t + \phi)$. The phase shift ϕ and the amplitude I_0 define the current response, from which the impedance $Z(\omega)$ for each frequency ω can be calculated to:

$$Z(\omega) = \frac{E(t)}{I(t)} = \frac{E_0 \sin(\omega t)}{I_0 \sin(\omega t + \phi)} = Re(Z(\omega)) + i Im(Z(\omega)) \quad \text{Equation 39}$$

The impedance, as a complex number, can be written in terms of a real and imaginary part ($Re(Z), Im(Z)$) or using the amplitude and phase ($|Z|, \phi$). In any representation, the full impedance spectrum consists of a complex number Z dependent on the frequency ω . Usually, the impedance spectrum is represented as Nyquist ($Re(Z)$ vs. $-Im(Z)$) or Bode ($|Z|$ vs. ω & ϕ vs. ω) plots, shown in **Figure 8A)** and **B)**. While Nyquist plots are sometimes helpful to reveal the number of underlying processes, it must be noted that the frequency does not appear in these plots.

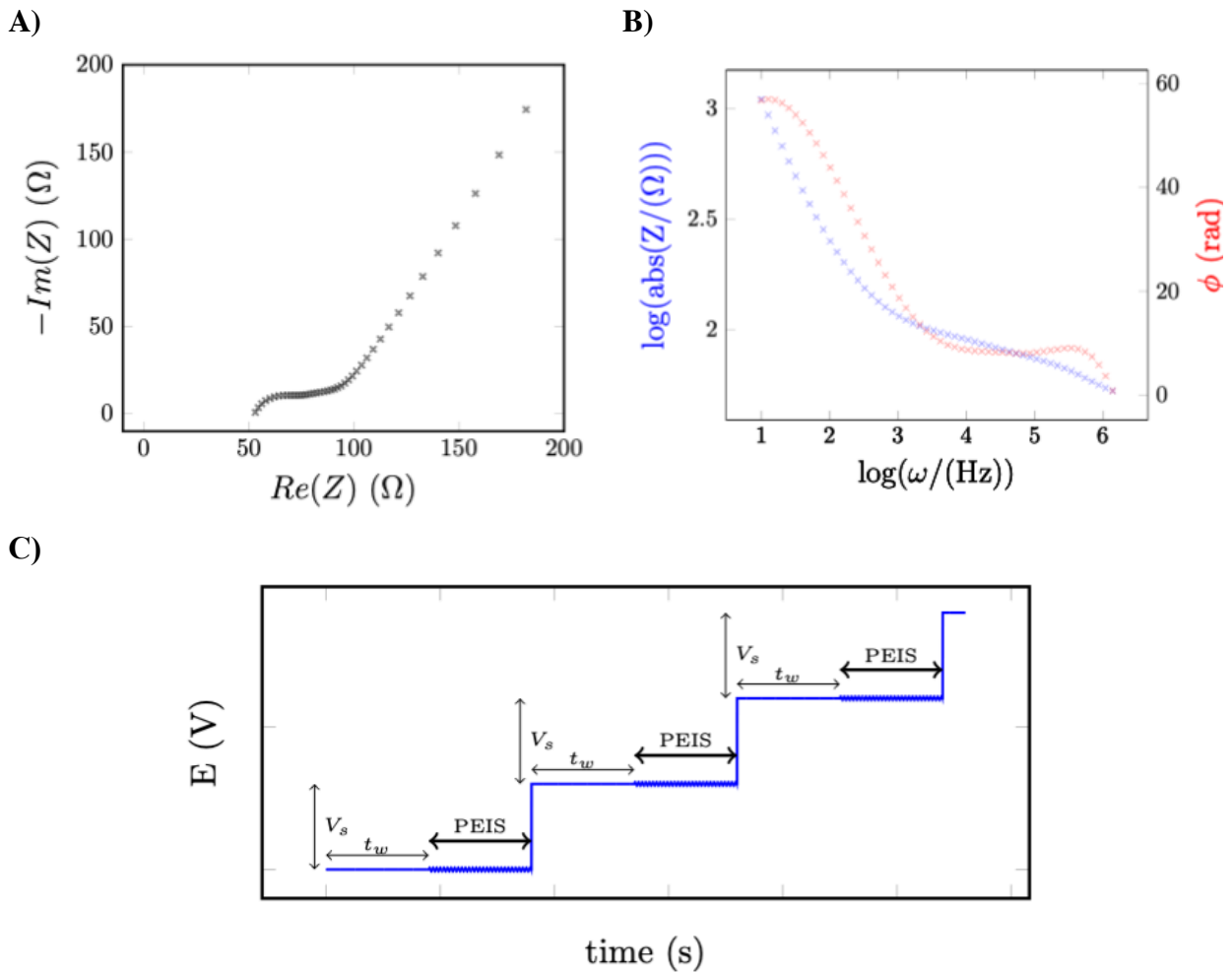


Figure 8. Typical representations of impedance data, the Nyquist plot in **A)** and Bode plot in **B)**. The Nyquist plot typically reveals the existence of features and electrochemical processes at a first glance, but hides frequency information. The Bode plot, consisting of two plots for the absolute value of the impedance and the phase shift, contains frequency information, but is usually harder to interpret. **C)** Applied voltage over time in a staircase potentiostatic EIS measurement with the waiting time t_w and voltage step size V_s .

An advanced technique of EIS, which will be used extensively in this work, the so-called staircase potentiostatic EIS (SPEIS), combines EIS with the application of a constant potential that changes in steps over time. Important parameters are the waiting time t_w , for which any potential step is held, and voltage step size V_s as shown in **Figure 8C)**.

Recording an impedance spectrum using modern equipment with a highly accurate potential and current acquisition capability at the given frequencies becomes an easy task. However, one must

keep in mind that the system response needs to fulfill two criteria: stationarity and linearity, which will be discussed in the next section.

3.2 Stationarity, Linearity and the Kramers-Kronig relations.

An electrochemical system is called stationary when the system does not change over time. In the case of PEIS, this is equivalent to the claim that the impedance $Z(\omega)$ is only a function of frequency and not of time. In mathematical terms, the second part of the current response shown in Equation 40 becomes zero.

$$I(t) = I_0 \sin(\omega t + \phi) + I_{non-stationary}(t) \quad \text{Equation 40}$$

The additional current will lead to distortions in the impedance for each frequency, which will unpredictably impact the impedance spectrum. For a linear or constant non-stationary current, which represents a drift of the electrochemical system, dedicated drift correction algorithms have been developed^{159,160,161} and implemented in software such as EC-Lab by Biologic®. A recent review by Szekeres et al.¹⁶² gives a good overview of methods for EIS in non-stationary systems.

However, the stationarity of an electrochemical system can be assured by a repeated recording of impedance spectra. A common solution is to apply a resting time before the recording takes place, which allows the system to settle in a steady state. While stationarity must be assured carefully, the linearity of the electrochemical system is typically fulfilled for small perturbation amplitudes. For battery applications in a PEIS, the perturbation potential is usually set between 5 mV and 20 mV.^{163,164}

When stationarity or linearity of the electrochemical system are not given or cannot be validated experimentally, a range of mathematical formalisms can help to detect distortions in the data. As EIS is a spectroscopic technique, harmonic analysis can detect non-linearity and noise within recorded impedance data.¹⁶⁵ Even simpler, and integrated into most EIS analysis software, the Kramers-Kronig (KK) relations can be used to validate impedance data. Mathematically speaking, the KK relations are a set of integral equations for the real and imaginary parts of a meromorphic function,¹⁶⁶ which all physical or electrochemical processes can be represented by.¹⁶⁷ For the

application in EIS, the KK check has been proven to be highly accurate in detecting a disturbance of the system in the forms of non-linearity, non-stationarity, and measurement noise.^{168,169}

While the recording of the impedance spectra is now formally completed and the spectrum can be checked for its validity, the most critical step to gain insights into the electrochemical system still lies ahead. A physical model must be built, describing the response of the processes taking place in the system. For EIS, these models are typically developed and represented as electrical equivalent circuits (EECs), and the importance of the physically motivated model building is highlighted in the next section.

3.3 Electrical Equivalent Circuits.

EECs are used throughout a wide range of applications to model a system's response to an external perturbation, for example, in plant cells,¹⁷⁰ piezoelectrics,¹⁷¹ photovoltaics,¹⁷² and battery applications.^{173,174,175}

All electrochemical processes in this work can be described using four basic elements:

- (i) a resistor R, for conductivity and charge transfer processes,
- (ii) a capacitor C, for charge accumulation at interfaces and geometric capacitances,
- (iii) an inductor L, mostly as artifacts of electrode wires¹⁷⁶ and cell design,¹⁷⁷
- (iv) a constant phase element CPE, for the description of imperfect capacitances.¹⁷⁸

Each of these elements is described by a complex impedance function of the frequency, which is represented in **Table 2**.

Table 2: Commonly used elements in EECs for the fitting of battery impedances, the resistor R, the capacitor C, the inductor L, and the constant phase element CPE.

Element	Resistor	Capacitor	Inductor	Constant Phase Element
Symbol	R	C	L	CPE
<i>Impedance</i>	R	$\frac{1}{i\omega C}$	$i\omega L$	$\frac{1}{Q(i\omega)^\alpha}$

The CPE requires a more delicate discussion, as the origins and physical explanation are not fully understood.¹⁷⁹ In addition to the pseudo-capacitance Q , the impedance of the CPE contains an additional parameter α . For $\alpha = 1$, the impedance matches that of a capacitor with $C = Q$, whereas, for $\alpha = 0$ the CPE impedance is a resistor with $R = \frac{1}{Q}$. Therefore, any value for α below 1 represents an imperfect capacitor that can originate from electrode surface structure,¹⁸⁰ porous electrodes,¹⁸¹ anomalous diffusion processes,¹⁸² and multiple reaction rates.¹⁸³ In this work, the CPE is used to account for the compact part of the electrochemical double layer, which is commonly done in liquid electrolytes.^{184,185} Typically, the Q value is treated as capacitance and used to

describe the double layer capacitance¹⁸⁶ if the value for α is above 0.9. Although more elements and parameters exist, such as the Warburg element for diffusion-limited processes,¹⁸⁷ these are applicable only in special cases and therefore omitted here. As every electrochemical system contains multiple processes, the elements above are arranged in the EEC using Kirchhoff's circuit laws by series and parallel connections. As the elements each describe an equation for the impedance response, the EEC is a mere graphical representation of the underlying equation.

The simplest EEC, which, for example, can be used to describe an electrochemical interface between an electrode and an electrolyte in a first approximation, is an RC-“element” comprising a resistor parallel to a capacitor. The low-frequency limit will be dominated by the resistor, and the impedance will be represented by a semicircle in the Nyquist plot. The fact that a semicircle is easily identifiable highlights the importance of a Nyquist plot for the first evaluation of impedance when an electrochemical system with multiple, possibly overlapping, processes is investigated.

An EEC must be able to fulfill three criteria at the same time: (i) a good fit is obtained, identifiable by a low deviation, (ii) being comprised by the minimal number of parameters to avoid overfitting, and (iii) representing the physical and electrochemical processes of the system.

Out of these three criteria, the third is the most complicated and requires delicate treatment. In a recent review article,¹⁸⁸ the importance of finding a physically meaningful EEC was elucidated with examples from battery research. The “black box” problem of EIS is a major concern when the elements contained in the EEC are assigned *a posteriori* to a physical or electrochemical process. Therefore, building an EEC must either follow strict physical reasoning, as shown in the derivation of an EEC for SSEs in section 6.2, or be accompanied with auxiliary techniques confirming that the parameters are correlated to the physical processes they are assigned.

However, EEC modeling for impedance data is only one way to gain insights into the physical processes of the electrochemical system at hand. So-called “model-free” approaches for the analysis of impedance data exist, which provide a different path to the analysis. Impedance spectra are recorded in the frequency domain, and a transformation into the time domain is a common tool, that obtains the so-called distribution of relaxation times (DRT). However, DRT typically relies on solving a numerical integral using a regularization parameter,¹⁸⁹ which in turn drastically impacts the time domain spectra.¹⁹⁰ While some DRT approaches exist for battery applications,^{191,192,193} this work will focus on finding and validating a physically motivated EEC.

This short introduction into EIS and the “black box” problem of finding a physically meaningful EEC is by no means a complete picture of the theory, application, or prospects of EIS. The interested reader is referred to a recently published review¹⁸⁸, the various works of Bernard A. Boukamp on electrochemical impedance spectroscopy for solid-state ionics^{194,195} and the textbooks by Orazem & Tribollet¹⁹⁶ and Lasia¹⁵⁵, and the reference therein.

4 Spectroscopic Ellipsometry and Optical Modeling.

Spectroscopic ellipsometry will later play an important role in “watching” the formation of space charge layers with an accurate determination of thickness and concentration change. This section will describe the physical background, the working principle, and the important step of modeling the ellipsometry spectra. Ellipsometry measures the change in polarization of light when it is reflected at an interface between two materials or thin films. The first section is a quick recap of light polarization and polarization angles.

4.1 Light Polarization and Reflection.

The following description is textbook knowledge, and only the points most relevant for the measurement principles of ellipsometry are made. An in-depth explanation of the theory of polarized light can be found in *Polarization of Light* by S. Huard, 1997.¹⁹⁷

Monochromatic light as an electromagnetic wave can be described as three independent oscillations along the three space axes (x, y, z). In a transverse wave, the oscillation is perpendicular to the direction the wave propagates, which is the same as claiming that the electromagnetic field vector E is always orthogonal to the direction of motion. Setting the direction of motion to the z -axis leaves two oscillations along the x, y -axes, which are characterized by an individual amplitude and phase, but have the same frequency. The projection along the z -axis describes the time-dependent movement in x, y -plane, which is called the polarization of light. Generally, this is described by an ellipse, and thus the wave is called elliptically polarized. Two special cases are noteworthy here, which are linear and circular polarization. In linear polarization, the phase of x and y oscillation is equal, and the projection yields a straight line. If the phase difference is exactly $\pm 90^\circ$, a circular pattern arises in the projection. In optics, the axes are usually defined with respect to a surface that interacts with the light. The x -axis is defined parallel to the plane of incidence. Therefore, the y -axis is perpendicular to the plane of incidence. The electric field is then characterized by the parallel component p and perpendicular component s . Note that

the polarization state is fully described by the movement of the field vector E on an ellipse and can be expressed as $E = \begin{bmatrix} E_p \\ E_s \end{bmatrix}$. When the light wave reflects from any interface, the polarization state E is changed by the reflection matrix R , and the outgoing light wave is described by E' .

$$E' = \begin{bmatrix} E'_p \\ E'_s \end{bmatrix} = \begin{bmatrix} R_{pp} & R_{ps} \\ R_{sp} & R_{ss} \end{bmatrix} \begin{bmatrix} E_p \\ E_s \end{bmatrix} \quad \text{Equation 41}$$

The reflection matrix for isotropic materials is diagonal ($R_{ps} = R_{sp} = 0$) and therefore, the change of polarization can be described by R_{pp} and R_{ss} . The phase shifts between the incident and outgoing components of the light wave are expressed as δ_{pp} and δ_{ss} .

The change in the polarization state can be used to define the two parameters Δ and Ψ , which are derived from the equation for the fraction of the reflection coefficients R_{pp} and R_{ss} .

$$\frac{R_{pp}}{R_{ss}} = \frac{|R_{pp}|}{|R_{ss}|} e^{i(\delta_{pp} - \delta_{ss})} \quad \text{Equation 42}$$

$$\Psi = \arctan \frac{|R_{pp}|}{|R_{ss}|} \quad \text{Equation 43}$$

$$\Delta = \delta_{pp} - \delta_{ss} \quad \text{Equation 44}$$

These parameters are commonly called ellipsometric angles. Despite the nomenclature, the parameters do not have a physical interpretation with a direct correlation to the optical properties or thickness of a medium. Therefore, the analysis of data obtained in spectroscopic ellipsometry depends on an (empirical) model to fit the experimental data. The description and modeling of the

optical properties, especially those relevant for a spectroscopic experiment, are described in the next section.

4.2 Optical Properties and Modeling.

For a given material, the process of the transmission or absorption of a light beam can be described by the refractive index, which is typically a complex number $\bar{n} = n + ik$, where n is the real part, describing the phase velocity. The attenuation of the wave is determined by the extinction coefficient k . As this is a spectral property of the medium, the refractive index \bar{n} depends on the wavelength λ and can be expressed as $n(\lambda)$ and $k(\lambda)$. If more than one medium is present, the individual descriptions of the refractive indices are accompanied by the reflection (and therefore polarization) at the interface between the two materials. Under the assumption of plane-parallel reflection, the system is fully described by the complex refractive indices and the thicknesses of the materials.

The optical system modeling is now two-fold: On the one hand, the refractive index of a single layer can be modeled using various approximations, which will be described in the following. On the other hand, a model must be developed to describe the stack of the different materials with individual refractive indices and thicknesses to obtain useful information about the system.

For a single layer, the refractive index can be readily determined with a refractometer for materials in gas,¹⁹⁸ liquid,¹⁹⁹ and solid phases.²⁰⁰ Therefore, libraries exist for the most common materials and their phases, which contain data on the wavelength-dependent dispersion relation for specific phases of the material.^{201,202} If more than one phase is present within a layer for which the dispersion relation is of interest, effective medium approximations (EMAs) for composites to describe the macroscopic properties are commonly used.²⁰³ The EMA models inclusions of a guest material into a host material, usually under the approximation of a small guest concentration, which is illustrated in **Figure 9**. If the dispersion relations of the individual materials are known, the Bruggeman model (one EMA approach for optics) can account for spherical or ellipsoidal inclusions and can be used to calculate the effective refractive index of the composite material.²⁰⁴ The fraction of the guest material in the host material is the most important modeling parameter and fully determines the effective refractive index if the individual refractive indices are known. A work by A. Feldman²⁰⁵ provides a critical view of refractive index modeling in composite systems and concludes that the prediction of a model before experiments are conducted is difficult.

But generally a good model can be found after the experiments are done. The EMA will later be used to model the inclusion of Li^+ in the SSE as a first approximation for depletion and accumulation of Li^+ in SCLs.

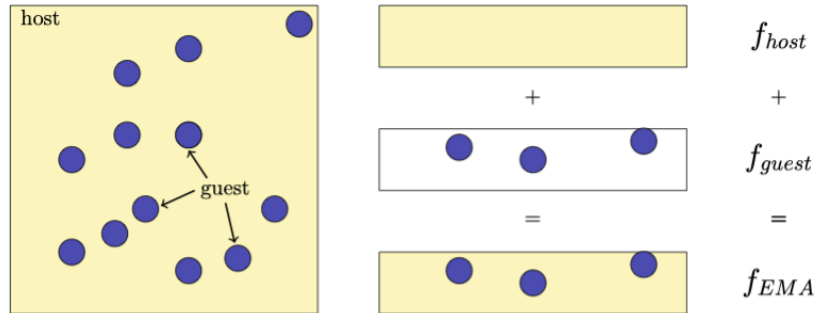


Figure 9. 2D schematic of an effective medium approximation, in which a small fraction of guest material is present in a host material. The optical properties of the composite can be calculated by the EMA, when the fraction and individual properties of guest and host are known.

Multiple studies have shown the validity of the Bruggeman model for ion-inserted semiconductors.^{206,207,208} The Bruggeman model was developed under the assumption that the composite material contains only a small fraction of guest material with ellipsoidal or spherical shape.²⁰⁹ In the first approximation, the guest material is assumed to be homogeneously distributed within the host material, and the fraction is only described by the volume fraction $c = V_{guest}/V_{host}$, where V describes the respective volume of host and guest. A chapter in the book “Ellipsometry at nanoscale” by J. Humlicek²¹⁰ provides a detailed analysis of the limitations of the Bruggeman approach and compares it to other models and, whenever possible, the analytical solution.

For a multilayer system with different layers denoted with i , the response can be modeled by the refractive indices of the individual layers $n_i(\lambda), k_i(\lambda)$, and their respective thickness d_i . For a system with n layers, there are $3n$ unknown parameters – two vectors (refractive indices) and one scalar quantity (thickness). Additionally, the interface between materials can introduce roughness parameters²¹¹ and mixed layers, which contribute to the overall optical properties in different

ways.²¹² **Figure 10** shows a stack of three layers with surface roughness indicated between layers 1 and 2 and a mixed layer between layers 2 and 3.

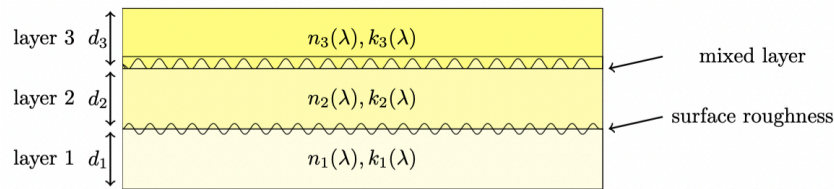


Figure 10. Schematic of a three-layer structure for the modeling of the optical response. Each individual layer is described by the refractive indices $n_i(\lambda), k_i(\lambda)$ and the thickness d_i . In addition to the individual components of layers 1-3, mixed layers as drawn between layers 2 and 3 or interface roughness as indicated between layers 1 and 2 can be present and influence the overall optical response.

In most cases, the refractive indices are either known from literature or can be measured on the bare material and the thicknesses are the parameters of interest.²¹³ Further reading on data analysis for spectroscopic ellipsometry can be found in a review by GE Jellison.²¹⁴

4.3 Working Principle of Spectroscopic Ellipsometry.

With the basics of light polarization covered in the previous sections 4.1 and 4.2, the following covers the working principles and explains the experimental technique of “nulling ellipsometry” used in this work. An overview of the applications of ellipsometry for thin-film characterization can be found in “Spectroscopic Ellipsometry: Practical Application to Thin Film Characterization” by G. N. Tompkins and J. N. Hilfiker, published by Momentum Press, 2015.²¹⁵

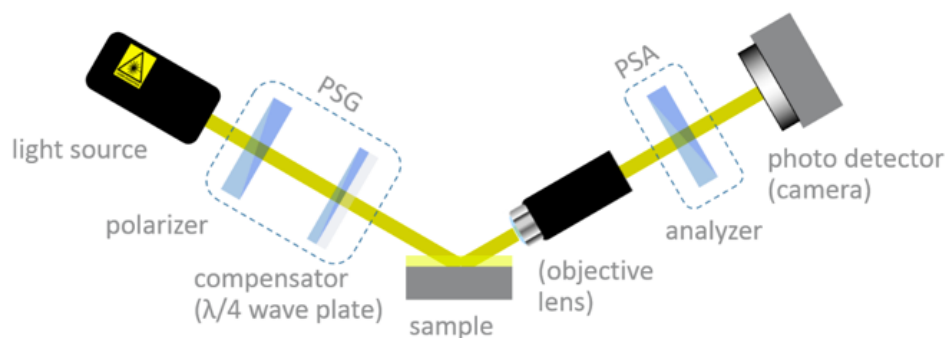


Figure 11. Schematic drawing of an ellipsometer setup with a light beam direction from left to right. A linearly polarized light beam is produced by the polarization state generator (PSG) and after the reflection from the sample surface analyzed by the polarization state analyzer (PSA). *Graph reproduced from reference 216.*

Spectroscopic ellipsometry is based on measuring the polarization change throughout a spectrum of wavelengths. As depicted in **Figure 11**, a light source provides the initially unpolarized beam, which is polarized into a defined, typically linear, polarization state using the polarization state generator (PSG). Combined with the compensator, which is an optical retarder and shifts one polarization component by $\lambda/4$ in the case of a “quarter-wave plate”, arbitrary polarization states (linear, circular, or ellipsometric) can be generated. After the reflection from the sample, the beam is collimated using a lens and analyzed by a polarization state analyzer (PSA) with a photodetector. Both PSA and PSG are so-called polarizers, a common device found in optical setups, which can selectively suppress or transmit light of a certain polarization state. In “nulling ellipsometry”, the PSA is adjusted to detect the minima in intensity. Based on a linearly polarized incident light beam

on the sample, the beam after reflection from the sample is in an elliptical polarization state. In the case of a non-depolarizing sample, which is equivalent to finding an elliptically polarized light beam that exhibits linear polarization after the reflection from the sample. A linearly polarized light beam can be extinguished by setting the analyzer at a 90° position with respect to the polarization direction. In practice, the compensator is fixed to a certain angle, and the angle of the PSG and PSA are varied until the signal of the photodetector vanishes. While this requires an iterative procedure to improve the accuracy, it is by far the most common ellipsometry technique. One “nulling ellipsometry” measurement determines the ellipsometric angles Δ and Ψ . To reconstruct information about the sample, a variation of the angle of incidence (AOI) or the wavelength of the incident light beam is necessary. For further reading on the application and principles, the reader is referred to the work of H. Fujiwara.²¹⁷

5 Experimental Setups and Materials.

In the last chapters, the concepts and theory of the experimental techniques and the investigated material class were described in detail. The following section gives specific information about the model electrolyte, the electrode materials, and the experimental setups used in this work.

5.1 A Model Solid-State Electrolyte: Ohara LICGC™.

The model electrolyte used in this work is a NASICON-type electrolyte produced by Ohara Inc. with the trade name LICGC™ (Lithium Ion Conducting Glass Ceramic).²¹⁸ The modest ionic conductivity of the electrolyte is in the order of $10^{-4} S/cm$ at room temperature and is reproducibly found across sample batches, which makes experimental studies easily comparable and reproducible. The proven stability in ambient air and moisture makes the experimental designs independent of an inert atmosphere, which will be used across the investigations of this work.

The main crystalline phase in the LICGC™ is $Li_{1+x+y}Al_x(Ti,Ge)_{2-x}Si_yP_{3-y}O_{12}$, but the exact stoichiometry is not stated by the manufacturer. Further, a phase of $AlPO_4$ is present and visible in the scanning electron microscopy images shown in reference 223. The specimen used in this work are of 19 mm diameter with a thickness of 150 μm and are used as received with no further cleaning steps. A general characterization of the samples, including surface roughness, grain size distribution, and XRD measurements, can be found in reference 231.

5.2 Electrode Fabrication.

For EIS measurements and the application of bias potential, metal electrodes were evaporated using either (for the studies in sections 6.1 and 6.2) an L560 (Leybold, Germany) e-beam evaporator with an IC6000 deposition controller (Inficon, Switzerland) or (for all other studies) a MICO (Tectra, Germany) thermal evaporator. The evaporation rates were set to 1 $\text{\AA}/s$ with a final thickness of 25 nm for all materials. All electrodes are fabricated using a stainless-steel mask with an inner radius of 7.5 mm, resulting in an electrode area of 1.76 cm^2 .

5.3 Impedance Setup and Analysis.

A VSP300 potentiostat from Biologic, France²¹⁹ was used to carry out the impedance studies in this work. For all impedance measurements, a sinusoidal excitation amplitude of 10 mV was applied, and spectra were recorded in a frequency range from 5 MHz to 0.5 Hz. A waiting time of 3 frequency periods is set before the acquisition starts at each frequency point, which is averaged over 5 periods. For SPEIS measurements, the bias potentials were applied vs. counter electrode with a waiting time of 15 minutes, for which the potentials are held before measuring the impedance spectrum.

The impedance spectra were analyzed and fitted using the “EIS Data Analysis 1.3” software by A.S. Bandarenka.^{220,221} The fitting was done with a hybrid “Powell” algorithm in amplitude weighting mode.

5.4 Electrochemical Cell Setup.

For the electrochemical measurements, the samples are placed in a “PAT Cell” (EL-CELL, Germany), which was assembled inside an Argon-filled glovebox ($O_2 < 1$ ppm, $H_2O < 1$ ppm). Polished stainless-steel plungers inside the cells contact the metal electrode without further application of pressure, which leaves the actual pressure unspecified. The cells are He-leak tested²²² and, therefore, can be taken out of the glovebox without contamination of the sample. The “PAT cell” is connected to the potentiostat through a “PAT stand” (EL-CELL, Germany) with 3 *m* wires.

For the temperature variation measurements, the cells are loaded into a custom-built temperature chamber with a simple PID controller and a thermometer tip within the steel case of the cell. At a given temperature, the thermodynamic equilibrium is assured by waiting for one hour prior to EIS or SPEIS measurements.

5.5 Optical Measurements.

The optical measurements require the top surface of the sample to be accessible by the instrument. In addition, the ellipsometry measurements require that the sample is fixed at a certain temperature, which is assured using a temperature stage – requiring the cell to be thin enough to easily transport heat to the cell, which is assured by a very thin cell layout. For alignment reasons, the sample should be plane parallel to the stage. The sample layout on top of the sample stage is shown in **Figure 12**.

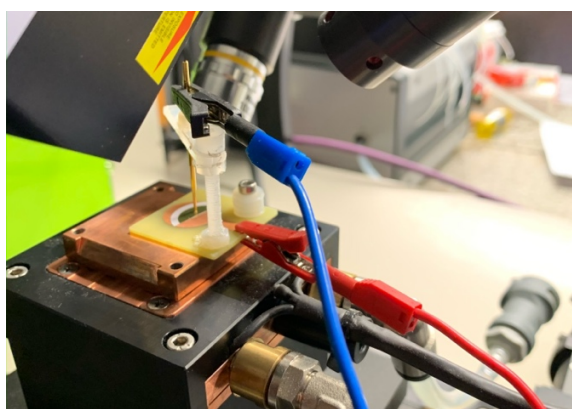


Figure 12. Photograph of the sample stage of the spectroscopic ellipsometry. Red and blue clamps and cables are the working and counter electrode, respectively. The SSE is placed on a copper surface and held by an Au spring, which also serves as the electrical connection for the counter electrode. The copper plate beneath the sample is the temperature stage, assuring a fixed temperature throughout the measurements. The optical lens in the back is the detector. The light beam originates from the left of the picture.

For all ellipsometry measurements, an EP4 imaging ellipsometer (Accurion, Germany) was used either in combination with a solid-state laser (658 nm) or, in spectroscopic measurements, with a stabilized xenon arc lamp and a grating monochromator. The angle of incidence was set to 65° for all *in situ* ellipsometry measurements. With an SP-150 potentiostat (Biologic, France), the polarization potentials were applied, and the samples were left to rest at any given polarization for 2.5 hours. The software used to control the ellipsometry measurements also serves as the modeling environment, as the “EP4Model” module is contained. For the bare electrolyte, new material is

created and parameterized using a second-order Cauchy model. Using this new material, the EMA uses the material as a host and lithium as a guest structure.

6 Investigation of Space Charge Layers in Solid-State Electrolytes.

The small changes in charge carrier concentrations in layers only a few hundred nanometers wide make experimental evidence hard to come by. The following chapter provides the original findings of this work, which reveal the nature of space charge layers in solid-state electrolytes.

6.1 Measuring the Spatial Extent with Spectroscopic Ellipsometry.

The following section is based on a first-author publication in Wiley's Advanced Materials journal, entitled "Characterization and Quantification of Depletion and Accumulation Layers in Solid-State Li⁺-Conducting Electrolytes Using *in Situ* Spectroscopic Ellipsometry".²²³ The article is open access under the terms of the Creative Commons Attribution License and can be found in Appendix 9.3.

Spectroscopic ellipsometry is a well-known technique to determine the thickness of thin layers accurately.²²⁴ While mostly used for film thicknesses of synthesized films, it has been used to monitor the growth and swelling of thin organic films.^{225,226} In a recent study, the Li⁺ insertion into LiMn₂O₄ was investigated with spectroscopic ellipsometry combined with FEM analysis. However, no model for the changes in refractive index upon lithiation are developed in this work, and the analysis remains qualitative.²²⁷ As the theory (see section 2.4) suggests, the formation of SCLs strongly depends on the electrochemical potential difference between the electrode and electrolyte. Under blocking conditions, in which the measurements were taken, this implies that a change in bias potential leads to a formation of SCLs next to the Au electrodes. The experimental setup shown in **Figure 12** allows forming SCLs while observing the change in light polarization. The *in situ* approach rules out inhomogeneity in the sample surface, the geometric path of the light beam, and possible hysteresis of the electrochemical state. As introduced in section 6.2, impedance spectroscopy and spectroscopic ellipsometry can be combined to conduct optical and electrochemical investigations simultaneously.

The following section is divided into three major parts, beginning with the observed changes in ellipsometry spectra upon polarization, followed by the optical modeling of the SCL, and concludes with the application of the model to find SCL thicknesses and concentrations.

The changes in spectroscopic angles for different polarizations are shown in **Figure 13**, where the spectrum at 0 V bias is subtracted. A direct physical interpretation of the raw data, i.e., the ellipsometric angles Δ and ψ , has not been reported in the literature. The application of a bias potential clearly leads to a change in the spectroscopic angles with a change in Δ of up to 0.6% deviation in **Figure 13A**). For higher bias potentials (-1 V and 1 V), the changes are bigger compared to the smaller biases. However, the impact is not symmetric – an observation that, even without further data analysis, points to an asymmetry in the formation of the depletion vs. accumulation layer.

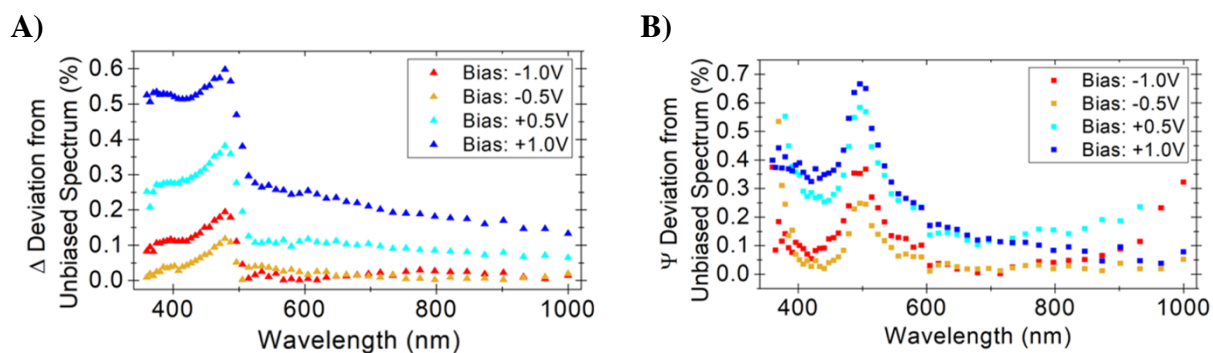


Figure 13. Relative changes in spectroscopic angles upon application of bias potential. Although variations are small, compared to the statistical error of 0.05%, a relevant change occurs for all applied bias potentials. *Graphs adapted from Adv. Mater. 2021, 33, 2100585, © 2021 The Authors. Advanced Materials published by Wiley-VCH GmbH.*

While the relative deviations are below 1 %, the changes are still significantly above the statistical error of 0.05% and therefore considered relevant for the subsequent fitting process.

A model representing the layer structure, including the depletion/accumulation layer, is needed to derive quantitative results from these changes. The layer stack, shown in **Figure 14**, consists of three different materials with individual complex diffractive indices and thicknesses. This leads to a total of 6 free fitting parameters, three thicknesses (scalar), and three diffractive indices (complex vectors). The 25 nm gold electrode, thermally evaporated as described in section 5.2, is represented

by a literature model “Au-Gold_Q-Sense-Quarz” found in the EP4Model software, see section 5.5. The only fitting parameter for the Au layer is, therefore, the thickness, which is expected to match the deposition thickness of 25 nm.

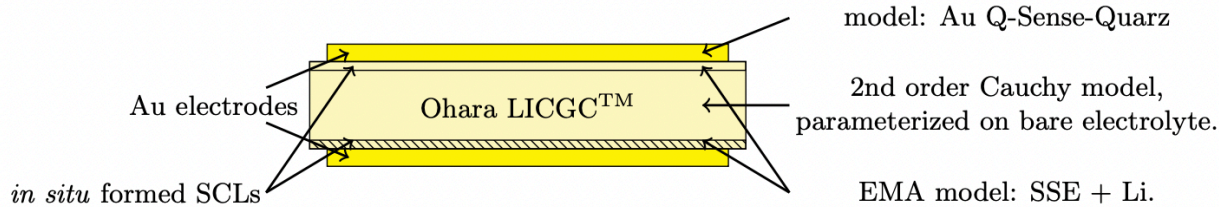


Figure 14. Drawing of the sample with the different layers of materials and the *in situ* formed SCLs. The models for the different materials and layers are listed on the right, with a literature model for the Au electrodes, a 2nd order Cauchy model for the SSE, and the EMA model for the SCLs.

For the Ohara LICGC™, no optical model describing the complex diffraction index is known in the literature. However, other glass-ceramics for different applications have been successfully fitted with Cauchy models.^{228,229,230} Therefore, the bare SSE was measured separately to determine the parameters of the Cauchy model. The ellipsometry spectrum of the bare SSE is shown in **Figure 15A)** together with the fit of a Cauchy model to the complex diffractive index, also shown in **Figure 15B)**. The SSE is used as the substrate in the optical layer stack for fitting purposes. No free fitting parameters are set for the SSE substrate, as the optical properties are determined, and its thickness is assumed to be infinite, which is a reasonable assumption considering the total transmission of only 3.8 % through the Au/SSE/Au sample.

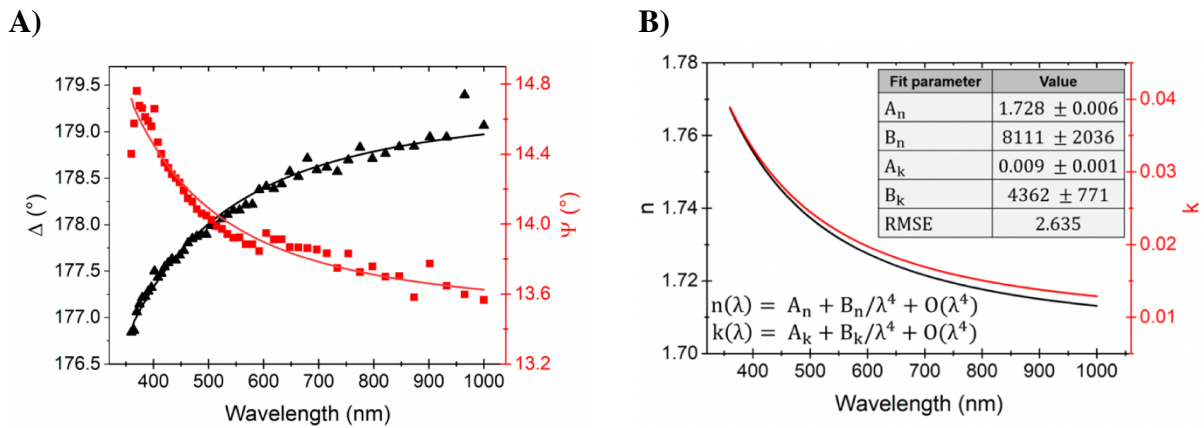


Figure 15. Analysis of the bare SSE. **A)** Ellipsometry spectra recorded on a pristine SSE combined with a fit using a Cauchy model. **B)** Fitted dispersion relation using a second-order Cauchy model. *Graphs reproduced from Supporting Information of Adv. Mater. 2021, 33, 2100585, © 2021 The Authors. Advanced Materials published by Wiley-VCH GmbH.*

The description of the SCL relies on the fact that the accumulation and depletion of Li^+ can be viewed as SSE material with additional or less Li^+ . A Bruggeman model, introduced in section 4.2 for the effective medium approximation (EMA), with the SSE representing the host material and lithium the guest material, is therefore used to describe the SCL. The diffractive index is then determined by the concentration of Li^+ inside the SSE, which leaves the concentration and thickness as free fitting parameters. The optical properties of the SCL based on a depletion (-8% volumetric lithium, assumed at -1 V) and accumulation (+3% volumetric lithium, assumed at 1 V) are calculated and shown in **Figure 16**, where a negative bias indicates a depletion and positive bias an accumulation, respectively. This verifies the model's sensitivity to a change in optical properties, which will now be used to fit the equation to experimental data.

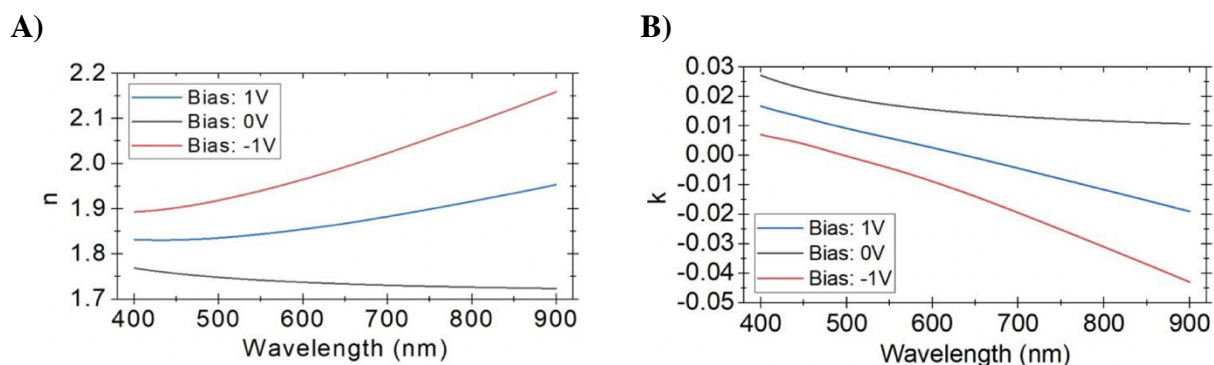


Figure 16. Sensitivity of the developed Bruggeman model to the concentration change. The calculations are based on -8 vol% and 3 vol% lithium, representing SCL for -1 V and 1 V, respectively. *Graphs reproduced from Supporting Information of Adv. Mater. 2021, 33, 2100585, © 2021 The Authors. Advanced Materials published by Wiley-VCH GmbH.*

The final optical model used to fit the ellipsometry spectra under different bias potentials therefore only contains two free parameters: the SCL thickness (d_{SCL}) and the concentration change (c_{SCL}).

Table 3. Fit parameters based on fits for 9 spectra recorded for different bias potentials. An asymmetry in the thicknesses can be observed in both thickness and concentration change of the formed SCLs. Overall, the errors are below 10 % for the thicknesses, except for the data at no applied bias potential – which correlates to a vanishing SCL. *Data reproduced from Supporting Information of Adv. Mater. 2021, 33, 2100585, © 2021 The Authors. Advanced Materials published by Wiley-VCH GmbH.*

Bias [V]	-1.0	-0.75	-0.5	-0.25	0.0	0.25	0.5	0.75	1.0
SCL thickness d_{SCL} [nm]	190.7 ± 19.0	189.5 ± 16.8	189.9 ± 13.2	58.2 ± 9.4	21.7 ± 19.6	138.7 ± 15.6	318.7 ± 17.1	326.0 ± 13.2	321.8 ± 15.7
SCL concentration c_{SCL} [vol%]	-8 ± 1	-7 ± 1	-8 ± 1	-3 ± 1	-5 ± 3	2 ± 1	3 ± 2	4 ± 2	3 ± 2
Fit quality (RMSE)	4.5	5.9	9.0	9.9	9.4	8.9	6.4	9.9	11.5

The fit results for bias potentials between -1 V and 1 V are shown in **Table 3**. The change in lithium concentration ranges from -8 vol% to +4 vol%, for negative to positive potentials, respectively. It must be noted that this change is a volumetric concentration change based on the mixing of lithium into SSE material. Due to the unknown Li^+ -concentration of the bulk electrolyte,

no conclusions about the Li^+ -concentrations in the SSE's crystal lattice can be drawn. The asymmetry is best explained considering the different boundaries for Li^+ -concentration. As explained in section 2.4, the Li^+ -concentration is limited by the mobile Li^+ -concentration (for Li^+ depletion) and the free vacancy concentration (for Li^+ accumulation). If the vacancy concentration is not exactly double the mobile Li^+ -concentration, the same amount of charge (i.e., the absolute number of Li^+) cannot be depleted/accumulated in a layer of equal width. This is not only reflected in the Li^+ -concentration change, but can also be found in the fitted thicknesses in **Table 3**. As the electrochemical system is in blocking conditions, the net charge of the accumulation layer must equal that of the depletion layer. The wider accumulation layer, seen for positive potentials as described in section 5.5, is less concentrated but must hold the same total charge as the thinner depletion layer with a higher deviation in concentration. The concentration fraction of occupiable vacancies to mobile Li^+ is estimated to be ca. $2/3$, meaning that the bulk concentration is two-thirds of the maximum Li^+ -concentration.

Although the semi-empirical, three-layer model performs reasonably well, a few limitations must be considered:

On the one hand, the model is relying on a true sharp separation of the layers like the abrupt approximation for SCLs in semiconductors and thereby neglecting the fact that any change in concentration will not occur in a step but rather a smooth, sigmoid-like distribution as suggested by the theoretical calculations introduced in section 2.4. The small concentration changes (-3 vol%) at low bias potentials (-0.25 V) indicate that the layers indeed form gradually, and the full depletion/accumulation is not reached for low bias potentials. On the other hand, the approximation of forming volumetric Li^+ -content inside the electrolyte material is rather simple. A more elaborated model on the changes of optical properties of the SSE with accumulated or depleted Li^+ is therefore suggested for future measurements. For example, several stoichiometries with varying Li^+ -concentration in bulk could be measured in a non-biased state to investigate the impact of Li^+ -content on optical properties. Not only could this be used to validate and improve the model at hand, but the partition of mobile Li^+ in the stoichiometric Li^+ -content could be determined.

Conclusively, the thickness of the SCL forming at the electrode/electrolyte interface can be determined using spectroscopic ellipsometry, and the semi-empirical model developed. The findings presented in this section are direct evidence for the suspected SCL formation in SSE, and

the thickness of these layers cannot be considered negligible. The suspected asymmetry can be measured and quantified to be the fraction between available and occupied Li^+ -vacancies. This is especially important for theoretical models, where parameterization is inherently complex due to the unknown ion concentrations. A given fraction of accumulable and depletable charges allows us to describe the SCL formation at least qualitatively by theoretical calculations. However, the ellipsometry measurements are limited to “optical” properties and do not give insight into the resistance caused by this layer. As an electrochemical phenomenon, the SCL is investigated using electrochemical impedance spectroscopy (EIS) to gain insight into the electrochemical properties, such as resistance and capacitance. The following section explores impedance measurements and model building to describe and analyze the SCL effect.

6.2 Determining Electrochemical Properties with Electrochemical Impedance Spectroscopy.

The main ideas and results presented in this section are published in ACS Applied Materials & Interfaces, entitled „Properties of the Space Charge Layers Formed in Li-Ion Conducting Glass Ceramics”, which can be found in reference 231. Permission to reuse was granted by ACS for use in this thesis, found in Appendix 9.1. The full paper can be found in Appendix 9.4.

With the prerequisites of section 3 in mind, the use of EIS to measure the counterpart to double layers of liquid electrolytes becomes self-evident. Not only does EIS allow to measure resistances and capacitances in electrochemical systems on very different lengths- and timescales, but the simultaneous modification of the boundary conditions, here the bias potential, can be achieved. As described in the methodology, see section 3.1, staircase potential electrochemical impedance spectroscopy (SPEIS) can be used to swiftly measure the impedance response of the electrolyte at different DC potentials. As this is the first study of its kind, the same model material system as for the optical measurements is used: an SSE in between two blocking electrodes.

As described in the previous section on spectroscopic ellipsometry measurements, the SCL phenomenon can be “activated” by applying a bias potential. Assuming some impact of the SCL on the impedance response of the electrochemical cell, a change in applied bias potential should correlate with a change in impedance. **Figure 17** shows typical impedance spectra on different scales with a variation of the bias potential. Despite the fact that no analysis of the data should be done without an electrical equivalent circuit (EEC) describing the electrochemical processes, it can be seen that the applied bias potential has an impact on the impedance in the low-frequency (**Figure 17A**) and mid-frequency (**Figure 17B**) regime.

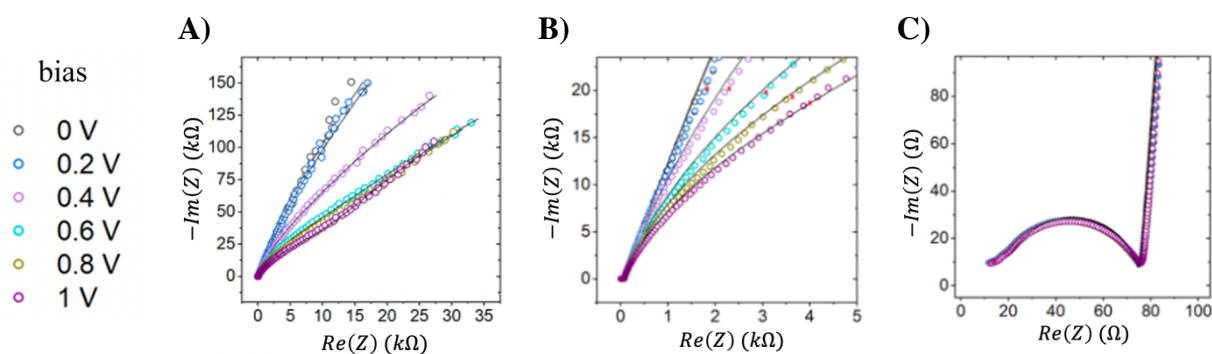


Figure 17. Influence of the bias potential on the impedance of an SSE in blocking conditions in different frequency regions. **A)** all frequencies, **B)** mid frequencies and **C)** high frequencies. The impact of the bias potential is limited to mid and low frequencies, which are generally associated with slower processes such as charge accumulation at interfaces. The lines show the fits of the EEC to the data, showing very good agreement of the fit results. *Graphs reprinted with permission from 231. Copyright 2021 American Chemical Society.*

To find a suitable and physically meaningful EEC, as described in section 3.3, one must consider the possible electrochemical processes of the Au/SSE/Au cell. The blocking electrodes should neither cause a high resistance nor a capacitance and will be included in the uncompensated resistance – an element typically found to account for connection resistances.²³²

The SSE can be represented by a resistance linked to its ionic conductivity, geometry, and geometric capacity. The geometric capacity is caused by the SSE’s polarizability, as it is a dielectric medium in between two electrodes, and the capacity is determined by the following equation:

$$C_{geom} = \frac{\epsilon_0 \epsilon_R A}{d} \quad \text{Equation 45}$$

where A is the sample area, ϵ_0 and ϵ_R the dielectric constants of vacuum and the bulk SSE, and d the sample thickness.

Furthermore, the two interfaces of the SSE towards the electrodes must be considered in the EEC. Adjacent to the Au-electrode, a very thin double layer (DL) structure is formed and can be described by a constant phase element.²³³ Notably, this DL is not the same as the SCLs, but rather conceived as a layer of single ions on the Au surface – like the Helmholtz layer in LEs. Furthermore, the impedance spectra shown in **Figure 17** indicate the presence of a third contribution. The strongly depleted SCL near the positive electrode will form a layer of lower ionic conductivity, as the conductivity is proportional to the Li^+ -concentration in SSEs.²³⁴ In parallel to

this SCL resistance, the Li⁺-depleted layer will also introduce a capacitance as it acts as an effective barrier to Li⁺. The SCL capacitance can be described as a geometric capacitance, where the thickness is equal to the SCL width. No impact on the impedance is expected to be introduced by the accumulation layer, where a wider layer naturally exhibits a lower capacitance. The charge accumulation does not lead to an increase in resistance but rather a decrease.

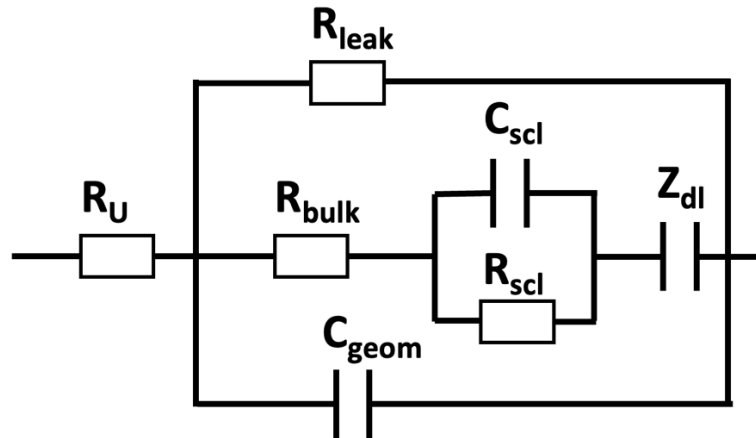


Figure 18. Physical EEC for the SSE in blocking conditions. A central resistance, R_{bulk} , accounts for the electrolyte resistance and is in series to the SCL elements and the compact double layer (Z_{dl}). In parallel, a geometric capacitance and a leakage resistance represent the SSE as a dielectric with small electronic leakage.

The equivalent circuit based on this line of arguments is shown in **Figure 18** with the addition of a leakage resistance to account for electronic leakage currents. However, the model must be validated by proving that each element of the EEC corresponds to the assigned electrochemical cause. By comparing the external condition with a subsequent impact on the impedance, we can deduce that the EEC elements are assigned to the correct cause. **Table 4** shows the expected influences of the three external conditions on the EEC parameters.

The interface conditions, i.e., the bias potential and electrode metal, should not influence any phenomena occurring in the bulk of the electrolyte, such as the bulk conductivity and geometric capacitances. Important to notice is that the frequently included grain-boundary impedance, represented by an additional RC-element,^{235,236} is not explicitly present but rather included in the bulk resistance. The temperature impact on the bulk conductivity should represent an Arrhenius behavior²³⁷ with well-defined activation energy. For a material system close to the one used here,

the activation energy is roughly 0.35 eV.²³⁸ Up to now, no predictions existed about the impact of temperature on the geometric capacitance, closely linked to the dielectric constant.

Table 4. Expected impact of external conditions on EEC parameters, to create a verifiable physical model.

	R_{bulk}	C_{geom}	$R_{\text{scl}} \& C_{\text{scl}}$	Z_{dl}	R_{leak}
Bias potential	No	No	Yes	Yes	Unknown
Temperature	Arrhenius	Yes	Yes	low	low
Electrode metal	No	No	Yes	Yes	No

With these assumptions set in place, it is now time to verify our impedance model with experimental data. Before evaluating the EEC parameters, a good fit quality must be ensured. **Figure 19** shows the impedance spectra for three different electrode metals and 10 different temperatures, including a solid line for the corresponding fits.

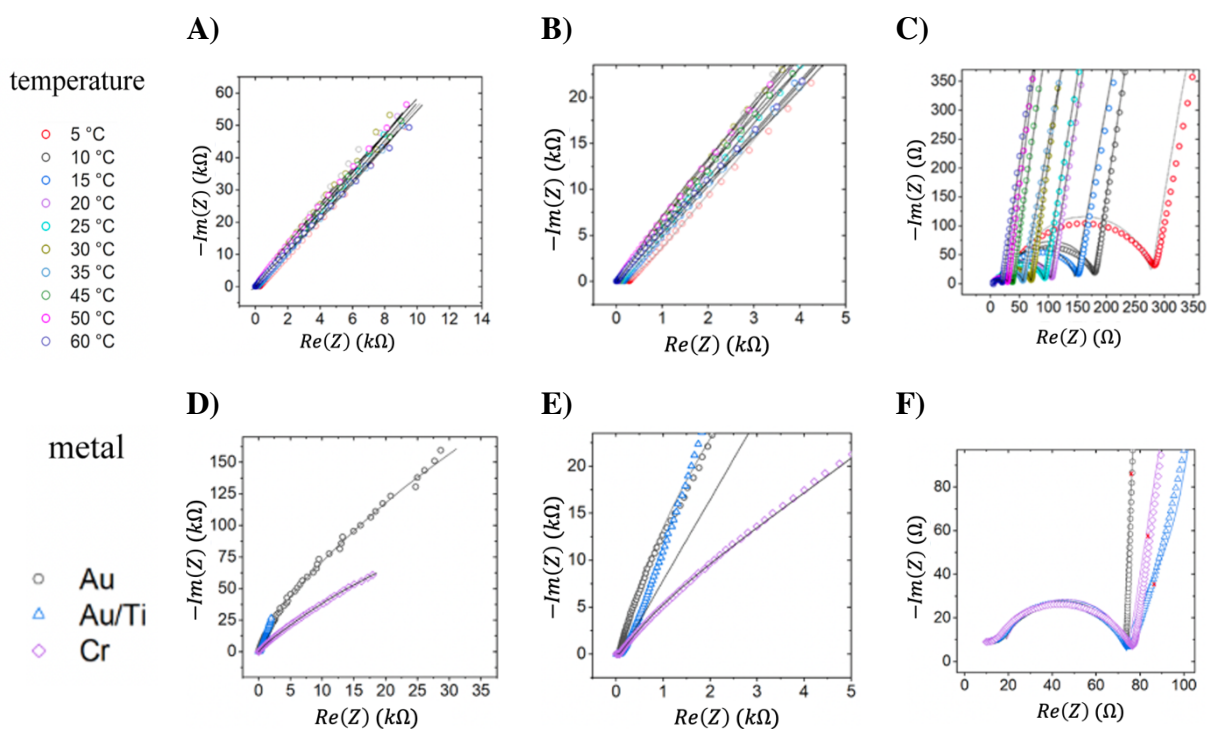


Figure 19. Impedance spectra recorded for **A) - C)** 10 different temperatures and **D) - F)** three different electrode metals, shown in three different regions from low to high frequencies, from left to right, respectively. *Reprinted with permission from 231. Copyright 2021 American Chemical Society.*

As expected, the temperature impacts the high-frequency region (**Figure 19 C**)) and leaves the mid- and low-frequency regions almost untouched. The variation of the electrode metal has the opposite effect, only impacting low and mid-frequency regions. It can therefore be concluded that the low and mid-frequency impedances are caused by an interface phenomenon.

The EEC parameters for the different electrode metals are shown in **Table 5**. As expected, the values for C_{geom} , R_U , and R_{bulk} are unchanged regardless of the interface condition. All other parameters change with the choice of electrode metal, confirming that their origin is indeed an interface phenomenon.

Table 5. EEC parameters including errors for different electrode metals. *Reprinted with permission from 5. Copyright 2021 American Chemical Society.*

	Au		Cr		Au/Ti		Unit
	Value	Error	Value	Error	Value	Error	
C_{geom}	3.74E-09	1.10E-10	3.53E-09	1.16E-10	3.82E-09	1.60E-10	[F/cm ²]
C_{scl}	1.22E-05	1.85E-06	2.40E-05	4.80E-06	6.68E-06	1.65E-06	[F/cm ²]
R_{U}	16.73	0.45	21.77	0.53	16.18	0.92	[Ohm]
R_{bulk}	55.87	0.77	60.85	0.87	57.59	1.14	[Ohm]
R_{scl}	6319.42	3963.79	1353	718.17	22.05	1.82	[Ohm]
R_{leak}	1.52E+06	6.46E+05	5.53E+05	2.08E+05	4.01E+07	1.48E+07	[Ohm]
C'_{dl}	1.14E-06	1.07E-08	3.03E-06	3.04E-08	7.56E-06	1.14E-07	[F/cm ²]
α_{dl}	0.97	1.57E-03	0.90	1.80E-03	0.93	3.12E-03	

With the knowledge of the previous section on spectroscopic ellipsometry that the SCL should be of several hundred-nanometer thicknesses, **Figure 20** shows the impact of the applied bias potential on the impedance parameters. **Figure 20A)** and **Figure 20B)** show that the bulk parameters (C_{geom} , R_{bulk}) are not impacted by the bias potential. However, the double layer capacitance (**Figure 20C)**) - interpreted as a very thin layer of ions right next to the electrode – shows a symmetric increase of capacitance, indicating a thinning layer. Considering that this layer is formed in between electrode and electrolyte, and therefore assuming the dielectric constant to be that of vacuum, the thickness of this layer at 1 V can be calculated to be 0.7 nm, equal to 3.8 Li^+ radii. The qualitative behavior of the DL capacitance matches a literature report on oxygen SSEs.²³⁹ In our recent study, which can be found in Appendix 9.2, the temperature dependency of the double layer capacitance was analyzed, and a positive correlation was found.²⁴⁰ The dominant factor is suspected of lying in the concentration change of mobile Li^+ as the temperature increases and thus increasing the capacitance. A possible explanation for the decrease in leakage resistance with increasing bias potential is the higher polarization of the material forming electronic pathways. However, this is out of the scope of this work.

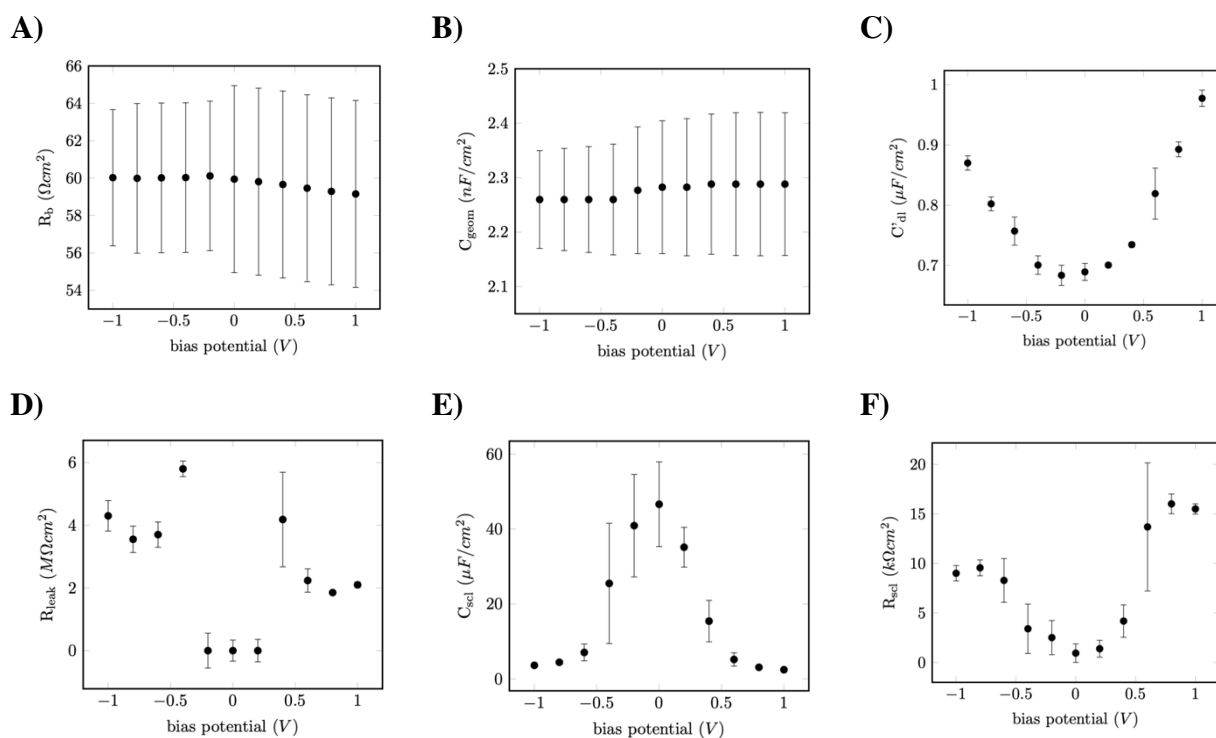


Figure 20. EEC parameters for bias potentials between -1 V and 1 V were recorded at room temperature (25 °C) with an Au electrode. The properties of the bulk, namely R_b and C_{geom} , shown in **A)** and **B)** are independent of the applied bias potential. A symmetrically increasing double layer capacitance, shown in **C)**, indicates the formation of a thin DL with a decreasing thickness. The electronic leakage, **D)**, strongly depends on the applied potential and seems to be “activated” by the application of a potential. **E)**, **F)** show the properties of the SCL with a decrease in capacitance (indicating a growing layer) and an asymmetric increase in resistance. *Adapted with permission from 231. Copyright 2021 American Chemical Society.*

The behavior of the SCL properties, C_{scl} and R_{scl} , can be explained as follows: As we already know, a layer of complete depletion will form upon application of a bias potential and gradually grow into the electrolyte. Assuming a perpendicular growth as indicated by the optical studies, the capacitance of this layer can be treated as the result of a plate capacitor, with the thickness being that of the SCL. However, when calculating the thickness using the plate capacitor equation (Equation 22) it is important to notice one of the major limitations of this approach. As the dielectric constant of the SCL is unknown, in a first approximation, the dielectric constant of the bulk is used, which is determined from the geometric capacitance C_{geom} . Although the uncertainty is hard to quantify, as the accumulation or depletion of Li^+ will change the dielectric properties of

the bulk material, the observed qualitative trend in SCL thickness is unaffected. A comparison can be made, however, to the thicknesses determined from spectroscopic ellipsometry, shown in **Table 3**. **Figure 21** shows the calculated depletion layer thicknesses from EIS compared to the thicknesses determined by spectroscopic ellipsometry and the corrected dielectric constant. Although the increase in SCL thickness is qualitatively observed with both spectroscopic ellipsometry and EIS analysis, a strong deviation can be observed in **Figure 21A)** with a plateau formation in the thickness determined by ellipsometry.

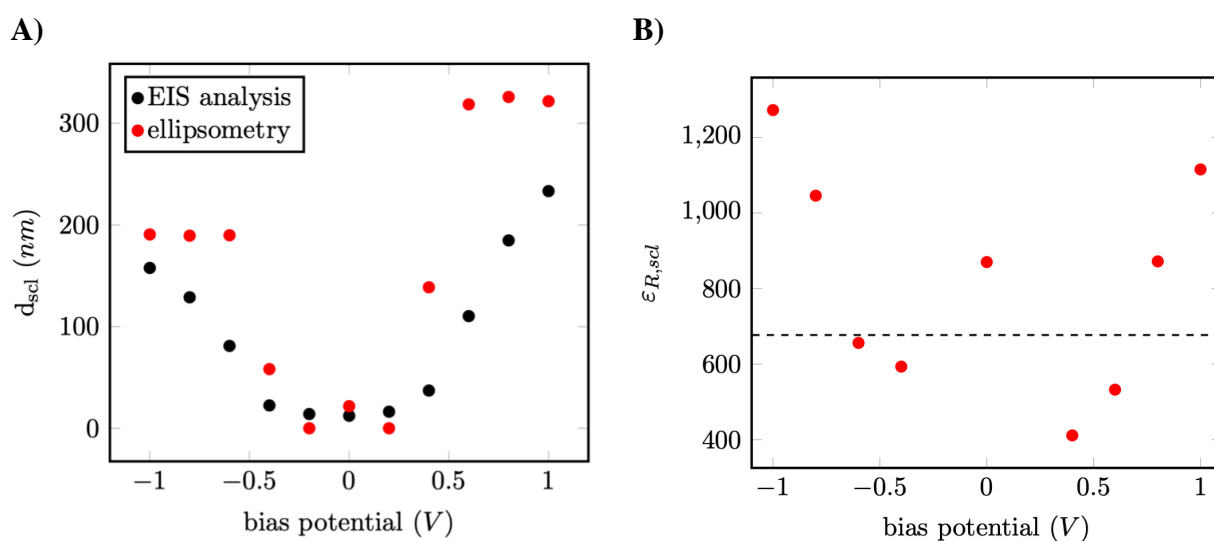


Figure 21. **A)** Comparison of SCL thicknesses determined using spectroscopic ellipsometry and electrochemical impedance spectroscopy. Although both are on the same order of magnitude and the general trend is similar, the plateau formation for high potentials ($> \pm 0.5$ V) is only observed in spectroscopic ellipsometry data. **B)** Corrected relative dielectric constant calculated based on the thickness determined with spectroscopic ellipsometry and capacitance from EIS analysis. *Data adapted with permission from Ref 231. Copyright 2021 American Chemical Society. Data adapted from Adv. Mater. 2021, 33, 2100585, © 2021 The Authors. Advanced Materials published by Wiley-VCH GmbH.*

A layer of this form, depleted of Li^+ and up to a few hundred nanometers wide, will naturally form a resistance, shown in **Figure 20F)**. The resistance increases when a bias potential is applied. However, the asymmetry in the observed resistance is not expected as the cell setup is fully symmetric with a two-electrode configuration for SPEIS measurements.

The values of the resistance, peaking at $16 \text{ k}\Omega\text{cm}^2$ for positive potentials show the detrimental effect of the SCL on the charge transfer at the SSE/electrode interface. Conclusively, it has been

shown that EIS, together with a carefully developed and physically validated EEC, can not only reveal the resistance but can be used to calculate the thickness, assuming unchanged dielectric properties. In the approximation of a compact and perpendicularly growing layer with a different Li^+ -concentration than the bulk, this layer can be thought of as an ionic conductor itself in co-existence with the bulk of the original SSE. As such, it is a reasonable pursuit to find the electrochemical properties such as ionic conductivity and activation energy of this newly “formed” material. Therefore, the next section describes the evaluation and interpretation of impedance spectra measured at various temperatures. In addition to the calculation of the properties of this layer, the temperature variation also allows to compare the results to theoretical predictions further. For theoretical simulations, the temperature is usually an easily accessible parameter, making a study on the effect of temperature on SCL formation relevant for the validation of thermodynamic and electrochemical models for SCLs.

6.3 Temperature Dependence of Space Charge Layer Properties.

As introduced in section 2.3, the Debye length is a common measure in liquid electrolytes for the spatial extent of the diffuse double layer into the electrolyte. Qualitatively, the thickness of the SCL should be proportional to the square root of the temperature, which is easily verifiable. The mentioned uncertainty caused by the ignorance of the true dielectric constant of the SCL is not relevant, as are any other proportionality constants between capacitance and thickness.

The ideas, graphs, and data shown in this section are primarily based on a first-author publication in ACS Applied Materials and Interfaces, entitled „Li⁺ conductivity of space charge layers formed at electrified interfaces between a model solid-state electrolyte and blocking Au-electrodes”, which can be found in reference 241.

The same blocking conditions, i.e., a gold electrode with no charge transfer over the interface, as in section 6.2 are used, and therefore the same EEC, shown in **Figure 18**, is used for fitting the recorded impedance spectra at different temperatures. The following section begins with observations of the temperature impact on the impedance, followed by the analysis of the SCL-related properties, a comparison of the observed thicknesses to a theoretical model, and concludes with a detailed description of the nature of Li⁺ conductivity inside the SCLs.

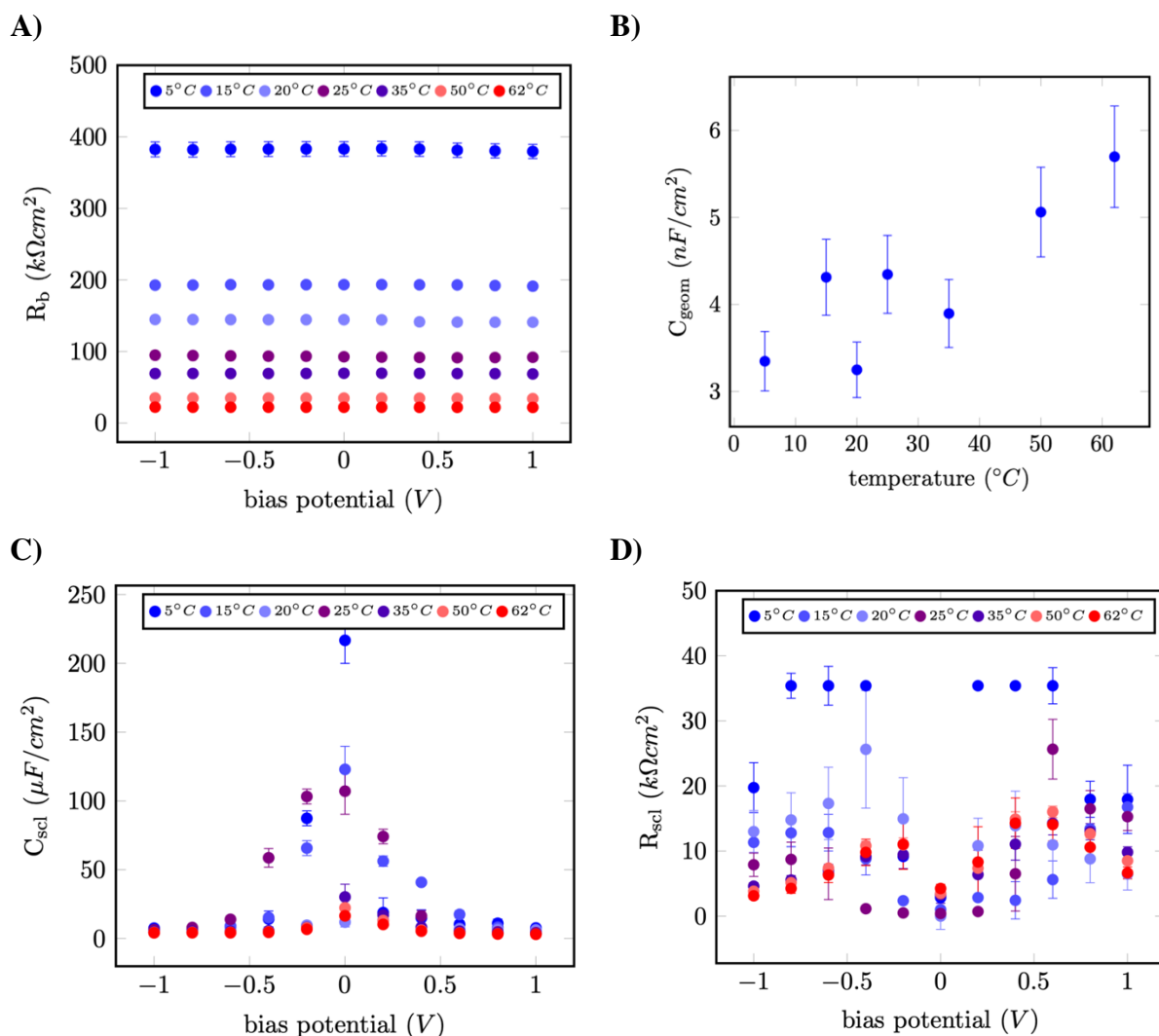


Figure 22. Parameters of the evaluation of impedance data with the EEC shown in **Figure 18**. The two bulk properties, R_{bulk} and C_{geom} in **A)** and **B)** show a potential independent behavior with an increase in bulk resistance with temperature as expected. The increase in geometric capacitance is due to an increase in permittivity. The space charge layer properties C_{scl} & R_{scl} qualitatively match the room temperature data shown before with decreases in both resistance and capacitances. However, the asymmetry of the resistances is more pronounced for higher temperatures. *Graphs adapted with permission from Ref 241. Copyright 2022 American Chemical Society.*

The bulk properties, shown in **Figure 22 A)&B)**, show the expected constant behavior across the whole range of applied bias potentials. While the effect of temperature on the bulk resistance can be described using the Arrhenius equation, the origin of the increasing geometric capacitance,

C_{geom} , is not described in the literature for SSEs. An early study in 1963 found that a temperature-correlated increase in dielectric constant is seen in cubic ionic compounds, identifying volume cell expansion as the most prominent factor.²⁴² Some literature^{243,244} exists on the high dielectric constant observed in Li^+ -conducting SSEs, but without further investigation of the temperature impact. While volume expansion is an accessible experimental parameter, a detailed investigation is out of the scope of this work, and although the thickness of the sample will certainly change to some degree, the change is not considered relevant for the calculations in this work. Whether an increase in temperature leads to a change in (mobile) ion or defect concentrations will be discussed later in section 6.4.

For the SCL parameters, shown in **Figure 22 C)&D)**, the qualitative behavior of the room temperature parameters of **Figure 20** can be confirmed. The resistance decreases as the temperature increases, which – from an electrochemical point of view – is expected. At low bias potentials, i.e., absolute values below 0.5 V, and the lower temperatures below 20 °C the layer might not be fully formed. The capacitance drops symmetrically upon applying a bias potential and decreases with the increase in temperature, indicating a growing depletion layer.

While a thorough study of the impact of temperature on SCL thickness would benefit from a method using a direct measurement, perhaps spectroscopic ellipsometry, the indirect determination using EIS allows for simultaneous determination of resistances and thereby the impact on the electrochemistry. Furthermore, the ellipsometry sample stage is not as easily manipulable, and temperature variation would require more work, which could be part of future studies. In the following discussion, only the values for negative bias potentials are used as the resistance values show a more reasonable trend.

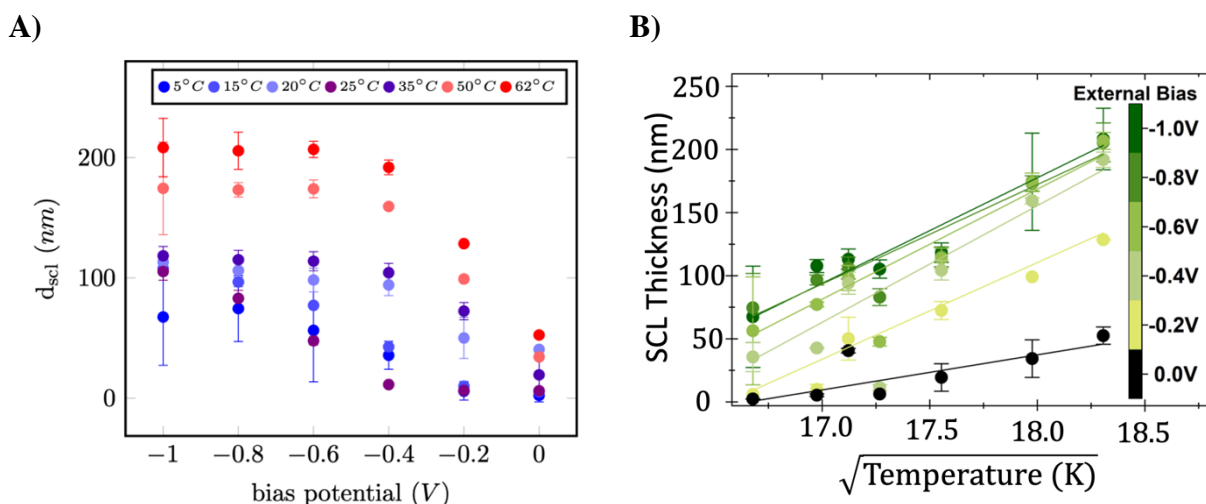


Figure 23. SCL thickness plotted over bias potential, **A**), and the square root of temperature calculated based on the measured capacitances and dielectric constants, **B**). A plateau formation can be observed for higher temperatures at higher absolute potentials. The proportionality suggested by the Debye theory between screening length and temperature is confirmed in **B**) for negative applied potentials. *Graph adapted with permission from Ref 241. Copyright 2022 American Chemical Society.*

Figure 23 shows SCL thickness for different temperatures and bias potentials calculated from the EIS analysis. The growth of the SCL is promoted by both the applied potential (as discussed in the previous section) and the temperature. To explain such a trend, it is helpful to reconsider the underlying boundary conditions of the electrochemical system. The number of depletable Li^+ per volume is given by the mobile Li^+ concentration. If the potential drop across the SCL is equal for all temperatures, a wider layer containing the same amount of charge indicates a lower concentration of depletable Li^+ . This is somewhat contradictory to the general assumption that an increase in temperature should activate more Li^+ to become mobile and take place in the conduction process, as observed for practically all SSEs. A solution for this conflict can be found in the impact of the dielectric properties on the SCL formation, which will be discussed in section 6.4 and is suggested by the multitude of theoretical models described in 2.4.

More importantly, the scaling of the thickness with the square root temperature proves that the concept of the Debye screening length can be transferred from liquid electrolytes to SSEs. While no exact linearity holds for all bias potentials, an increase in the slopes can be observed in **Figure 23B**). Even for no applied bias potential, the depletion layer grows as the temperature increases. This indicates that the electrochemical potential without an applied bias potential is not exactly

zero, which could be caused by the Au electrodes as reported in a study on Au(111).²⁴⁵ Early reports in the literature have considered the interfacial capacitance at a metal/SSE with much smaller Debye lengths on the order of the lattice parameters.²⁴⁶ In a review article spanning across different sorts of SSEs, it was reported that for yttrium-stabilized Zirconia compounds the Debye length largely underestimates the SCL thickness.²⁴⁷ Further studies, in combination with the exact determination of the thickness using spectroscopic ellipsometry, should also consider the dielectric constant as part of the Debye equation.

The thickness of SCLs is certainly relevant to physically describe the phenomenon and validate theoretical models for the SCL formation in SSEs, but the contribution to the interfacial resistance is of more practical importance. The overall decrease in resistance, shown in **Figure 22D**), can be expressed as an increasing conductivity when taking the thickness of the layers into account. **Figure 24A**) shows the Arrhenius behavior of the SCL conductivity for the three lowest bias potentials and thus for the largest SCL thicknesses. Overall, the conductivities increase with the temperature, where a linear trend can be observed for the different bias potentials. Viewing the SCL as a new electrolyte material with different ionic properties, i.e., ion and defect concentration and activation energy, the ion transport is still a hopping mechanism and, therefore, a temperature mediated effect.

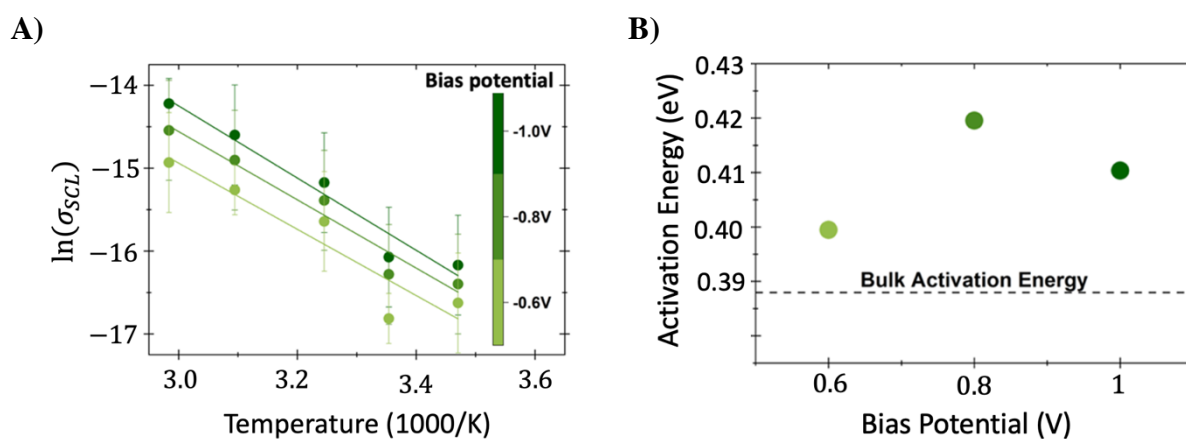


Figure 24. **A)** Arrhenius behavior of the conductivity observed in SCLs formed at the SSE/Au interface for three different bias potentials. The overall conductivity is lower at higher bias potentials. **B)** Activation energy calculated from the slope of the Arrhenius plot and a comparison to the bulk activation energy (dashed line). *Data adapted with permission from Ref 241. Copyright 2022 American Chemical Society.*

However, the activation energy rises significantly compared to the bulk activation energy of 0.388 eV as shown in **Figure 24B**). For yttria-stabilized zirconia, the opposite effect has been discussed in the literature.²⁴⁸ The depletion of ions leads to more vacancies, which in turn lowers the energy an ion must overcome to take part in the conduction process. Thus, the activation energy decreases as the ions are depleted.

In the Li⁺-conducting SSE of this study, a different mechanism seems to be dominant, which can be explained using an analogy to semiconductor physics. For semiconductors, it has been long known that Coulomb interaction leads to the trapping of electrons in highly depleted space charge regions and thereby hinders electronic conductivity.²⁴⁹ The phenomenon of Coulomb trapping has been investigated in polymer SSEs with the goal of minimizing trapping effects to foster high ionic conductivity.^{250,251} The SCL is a region of low cation concentration, thus only leaving a highly negatively charged anion lattice that traps any remaining cation. The exact physics of this trapping effect could be studied in the future using, for example, solid-state Nuclear Magnetic Resonance (NMR), which has been used to investigate trapping effects at interfaces towards battery electrodes.²⁵²

The temperature effect on SCL formation and conductivity has been studied empirically using EIS with the newly developed EEC. Although the results partially match theoretical expectations, such as scaling with the Debye length and qualitative Arrhenius behavior, the underlying mechanisms are to be investigated more thoroughly.

Based on the theoretical model introduced in section 2.4, the SCL formation as a function of temperature and bias potential can be depicted as follows: As shown in **Figure 25A**), when moving away from zero bias potential, the SCL starts to deplete and grows simultaneously into the electrolyte. Once a certain potential, here -0.6 V, is reached, the lattice is fully depleted, and any additional bias potential leads to a growth of the SCL perpendicular to the electrode. The temperature effect is similar, under the assumption that no additional Li⁺ are becoming mobile and the depletable number of Li⁺ is constant. The additional layer depleted of Li⁺ exhibits higher activation energy compared to the bulk and thereby contributes to the observed increase in charge transfer resistance across the interface, shown in **Figure 22B**).

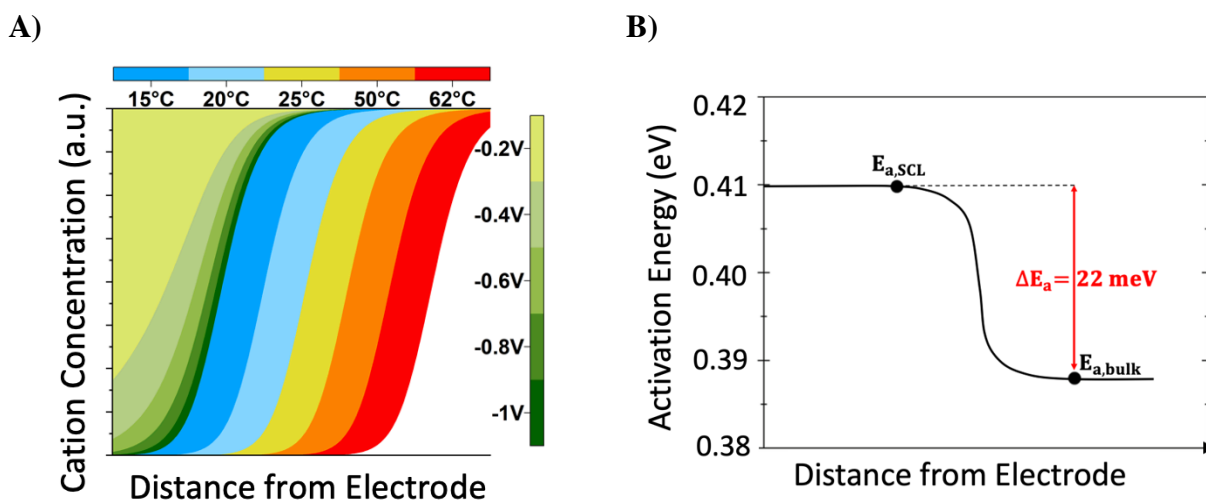


Figure 25. **A)** Formation of the SCL represented by the decrease in mobile cation concentration as a function of bias potential (green shades) and temperature (blue to red). **B)** The increased activation energy of the formed SCL compared to the bulk SSE of 22 meV. *Data adapted with permission from Ref 241. Copyright 2022 American Chemical Society.*

The change of the SCL's spatial extent correlates with the number of mobile Li^+ and the available vacancies. However, literature on quantification of these fundamental numbers is scarce, with one literature report of $4.7 \cdot 10^{27} \text{Li}^+ / \text{m}^3$ determined by solid-state NMR.²⁵³

The well-established Mott-Schottky theory for semiconductors, briefly described in section 2.5, uses the correlation of SCL capacitance to the applied bias potential to calculate charge carrier densities. The next section will show that a modified Mott-Schottky analysis can be formulated for SSEs. In combination with SPEIS measurements and the EEC for SCL formation in SSEs, this analysis can be used to calculate ionic concentrations.

6.4 Determining Ion Concentrations using a Modified Mott-Schottky Approach.

The work in the following section was conducted together with Matti Kaye, who's thesis was advised as a part of this work.²⁵⁴ The Mott-Schottky (MS) theory for semiconductors describes the SCL formation in the presence of an external potential and thereby links the formed capacitance with the applied bias potential. The classical approach for SCL formed by an accumulation or depletion of electrons can be found in section 2.5. A reformulation of the theory to be applicable for ionic SCLs and, therefore, ion concentrations can be done as follows.

Table 6 defines all relevant parameters and variables for the ionic Mott-Schottky theory (iMS). While the different concentrations were introduced before, for the built-in potential it is worth reconsidering the electrochemical equilibrium at the electrode/electrolyte interface. The driving force for the formation of SCLs is the electrochemical potential difference, which can be of electrical (e.g., a bias potential) or chemical nature. As the iMS theory describes the voltage-capacitance relation, the varied voltage is only the applied bias potential, and any preexisting potential drop across the interface changes the potential where the SCL becomes minimal, and the SCL capacitance is highest. The built-in potential is, therefore, specific for a given material system, and in symmetric blocking conditions, it is expected to be close to zero.

Table 6. Parameters and variables used in the derivation of iMS theory and a comparison to the traditional Mott-Schottky (MS) parameters used in semiconductor physics.

	Description	iMS vs. MS.
Constants		
F	Faraday constant	same
ϵ_0	vacuum dielectric constant	same
Material properties		
ϵ_R	relative dielectric constant	material dependent
z_i	charge of species i	ion/defect vs. e^- /hole
c_i	concentration of species i	ion/defect vs. e^- /hole
Variables		
A	sample area	same
T	Temperature	same
x	1D spatial coordinate	same
ϕ	bias potential	same
ϕ_{bi}	built-in potential	electrochemical vs. electrical

As in the derivation of the classical MS, we start with the 1D Poisson equation:

$$-\frac{\partial^2 \phi}{\partial x^2} = \frac{F}{\epsilon_0 \epsilon_R} \sum_i z_i c_i \quad \text{Equation 46}$$

As all mobile, charged species must be considered in the sum, the assumption of immobile anions, as introduced in section 2.1, leads to the conclusion that only vacancies and cations are mobile. A further restriction to the concentrations is the fact that if the cation concentration changes, the free vacancy concentration must change by the same amount but with a different sign. The two concentrations, c_{Li} and c_{vac} , for Li^+ and free vacancies can therefore be rephrased to c_{max} and c_{Li} , where $c_{max} = c_{Li} + c_{vac}$ is the maximum number of Li^+ accumulable with all vacancies filled. The mobility of cations and vacancies inside of an SSE can be described using the Poisson-Nernst-Planck (PNP) equation as described in section 2.2. However, it has been theorized in the literature that the PNP approach has significant shortcomings for highly concentrated electrolytes.²⁵⁵ Recently, a modified PNP model was introduced by Liu et al.,²⁵⁶ which considers the impact of

vacancies by adding an upper limit for the cation concentration (c_{max}). The spatial distribution of the cations, c_+ , for a given potential ϕ , is calculated to be:

$$c_+(x) = \frac{c_{Li^+} \exp\left(-\frac{z_{Li^+}F}{RT}\phi\right)}{1 + \frac{c_{Li^+}}{c_{max}}\left(\exp\left(-\frac{z_{Li^+}F}{RT}\phi\right) + 1\right)} \quad \text{Equation 47}$$

The Poisson equation and the derivation shown in section 2.5 can be used to calculate the capacitance, and thereby the following equation is found:

$$\frac{1}{C_{SCL}^2} = \frac{2}{A^2\epsilon_0\epsilon_R zF c_{Li^+}} \frac{\frac{RT}{zF} \frac{c_{max}}{c_{Li^+}} \ln\left(1 + \frac{c_{Li^+}}{c_{max}}\left(\exp\left(-\frac{zF}{RT}(\phi - \phi_{bi})\right) - 1\right)\right) + \phi - \phi_{bi}}{\left(1 - \frac{\exp\left(-\frac{zF}{RT}(\phi - \phi_{bi})\right)}{1 + \frac{c_{Li^+}}{c_{max}}\left(\exp\left(-\frac{zF}{RT}(\phi - \phi_{bi})\right) - 1\right)}\right)^2} \quad \text{Equation 48}$$

At first glance, Equation 48 does not look like the original Mott-Schottky equation. However, if the potential ϕ deviates from the built-in potential ϕ_{bi} the exponential terms quickly vanish. **Figure 26** shows that for potential values not in proximity of the built-in potential, the iMS equation is linear.

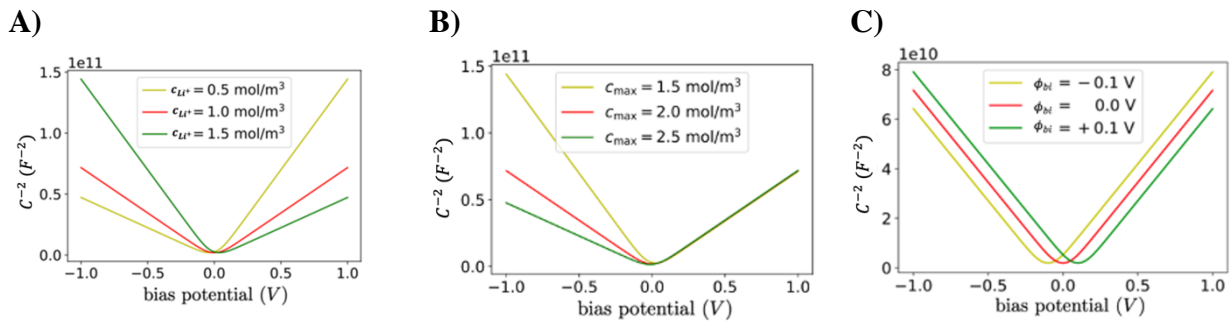


Figure 26. Numerical calculations of the iMS equation (Equation 48). Standard values are $c_{Li^+} = 1$ mol/m³, $c_{max} = 2$ mol/m³, $\phi_{bi} = 0$ V, and $T = 300$ K. Variation of c_{Li^+} and c_{max} leads to an asymmetric change in the slope, shown in **A)** and **B)**. The offset along the x-axis with the variation of V_{bi} can be observed in **C)**. *Graphs adapted/reproduced with permission from reference 254.*

It is important to notice that the potential values of the x-axes in **Figure 26A)** - **C)** imply the use of a reference electrode setup in which the accumulation layer and depletion layer can be measured separately. In this work, no reference electrode is employed, and only the depletion layer is

measured as described in the explanation of the EEC in section 6.2. The derivation of the Mott-Schottky analysis does not *a priori* define whether the SCL is positively or negatively charged, and therefore the capacitance-voltage relationship is valid for both negative and positive applied potentials.

Figure 26A) and **Figure 26B)** show the impact of the Li^+ concentration and the physical limit (i.e., c_{max}) on the inherent asymmetry. When a certain amount of charge is displaced, the width and capacitance of the accumulation and depletion layer are directly linked to the achievable concentration. A thinner layer with higher concentration difference can hold the same amount of charge as a wider layer of lower concentration change. In blocking conditions, the layers are only symmetric for $2c_{\text{Li}^+} = c_{max}$, and asymmetric behavior is expected for all other values. This is important for the experimental considerations: As explained in the derivation of the electrical equivalent circuit, see section 6.2, measuring the capacitance caused by the accumulation of charges is not achievable without a reference electrode as the depletion layer will dominate both resistive and capacitive effects. The fitting of the equation to the experimental data must therefore be limited to negative potentials and thereby only allows to calculate the Li^+ concentration but not the maximal concentration. When no reference electrode is used, and only the depleted layer is observed for both negative and positive bias potentials, the observed symmetry in voltage-capacitance plots can mislead to the conclusion that the bulk concentration is exactly half the maximal concentration. The built-in potential, a variation of which is shown in **Figure 26C)**, only impacts the position of the iMS curve along the x-axis. For a semiconductor junction the built-in potential is easily explained by the potential the junction exhibits due to the difference in doping, and therefore describes the space charge region without any electrical driving force.²⁵⁷ The electrochemical potential difference in the symmetrical cell setup of this work is not as simple. In principle, the Au electrode and the SSE have a different electrochemical potential, and thus the built-in potential leads to the formation of an SCL even at zero potential. However, the measurement of this potential would again rely on a reference electrode – and therefore is out of the scope of this work.

With these limitations, the experimentally obtained data of the SPEIS measurements can be fitted with the iMS equation, and information about the Li^+ concentration be obtained. A temperature variation is taken into consideration from the beginning to investigate the impact of temperature

on the charge carrier concentrations. For room temperature, the inverse squared capacitance is shown in **Figure 27A)** showing a slightly asymmetric trend for negative and positive potentials as expected from the considerations above. The minimum of the curve is slightly moved to positive potentials, indicating a potential of minimum SCL presence at small positive polarizations of the sample.

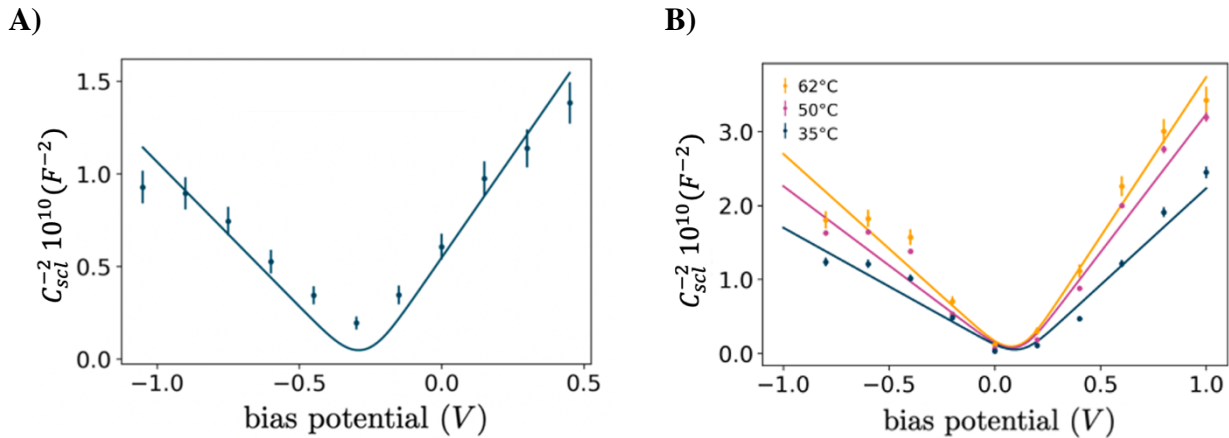


Figure 27. A) Room temperature SPEIS measurement in a Mott-Schottky plot with a slight asymmetry for negative and positive potentials. Overall, the fit of the iMS equation is closer to the data for positive potentials. **B)** Mott-Schottky plots of SPEIS data for different temperatures, solid lines are the fits of the iMS equation. While the SSE used for the measurements was the same, the samples were in a different electrochemical state, giving rise to the offset in the minimum of the curves, i.e., ϕ_{bi} . *Graphs reproduced with permission from reference 254.*

With increasing temperature, the asymmetry becomes more pronounced, as shown in **Figure 27B)** with an overall decrease in capacitances (thus increase in inverse squared capacitances). While the asymmetry points back to the issue of the missing reference electrode, the change in slope on the positive (right) side of the graphs leads to the conclusion that the concentration must change in dependence of the temperature. From the iMS equation and the calculations shown in **Figure 26A)** it can be deduced that the higher the slope, the lower the Li^+ concentration regardless of the maximal concentration, see **Figure 26B)**. Qualitatively, the decrease in Li^+ concentration agrees with the conclusions in section 6.3, where the thickness of the depletion layer grows with increasing temperature indicating that the same amount of charge is stored in a larger volume. Comparing the qualitative results to experimental studies in the literature remains difficult as the temperature dependency of the Li^+ concentration is a rarely studied phenomenon. However, early

theoretical works on single-crystal Na β -alumina suggest an exponential increase in concentration when the temperature is increased.²⁵⁸ Several approaches to explain the nonlinearity of traditional MS plots exist, such as the presence of multiple energy bands for mobile species in a TiO₂ semiconductor.²⁵⁹ Although this is certainly an interesting thought and would give insight into the solid-state ionics of the SSE at hand, this remains out of the scope of this work.

In addition to the qualitative analysis for the temperature impact, the data for positive branch of the curves can be fitted to obtain numbers for the mobile Li⁺ concentrations. It is noteworthy that the temperature, besides the direct impact on Li⁺, influences the iMS equation also directly through the parameter T and indirectly through the impact on the dielectric constant. While the direct impact is negligible, as it only changes the slope of the curve for $\phi \approx \phi_{bias}$, the influence through the change in ϵ_R can be accounted for using the true dielectric constant from the measurement of C_{geom} .

Table 7. Comparison of physical and electrochemical properties underlying the interfacial charge layers in different systems. *Adapted with permission from Ref 254.*

Temperature	25 °C	35 °C	50 °C	62 °C
Li ⁺ concentration [mol/m ³]	3.5 ± 0.24	2.61 ± 0.06	1.38 ± 0.01	1.06 ± 0.04

While the Li⁺ concentration is a critical parameter for parameterization, which will be extensively used in the next section, a comparison to literature values is difficult as reports are rare. However, the concentrations of Li⁺ match that measured on the surface of a LICGCTM sample by a spectroscopy approach.²⁶⁰ In the next section, a kinetic Monte-Carlo model and a parameterization based on the experimental results of this work will be used to show that a physical calculation with the correct parameterization without any *a priori* assumption about the formation of SCLs verifies many of the experimental findings, such as the asymmetry of accumulation and depletion layer. The spatial extent of the SCLs, given a realistic approximation of the mobile Li⁺ and defect densities, matches the experimentally observed thicknesses determined by spectroscopic ellipsometry, as discussed in section 6.1.

6.5 Parameterization and Validation of a Kinetic Monte-Carlo Model.

The work of the following section was conducted together with M. Gößwein at the chair of Prof. A. Gagliardi for “Simulation of Nanosystems for Energy Conversion” at TUM. Data and graphs were created in close collaboration with M. Gößwein.

The method of kinetic Monte-Carlo (kMC) simulation has been used extensively for SSEs in solid oxide fuel cells,^{261,262} but little research has been done on Li⁺-conducting SSEs.

Table 8. Input and output parameters of the kMC model. Note that, only the concentrations are hard to determine, while all other parameters are easily measured. The direct output parameters are spatial distributions of Li⁺ and potentials, from which the SCL thicknesses can be determined as described in the text. Bold are the standard values for the simulation if not specified otherwise.

	Description	Numerical Values
Input Parameters		
$c_{Li^+,bulk}$	bulk Li ⁺ concentration [ions/cm ⁻³]	{5 · 10 ¹⁷ , 3 · 10¹⁸ , 10 ¹⁹ }
$c_{Li^+,max}$	maximal Li ⁺ concentration [ions/cm ⁻³]	{1.25, 1.5 , 2} · c_{Li^+}
Δt	simulated time [s]	{2, 5 , 15}
L_s	sample length [μm]	{1, 1.5 , 3}
ϵ_R	dielectric constant	{100, 677 , 1400}
ϕ_{bias}	bias potential [V]	{0, 0.5, 1.5, 2.5 , 3.5, 4.5}
	Description	Type
Output		
$c_{Li^+}(z)$	spatial Li ⁺ distribution	vector
$\phi(z)$	spatial potential distribution	vector
d_{n-scl}	negative SCL thickness (Li ⁺ depletion)	scalar
d_{p-scl}	positive SCL thickness (Li ⁺ accumulation)	scalar

Table 8 summarizes the input and output parameters of the kMC model. The input parameters, except for the Li^+ concentration ($c_{\text{Li}^+, \text{bulk}}$) and its limit (c_{max}), are well known and/or easily measured. The concentrations, however, are less well known and rarely described in the literature. The three numerical values for $c_{\text{Li}^+, \text{bulk}}$ are orientated on the results of the iMS, see section 6.4 – for example, at 25 °C, a mobile Li^+ concentration of $2.1 \cdot 10^{18} \text{ cm}^{-3}$ is determined. The maximal concentrations are set in reference to the Li^+ concentration of the bulk SSE, with up to 2 vacancies per mobile Li^+ present. Before any kMC simulations are performed, it is known that this limits the charge accumulable, and based on the asymmetry of thicknesses known from the spectroscopic ellipsometry study, see section 6.1, the values are reasonably chosen. With all other parameters known, the kMC model is employed to simulate the 1D concentration profiles of the charge carrier concentration and thus the electrical potential profile across the simulated device, which in this case is an SSE in blocking conditions of $1.5 \mu\text{m}$ thickness with a dielectric constant of 677. The driving force for the Li^+ is the electrical potential difference, or potential ϕ_{bias} , which is incorporated as a boundary condition such that the potential at position $z = 0$ matches the applied bias potential ϕ_{bias} and at position $z = L_s$ matches 0 V .

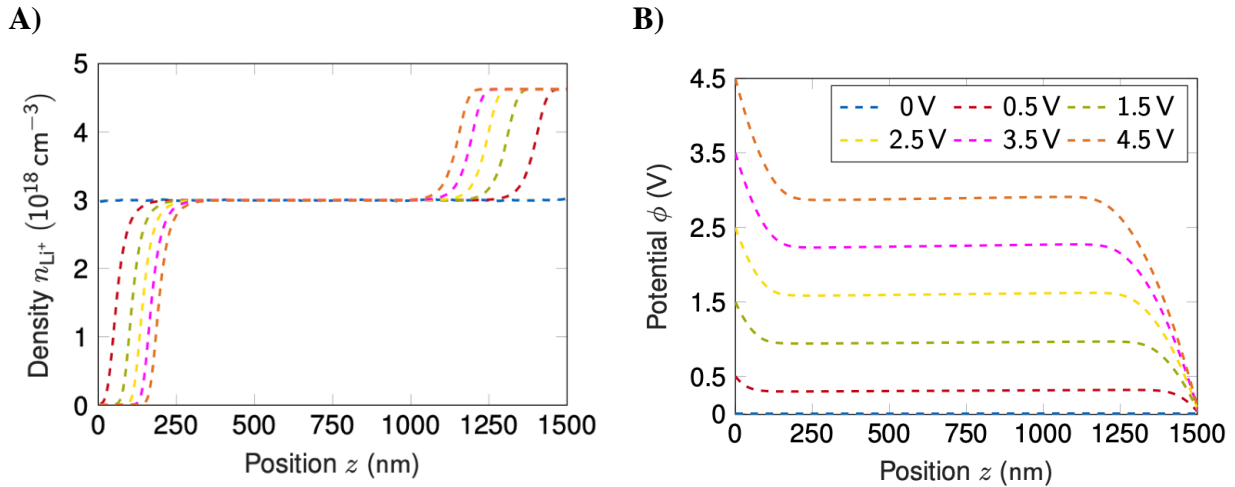


Figure 28. Results of kMC simulations with standard parameters, see **Table 8**. **A)** Li^+ concentration across the simulated device. A change in local charge concentration builds up towards the interface with a wider accumulation compared to the depletion. The net charge is displaced away from the more positive electrode to the negative electrode. The potential distributions in **B)** are based on the boundary conditions $\phi(z = 0) = \phi_{\text{bias}}, \phi(z = L_s) = 0$. The potential drops occur asymmetrically in the SCLs, with a higher potential drop in the accumulation layer. The bulk stays electroneutral, and therefore no potential drop occurs.

Figure 28 shows the results of the kMC simulation – the Li^+ concentration in **A**) and the potential profile in **B**). Here, the bulk concentration of mobile Li^+ , $c_{\text{Li}^+, \text{bulk}}$, is $3 \cdot 10^{18} \text{cm}^{-3}$ at which the local net charge is zero. Without any applied bias potential, i.e., $\phi_{\text{bias}} = 0 \text{ V}$, the charge profiles remain constant, and no SCL is present. Note that this neglects the possibility of a chemical potential difference between electrode and SSE, which could lead to a slight offset in the true potential at which no charge redistribution happens. The asymmetry of the charge profiles, with a wider, less concentrated accumulation layer and a thinner, more concentrated depletion layer is unsurprising as the boundaries for the charge carrier concentration are incorporated into the kMC model. An increase in bias potential leads to a widening of the SCL. However, as shown in **Figure 28A**), it is not proportional to the potential, which is in disagreement with the thermodynamic model described in section 2.4 and reference 77. These initial results predict the formation of two asymmetric SCLs of opposite charge based solely on merely two physical facts: The electrochemical potential difference must drop somewhere within the SSE, and there are limits for the minimal and maximal Li^+ concentration in the SSE. Even without an exact parameterization, the qualitative results align with the experimental studies of this work. The thicknesses of the SCLs can be quantified using the point of the Li^+ profiles where the concentration deviation is smaller than 10% with respect to the bulk Li^+ concentration, which is close to the abrupt approximation used for the iMS analysis of section 6.4.

Special attention must be brought to the impact of the SSE length, L_S . The thermodynamic model of Braun et al.⁷⁷ indicates a dependence of the SCL thickness on the “characteristic length” with a scaling of $d_{\text{scl}} \propto 1/L_S$. When the bulk is expected to be electroneutral, a dependence on the size of the bulk should not occur. **Figure 29** shows that the kMC model of this work does not predict a change of SCL thickness, **Figure 29A**) when the length of the simulation domain is changed. However, as observable in **Figure 29B**), a small deviation from the expected electroneutrality of the bulk occurs, which could either be due to the local polarizability of the SSE or a numerical artifact. As the impact is negligibly small, a detailed analysis is outside of the scope of this work.

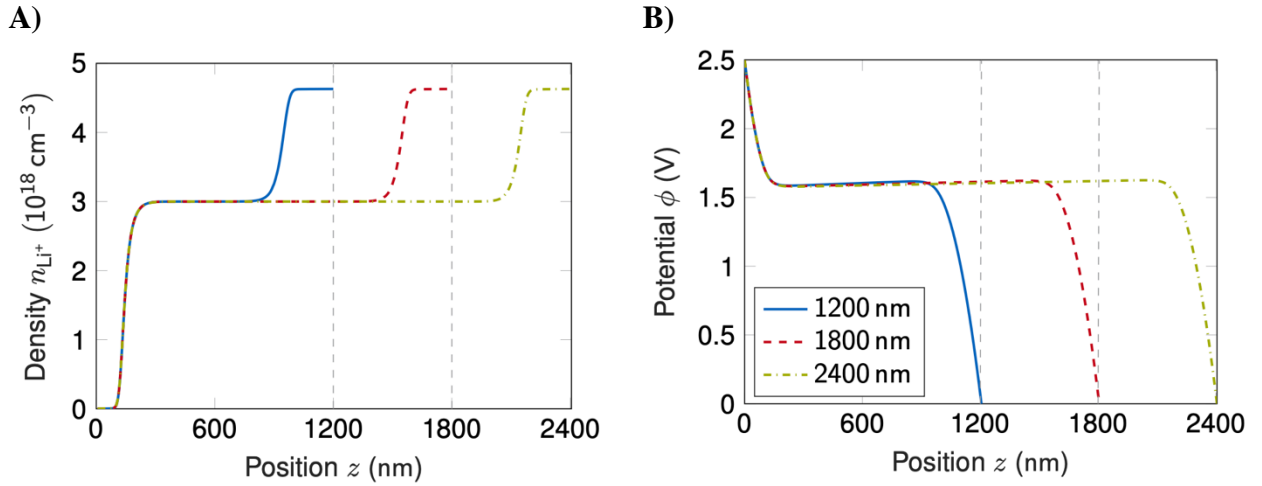


Figure 29. Impact of the sample length on the spatial extent of the SCLs. Simulation parameters are given in **Table 8**. In **A)** the independence of the SCLs thickness on the device length is shown with the dashed lines showing the geometrical end of the devices for different lengths. In the potential distributions, shown in **B)**, a slight deviation of the electroneutrality of the bulk is recognizable, which appears to be constant regardless of the SSE length.

After this brief physical validation of the model's output, the predictive power can be tested with a variation of the input parameters, namely $c_{Li^+,bulk}$, c_{max} , and ϵ_r . This is not only useful to test the model towards physical validity, but allows to predict the formation of SCLs for different materials with lower or higher Li^+ concentrations and provide a guide to quickly assess the susceptibility of a material to the formation of highly charged and possibly resistive layers at the interfaces towards electrodes. **Figure 30** summarizes the findings for the variety of parameters shown in **Table 8** for bias potentials between -4.5 V and 4.5 V for each simulation. Unsurprisingly, the SCL thicknesses strongly depend on the accumulable charge with higher cation concentrations $c_{Li^+,bulk}$ leading to thinner layers – as the total amount of charge to shield a certain potential at a fixed dielectric constant must be equal. The same is true for the influence of the maximal cation concentration, which impacts only the accumulation layer. The thicknesses of the SCLs are defined as the distance from the electrode at which the Li^+ concentration is within 10% of the bulk concentration.

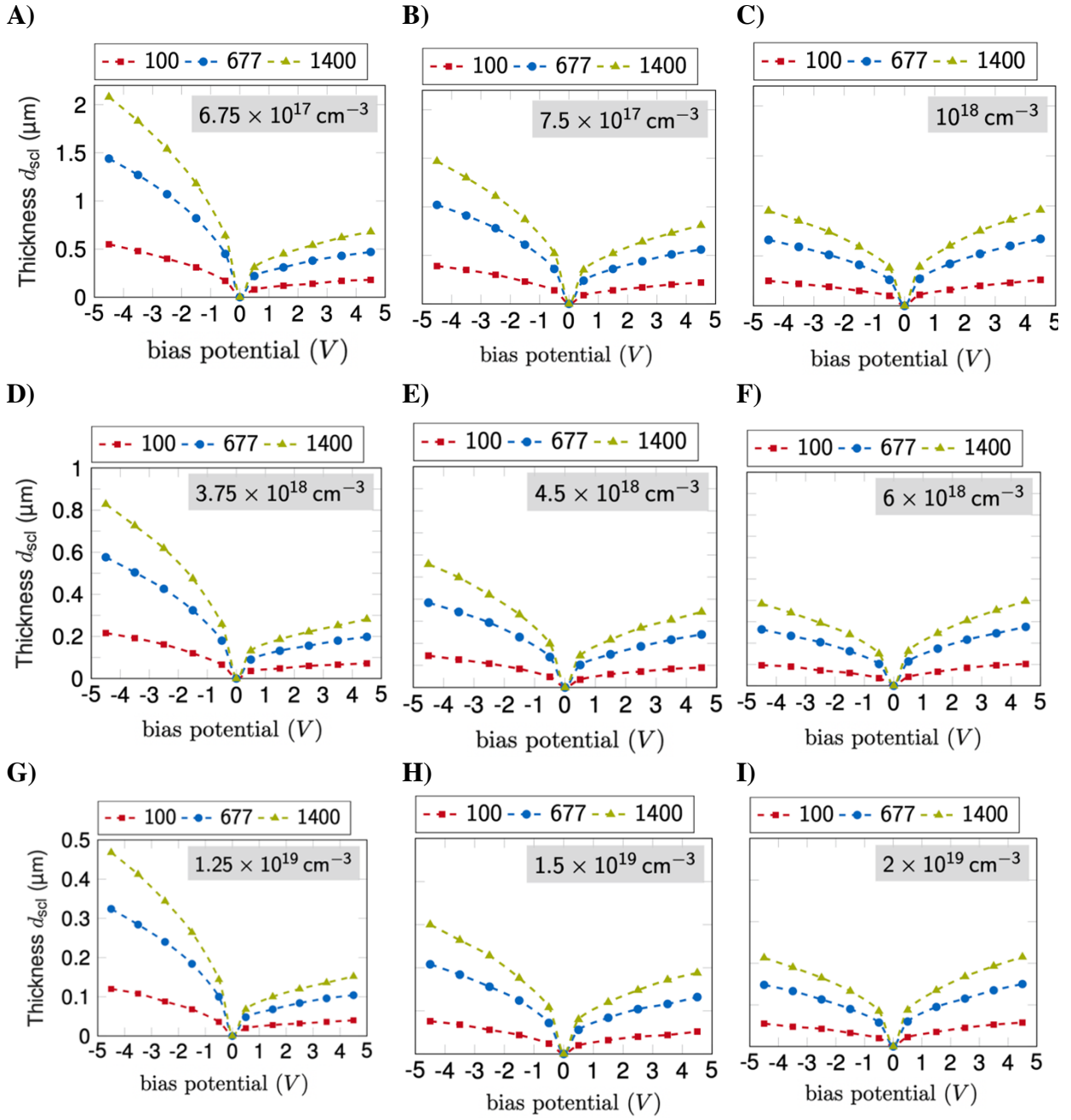


Figure 30. Influence of physical input parameters on the formation of SCLs. Standard parameters are given in **Table 8**. For positive bias potentials, the depletion layer thickness is shown, whereas, for negative potentials, the thicknesses are those of the accumulation layers. The thicknesses are calculated based on the 10% criterium as described in the text. The simulations in one row are of equal cation concentration ($c_{Li^+} = \{5 \cdot 10^{17}, 3 \cdot 10^{18}, 10^{19}\}$, for **A)-C)**, **D)-F)**, and **G)-I)**, respectively. The grey insets are the vacancy concentrations, which are 1.25, 1.5, and 2 times the cation concentration from left to right, respectively.

For a constant cation concentration, shown in the rows of **Figure 30**, only the layer for negative potentials, the case when the electrode next to the layer of interest is negatively biased, changes. Although the qualitative results seem unsurprising, the fact that the simulation quantitatively aligns with the measured thicknesses determined in the ellipsometry study, see section 6.1, and shows that the concentrations determined by the ionic Mott-Schottky analysis, see section 6.4, are close to the physical parameters. Not only does this further prove the conclusions about the formation of SCLs in the experimental studies, but it also allows to investigate the SCL formation in new materials.

7 Conclusion & Outlook.

In this thesis, the nature of space charge layers has been extensively elucidated and its physical and electrochemical properties measured. Theoretical predictions for the size and impact of the SCL were inconclusive or lacked a good set of parameters at the onset of this work, and experimental characterizations were and are hard to come by. A short summary of the research findings can be found at the end of this section. An overview of the leading Principal Investigators (PIs) in the field of SCL research in Li⁺-conducting SSEs is shown in **Figure 31**.

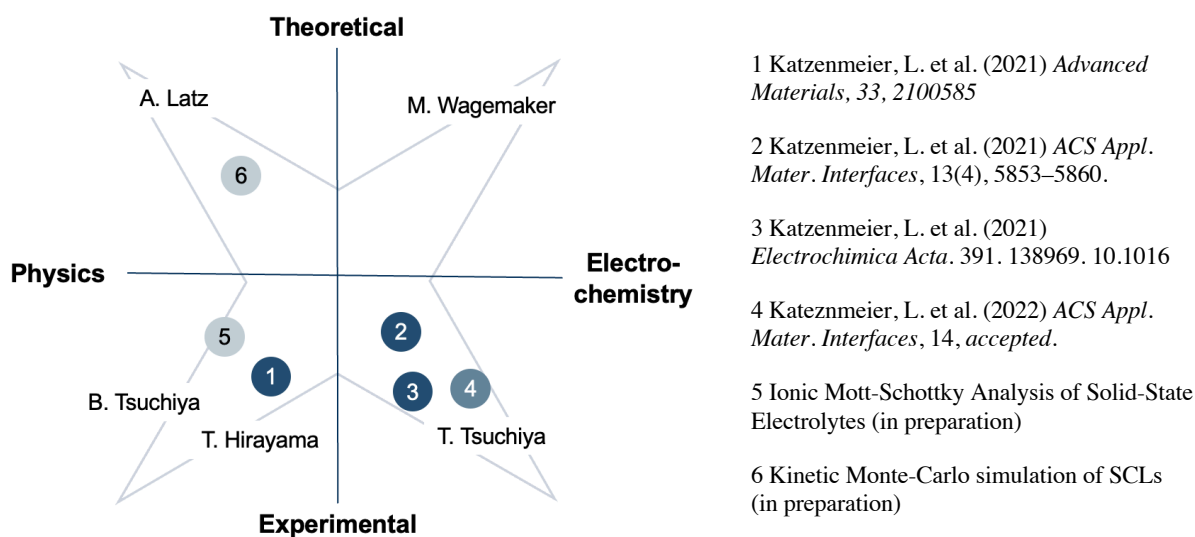


Figure 31. Overview of SCL research with the relatively small number of research groups, named by the PI, which investigate some aspects of SCL formation in SSEs ranging from theoretical to experimental works in the fields of physics and electrochemistry. The numbers indicate the studies and findings of this work according to the list on the right.

The findings of this work cannot only be seen from the viewpoint of SCLs, but each study in this work involved developing a new technique for modeling a new aspect of SSEs. Using spectroscopic ellipsometry to *in situ* detect charge accumulation in Li⁺ conducting ceramic materials did not only prove to be useful to detect the formation of SCLs in the SSE, but also opened a possible path towards the characterization of SSE layers and their Li⁺ concentration. Many publications on the formation of interphase layers at the SSE electrode exist, possibly

important for negative effects such as dendrite suppression,²⁶³ cell failure,²⁶⁴ or even stabilization of the interface.²⁶⁵ Spectroscopic ellipsometry could help to elucidate the nature of these layers with unknown precision while only requiring a bench-top setup. The technique is easily combined with electrochemical measurements as the sample is easily accessible and provides a way for *in situ* measurements.

The detection of SCLs via the capacitance caused by such a thin but resistive layer in SSEs showcases the power of EIS. Combined with an EEC, physical insights into the elusive SCLs can be gained with an easily accessible electrochemical technique that almost every research laboratory possesses. However, it must be stressed that the EEC is the central part of the analysis and therefore must be carefully validated and competing effects, here the grain-boundary impedance, have to be considered. Once a physically correct EEC is developed, the impedance spectra are easily recorded for different temperatures, electrode metals, and potentials, to only name a few possible parameters for which the influence on the electrochemical system can be studied. The fact that concepts and theories, such as the Debye screening and Mott-Schottky analysis, can be transferred to SSEs, although with minor adjustments, highlights the importance of fundamental research into the electrochemical behavior of Li⁺-conducting solids.

A deep understanding of the formation and impact of SCLs in SSE candidates for use in ASSB for automotive and mobile applications will require more work on both different materials and non-blocking conditions. Any real-world battery application will, of course, be in non-blocking conditions, such that the extension of the models and theories developed in this work must be prioritized in future studies.

However, the new field of lithionic devices, reviewed by J.L.M. Rupp and co-workers,²⁶⁶ could greatly benefit from a deep understanding of the formation of SCLs – as some of these devices operate in blocking conditions.

Research Summary

- An optical method, spectroscopic ellipsometry, was used to directly measure the growth of the SCL under different bias potentials and the asymmetry of depletion and accumulation layer shown. Not only the thicknesses but also the concentration changes inside these layers were quantified.
- Further probing of the electrochemical and physical properties of the SCLs was achieved by applying EIS and an EEC was developed. The physical EEC was then used to fit the data and was validated with a variation of bias potential, electrode metal, and temperature, thereby modifying the interface. The bulk and interface equivalent circuit elements were separated and individually assessed to gain insight into the SCL properties.
- The impact of temperature on the capacitance and resistance of the SCL was investigated using EIS. The SCL thickness shows a Debye-like temperature dependency, and its activation energy is significantly increased compared to the bulk electrolyte.
- A kinetic Monte Carlo model, parameterized through the experimental findings, conclusively reproduces the nature of the SCL formation in the model electrolytes. Not only do the calculated thicknesses match, but the model inherently predicts the experimentally observed responses.

8 Acknowledgements.

I express my sincere gratefulness to the following people without whom this work would not have been possible.

Prof. A. S. Bandarenka (TU Munich) for his supervision and providing critical feedback.

Prof. Dr. Ian Sharp (TU Munich) for agreeing to be the second supervisor for this work.

Dr. E. Knobbe (BMW Group, Munich) for the discussions on the intricacies of solid-state electrolytes and especially his mentoring in the non-academic aspects of this pursuit. **Dr. R. Koerver** (BMW Group, Munich) for always having a critical view of the data developed within this work.

Dr. A. Tschetschetkin and **F. Schatz** for their endless support and organizational efforts to make this work possible and for allowing me to contribute to the work of **TUMInt.Energy Research GmbH**. **V. Rechenberg**, **S. Scheele** (both TUMInt.Energy Research GmbH), **M. Ritter** (TU Munich), **H. Widera**, **U. Reitenbach** (both former ZAE Wuerzburg) for the administrative help with orders and travels. **Dr. D. Büttner**, **Dr. S. Braxmeier** and **Dr. H.P. Ebert** (all former ZAE Wuerzburg) for the support in the early days of this project.

Noteworthy are also my co-workers at **TUMInt.Energy Research GmbH** for the scientific discussions and their support. **Prof. J. L. M. Rupp** (TU Munich) deserves special thanks for the brief but impactful discussions on the reach and outlook of this work.

The ellipsometry measurements would not have been possible without the help of **S. J. Schaper** under the supervision of **Prof. P. Müller-Buschbaum** (TU Munich). For the kinetic Monte-Carlo simulations, I would like to thank **M. Gößwein** under the supervision of **Prof. A. Gagliardi** (TU Munich).

During this work, I got the chance to advise several masters and bachelors students to whom I am grateful for asking critical questions and helping me build a “solid” understanding: **R. Götz**, **A. Osmanpour**, **K. T. Song**, **J. Schönecker**, **S. Helmer**, **M. Wagner**, **M. Kaye**, and **M. Strahberger**.

The whole ECS group at TU Munich provided the academic surrounding to pursue my work, especially **P. Marzak, Dr. S. Watzele, Dr. B. Garlyyev, R. Kluge,** and **R. Haid** (thanks for the fun bike rides as well).


L. Carstensen for many interesting discussions and his effort in our joint works and presentations. **X. Lamprecht** had a great part in forming my skills on electrochemical impedance spectroscopy, culminating in a joint publication. Not to forget the great times we had together during off-campus activities, fueling my motivation to continue this work and face the challenges along the way.


9 Appendix.

9.1 Copyright Clearances.

Rightslink® by Copyright Clearance Center

21.10.21, 21:14

Home ? Help Live Chat Sign in Create Account



Properties of the Space Charge Layers Formed in Li-Ion Conducting Glass Ceramics
Author: Leon Katzenmeier, Simon Helmer, Stephan Braxmeier, et al
Publication: Applied Materials
Publisher: American Chemical Society
Date: Feb 1, 2021
Copyright © 2021, American Chemical Society

PERMISSION/LICENSE IS GRANTED FOR YOUR ORDER AT NO CHARGE

This type of permission/license, instead of the standard Terms and Conditions, is sent to you because no fee is being charged for your order. Please note the following:

- Permission is granted for your request in both print and electronic formats, and translations.
- If figures and/or tables were requested, they may be adapted or used in part.
- Please print this page for your records and send a copy of it to your publisher/graduate school.
- Appropriate credit for the requested material should be given as follows: "Reprinted (adapted) with permission from (COMPLETE REFERENCE CITATION). Copyright (YEAR) American Chemical Society." Insert appropriate information in place of the capitalized words.
- One-time permission is granted only for the use specified in your RightsLink request. No additional uses are granted (such as derivative works or other editions). For any uses, please submit a new request.

If credit is given to another source for the material you requested from RightsLink, permission must be obtained from that source.

[BACK](#) CLOSE WINDOW

© 2021 Copyright - All Rights Reserved | [Copyright Clearance Center, Inc.](#) | [Privacy statement](#) | [Terms and Conditions](#)
Comments? We would like to hear from you. E-mail us at customer@copyright.com

Li Conductivity of Space Charge Layers Formed at Electrified Interfaces Between a Model Solid-State Electrolyte and Blocking Au-Electrodes



Author: Leon Katzenmeier, Leif Carstensen, Aliaksandr S. Bandarenka

Publication: Applied Materials

Publisher: American Chemical Society

Date: Mar 1, 2022

Copyright © 2022, American Chemical Society

PERMISSION/LICENSE IS GRANTED FOR YOUR ORDER AT NO CHARGE

This type of permission/license, instead of the standard Terms and Conditions, is sent to you because no fee is being charged for your order. Please note the following:

- Permission is granted for your request in both print and electronic formats, and translations.
- If figures and/or tables were requested, they may be adapted or used in part.
- Please print this page for your records and send a copy of it to your publisher/graduate school.
- Appropriate credit for the requested material should be given as follows: "Reprinted (adapted) with permission from {COMPLETE REFERENCE CITATION}. Copyright {YEAR} American Chemical Society." Insert appropriate information in place of the capitalized words.
- One-time permission is granted only for the use specified in your RightsLink request. No additional uses are granted (such as derivative works or other editions). For any uses, please submit a new request.

If credit is given to another source for the material you requested from RightsLink, permission must be obtained from that source.

9.2 Temperature Dependency of the Double Layer Capacitance.

Electrochimica Acta 391 (2021) 138969



Contents lists available at ScienceDirect

Electrochimica Acta

journal homepage: www.elsevier.com/locate/electacta



Temperature dependences of the double layer capacitance of some solid/liquid and solid/solid electrified interfaces. An experimental study



Sebastian A. Watzel^{a,1}, Leon Katzenmeier^{a,b,1}, Jarek P. Sabawa^a, Batyr Garlyyev^{a,*}, Aliaksandr S. Bandarenka^{a,c,*}

^a Physics of Energy Conversion and Storage, Physik-Department, Technische Universität München, James-Frank-Str. 1, Garching bei München 85748, Germany

^b TUMint-Energy Research, Lichtenbergstr. 4, Garching bei München, Germany

^c Catalysis Research Center TUM, Ernst-Otto-Fischer-Straße 1, Garching bei München 85748, Germany

ARTICLE INFO

Article history:

Received 28 May 2021

Revised 2 July 2021

Accepted 18 July 2021

Available online 29 July 2021

Keywords:

Electrical double layer capacitance

Platinum

Fuel cells

All-solid-state battery

Solid-state electrolyte

Li-ion conductors

ABSTRACT

This study investigates the influence of the temperature on the electrical double layer capacitance (C_{DL}) of various materials, which are essential for fuel cells and solid-state Li-ion batteries. Electrochemical impedance spectroscopy is utilized to measure the C_{DL} of polycrystalline Pt/aqueous electrolytes interfaces, cathode catalyst layers of polymer electrolyte membrane fuel cells (PEMFC), and Au or Li electrodes in contact with a solid-state electrolyte (SSE), a prime example for solid-state ionics. Our results show that within the investigated temperature ranges, the C_{DL} decreases with an increase in the temperature for Pt electrodes in an aqueous acidic electrolyte. However, for SSE and PEMFC cathode catalyst layers, the C_{DL} increases with temperature. The C_{DL} behavior with the temperature of herein presented systems is important for understanding and modeling of the interface processes for renewable energy conversion systems such as fuel cells, water electrolyzers, and batteries.

© 2021 Elsevier Ltd. All rights reserved.

1. Introduction

Electrical double layer (EDL) structure plays a crucial role in various energy conversion and storage systems, such as supercapacitors, batteries, electrolyzers, and fuel cells [1–7]. The EDL structure can be influenced by several parameters such as the electrode and the electrolyte composition as well as temperature [8–13]. For instance, recently, the influence of supporting electrolyte components on the EDL of Pt, Au, and Cu electrodes has been investigated [14,15]. It was shown that the solvated metal cations present in the solution tend to accumulate near the electrode surfaces. This can have a significant influence on the catalytic performance of the electrodes [16–19]. Moreover, the EDL structure also plays an essential role in determining the properties of the solid electrode/solid-state electrolyte (SSE) interfaces. For instance, in solid-state ionics, the nature of the electrochemical interface

of SSE towards electrodes is believed to have a fundamental difference to the EDL formed at solid/liquid interfaces. The confinement of charge carriers to specific lattice sites of the SSE crystal gives a narrow concentration limit for the accumulation of charges. Previous work showed that the coexistence of a thin but highly charged, almost mono-ionic, EDL and a wider, less concentrated space charge layer (SCL) accurately describes the impedance behavior of an SSE in contact with a gold electrode [20]. The EDL of SSEs thickness is close to a few ionic radii of Li and, therefore, exhibits a capacitance on the order of microfarads. The electrochemical EDL in SSE has not been as widely investigated compared to the case of liquid electrolytes. A study on the metal/SSE has extended the classical Guoy-Chapman model to the case of solids and shows that the interfacial capacity differs quite drastically [21].

Electrochemical impedance spectroscopy (EIS) is a unique and affordable technique that can provide valuable information about the EDL of different interfaces [22,23]. In this work, the temperature dependence of the capacitive properties of various application-relevant systems is investigated using EIS. The influence of the temperature on the double layer capacitance (C_{DL}) of Pt/0.1 M HClO₄, cathode catalyst layer of polymer electrolyte membrane fuel cells (PEMFC), and SSE/Li or Au are presented. Results

* Corresponding authors at: Physics of Energy Conversion and Storage, Physik-Department, Technische Universität München, James-Frank-Str. 1, Garching bei München 85748, Germany.

E-mail addresses: batyrgarlyyev@tum.de (B. Garlyyev), bandarenka@ph.tum.de (A.S. Bandarenka).

¹ These authors contributed equally to this work.

showed that the C_{DL} of Pt electrodes decreases with increasing temperature, and the opposite trend is observed for the SSE and the PEMFC cathodes. The possible origin of these kinds of trends is briefly discussed.

2. Experimental methods

2.1. EIS measurements for polycrystalline Pt electrodes

Prior to experiments, all glassware was cleaned with freshly prepared, hot peroxymonosulfuric acid and subsequently rinsed multiple times with boiling de-ionized water. For the assessment of the C_{DL} of the simple Pt surface, a standard double-walled glass cell with a three-electrode configuration was utilized. A Pt wire (99.99%, Mateck, Germany), a mercury/mercury-sulfate electrode (SI Analytics, Germany), and a polycrystalline Pt(pc) (Mateck, Germany) were utilized as the counter, reference, and working electrode, respectively. The 0.1 M HClO₄ electrolyte was prepared using perchloric acid (70% Suprapur, Sigma Aldrich, Germany) and de-ionized water (18.2 M Ω) obtained from a water machine (Evoqua water technologies, Germany) and purged with argon (5.0) for at least 20 min. The temperature was controlled by a thermostat (Jubabo, Germany). The experiments were performed using a VSP-300 potentiostat (Biologic, France), and all the potentials are referred to the reversible hydrogen electrode (RHE) scale. A temperature range between 20 and 60 °C was studied. EIS spectra were recorded in 20 mV steps between 0.36 and 0.7 V vs RHE. Frequencies between 12 kHz and 1 Hz were applied, using a probing voltage amplitude of 10 mV.

2.2. EIS measurements related to the PEM fuel cell cathodes

For PEMFC cathode studies, a FuelCon Evaluator C1000-LT with an EIS capable load and the Peltier-Element-Tempered (PET) PEM single-cell was used [24]. The test procedure was fully automated and performed three times for each temperature measurement point. After preconditioning, to maintain the same measurement parameters and approximate the respective temperature, the impedance measurement was performed at the open-circuit potential. A membrane electrode assembly (MEA) with an active area of 43.6 cm² and a ~15 μ m thick polymer electrolyte membrane was used for the measurements. The Pt loading of the anode/cathode side was 0.05 and 0.45 mg Pt/cm², respectively. More about the measurement setup and the exact test procedure can be found in Ref. [25]. A temperature range between -5 and 60 °C was studied. EIS spectra were recorded at open circuit potential. Frequencies between 30 and 0.1 Hz were applied, using a probing current amplitude of 20 mA.

2.3. EIS measurements related to the metal/solid electrolyte interface

2.3.1. Solid Electrolyte

The solid electrolyte used in this work was a lithium-ion conductive glass ceramics (LICGCTM) purchased from Ohara, Germany. The main conductive in such samples crystalline phase is Li_{1+x+y}Al_xTi_{2-x}Si_yP_{3-y}O₁₂ and conductivity values of ~0.1 mS/cm are typical. The samples were used as delivered without further treatment.

2.3.2. Preparation of the blocking electrode

Gold electrodes were deposited using an e-beam evaporator (L560, Leybold, Germany) under vacuum conditions. A deposition rate of 1 Å/s was controlled with an IC-6000 (Inficon, Switzerland). Stainless steel masks with a radius of 7.5 mm were utilized to create circular electrodes.

2.3.3. Preparation of non-blocking electrodes

The Li electrodes used in this work were circular plates of 15.6 mm radius and 1 mm thickness. All handling was done in an Ar-filled glovebox with O₂ and H₂O residual values below 1 ppm. The surface was polished to reveal the metallic Lithium shine and instantly placed onto the SSE.

A temperature range between 25 and 62 °C was studied. EIS spectra were recorded in 0.25 V steps between -1 and 1 V bias potential. Frequencies between 5 MHz and 1 Hz were applied, using a probing current amplitude of 10 mA.

3. Results and discussion

3.1. Polycrystalline Pt and PEM fuel cells

First, the temperature effects on the EDL of Pt(pc) electrode were investigated in aqueous perchloric acid electrolytes. These model systems serve for a basic understanding and as a point of comparison with respect to more complex systems. To evaluate the C_{DL} the EIS is utilized. Using equivalent electric circuit (EEC) models with a physical meaning to fit the impedance data, the actual C_{DL} can be separated from other pseudo-capacitance contributions, e.g., caused by proton adsorption/desorption. The specific EECs are discussed for each individual system.

Fig. 1A shows a typical cyclic voltammogram, CV, of the Pt(pc) electrode in Ar-saturated 0.1 M HClO₄ at 50 mV/s scan rate. This CV shows all the expected features, such as typical proton and *OH/*O adsorption/desorption peaks, the peak positions are indicated in the figure [26,27]. Moreover, the Pt(pc) surface remained unchanged during the EIS measurements, which was confirmed by the CVs taken before and after recording the impedance spectra.

The EEC used to evaluate the EIS data is given in Fig. 1B. It consists of an uncompensated resistance, R_u , which is mainly determined by the electrolyte, the cell, and the electrode geometry, the impedance of the double layer Z_{dl} , as well as an adsorption capacitance, C_a and resistance, R_a . The latter two are caused by reversible adsorption/desorption with simultaneous electron exchange, e.g., the adsorption of protons or hydroxyl-ions. This pseudo-capacitance (C_a) can be typically separated from the C_{DL} due to the different time constant and frequency dispersion relation [28,29]. This physical model is generally accepted and commonly used for adsorption processes without diffusion limitation [14,15,22].

In general, the double layer capacitance depends not only on factors such as the electrolyte composition, the surface, and the temperature but also on the electrode potential. Consequently, EIS spectra were recorded and evaluated over a wide potential window to compare the minimum C_{DL} values at different temperatures. Fig. 2(A,B) show a typical impedance spectrum (open symbols) with the fitting results recorded at 20 °C. All the fits have a very small average deviation from the data of ($\Delta F^2 < 6 \cdot 10^{-5}$). Furthermore, all parameters have only low uncertainties (<5%), which shows the importance of the individual elements in the EEC. The fits at the respective capacitance minima for the higher temperatures can be found in the supporting information, SI (Fig. S1).

The exponent n in the constant phase element $Z_{CPE} = C_{DL} \cdot (j\omega)^{-n}$ remained always higher than 0.95. Hence, it can be assumed that the values of the parameter C_{DL} are close to the value of the real electrical double layer capacitance, C_{DL} .

In Fig. 2C, the C_{DL} values at different temperatures obtained from the EIS data analysis are plotted against the applied electrode potential. Two general trends can be seen. (i) Independent of temperature, the double layer capacitances are at minima at ca. 0.4–0.5 V vs RHE. (ii) The capacitance decreases with increased temperature. The position of the minima coincides with that from other works, e.g., for Pt (111) [30].

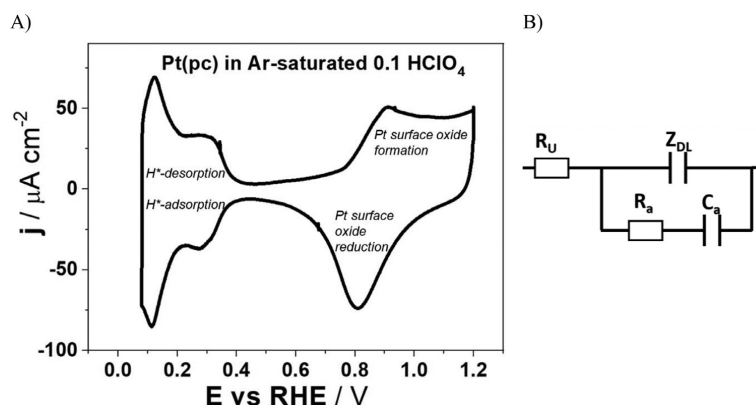


Fig. 1. Characterization of the Pt(pc) electrode. (A) Cyclic voltammogram in Ar-saturated 0.1 M HClO₄ (scan rate 50 mV s⁻¹). Typical proton and ⁻OH/⁻O adsorption/desorption peak positions are indicated in the figure. (B) Equivalent electric circuit for the evaluation of EIS data. It consists of uncompensated resistance R_U, a constant phase element to model the impedance of the double layer, Z_{DL}, adsorption resistance, R_a, and capacitance, C_a.

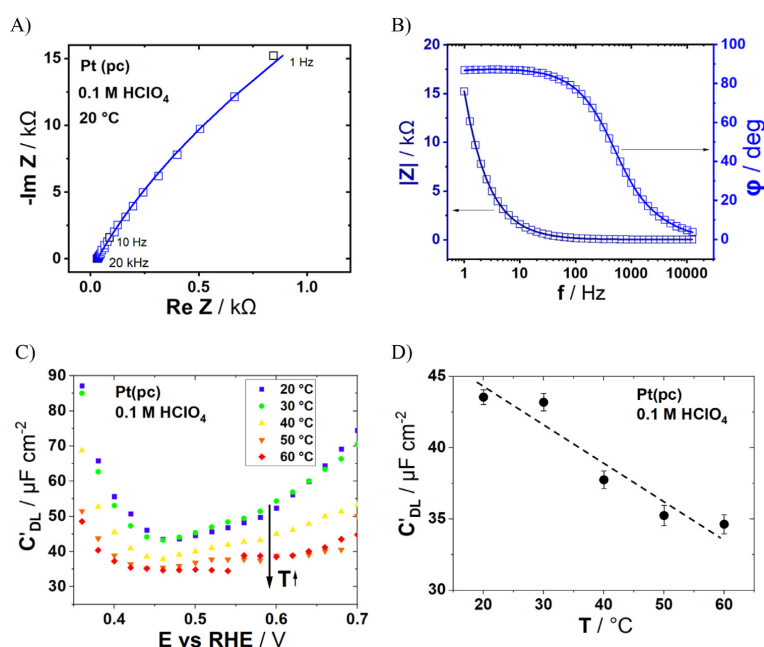


Fig. 2. Influence of temperature on the double layer capacitance of Pt(pc). (A) Representative Nyquist plot for the Pt(pc) electrode recorded in Ar-saturated 0.1 M HClO₄ at 20 °C and at 0.48 V vs RHE. Data points are represented with open symbols. The EIS data were fitted using the EEC presented in Fig. 1B. (B) Corresponding Bode plot. (C) The double layer capacitance as a function of the applied potential. (D) Minima of the double layer capacitance as a function of temperature. The dotted line is a guide to the eye. Note that, for better visibility of data points at high frequencies, the Nyquist plots are not orthonormal.

Concerning the temperature dependence of the double layer capacitance, as shown in Fig. 2C,D, this can probably be explained via Brownian molecular motion, stretching, bending, and rotation modes which are excited at elevated temperature [31]. Here, for example, the polarizability of water and thus the dielectric constant ϵ_r is significantly reduced at elevated temperatures. While at the lower temperature, the water molecules are more ordered and can be polarized, their polarizability is limited at higher tempera-

tures. This behavior leads to decreased ϵ_r [32]. In turn, this results in lower C_{DL}.

Let us now consider the C_{DL} of more complex systems, in particular, that of PEM fuel cells. To evaluate the impedance data with respect to the C_{DL}, an EEC shown in the inset of Fig. 3A was used. This EEC consists of an uncompensated resistance, double layer capacitance, adsorption capacitance and resistance. Moreover, due to the oxygen reduction reaction, ORR, happening at the cathode, the

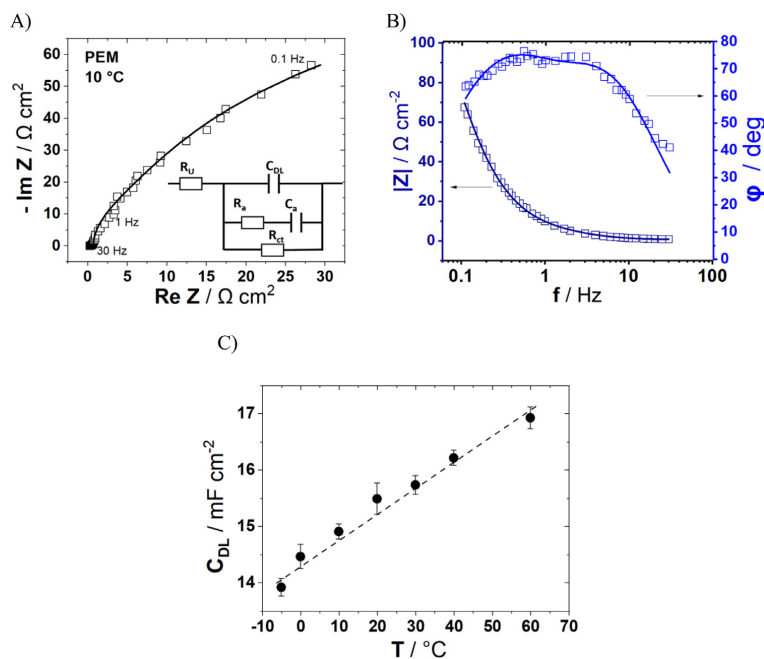


Fig. 3. Determination of the double layer capacitance of the PEM fuel cell cathode at various temperatures. (A) Typical Nyquist plot recorded at the 10 °C at the open-circuit potential. Open symbols correspond to measured data, while the line corresponds to the fitting using the EEC shown in the inset. The EEC consists of an uncompensated resistance, a double layer capacitance and adsorption capacitance and resistance, and a charge transfer resistance. (B) Typical Bode plot recorded at the 10 °C at the open-circuit potential. The magnitude of the impedance $|Z|$ (dark blue) and phase angle φ (light blue) are plotted versus the frequency. (C) The double layer capacitance as a function of temperature. The dotted line is a guide to the eye. Note that, for better visibility of data points at high frequencies, the Nyquist plots are not orthonormal (For interpretation of the references to color in this figure legend, the reader is referred to the web version of this article.).

EEC has an additional charge transfer resistance. This charge transfer resistance models the Faradaic reaction, while the adsorption capacitance and resistance are caused mainly by the adsorption of sulfonated groups from the ionomer [33,34].

Fig. 3A shows exemplary data of the measured impedance and the corresponding fitting analysis at a cell temperature of 10 °C. Fig. 3B illustrates the typical Bode plot recorded at the 10 °C at the open-circuit potential. The C_{DL} shows a quasi-linear behavior versus the cell temperature (see Fig. 3C). The detailed analysis of the other EEC parameters is out of the scope of this study and can be found in reference [25].

Two main mechanisms could be responsible for the quasi-linear increase of the measured C_{DL} in PEMFC: First, the proportion of free ions decreases sharply at low temperatures, which leads to a decrease in capacitance. Second, the influence of the volume changes of the catalyst layer triggered by the different temperatures cannot be neglected. There is higher repulsion energy between the hydrophobic and hydrophilic portions of the matrix domains at low temperatures, and thus less water can be absorbed at the hydrophilic sulfonate groups. In turn, at higher temperatures, more hydrophilic groups disperse into the hydrophobic matrix (entropically driven), leading to an increase in the number of water molecules absorbed at the hydrophilic groups [35–37]. In simple terms, this means that the reduction in volume towards lower temperatures results in a smaller amount of sulfonate groups coming into contact with the electrically conductive carbon surface, leading to a reduction in the interface and thus the capacitance.

Another practical conclusion of the double layer capacitance measurements related to the Pt-containing systems is that it is

not always correct to extrapolate the conclusions obtained using model Pt-surfaces to real PEMFC catalyst layers. Further investigations are required to understand the temperature dependencies of both model electrodes and devices in more detail.

3.2. Solid-state systems involving Li-ion conductors

Finally, the temperature dependence of C_{DL} formed between the solid-state battery electrolytes and Au or Li electrodes is examined. For this, the impedance was recorded for temperatures between 25 and 62 °C for both a blocking and a non-blocking electrode configuration. The blocking configuration has the SSE sandwiched between two gold electrodes, while the non-blocking one uses two Li electrodes.

It should be noted that, when considering the EDL in the case of SSEs, there are two significant differences to the solid/liquid interface. On the one hand, the charge carrier concentration tends to be higher in solids [38], more comparable to the ion concentration in ionic liquids. On the other hand, the crystal lattice poses an upper limit for charge carrier concentration. [39] As both of these are concentrations, ions, and vacancies, the impact of temperature can be considered as follows: As the temperature increases, the ions become more mobile and move through the lattice more easily. The concentration of mobile ions is also thought to depend on temperature, whereas the vacancy density is independent of the temperature.

For the analysis of the impedance data, it is essential to consider the different contributions to the impedance spectra of (i) bulk electrolyte, (ii) space charge layer, SCL, describing the wider

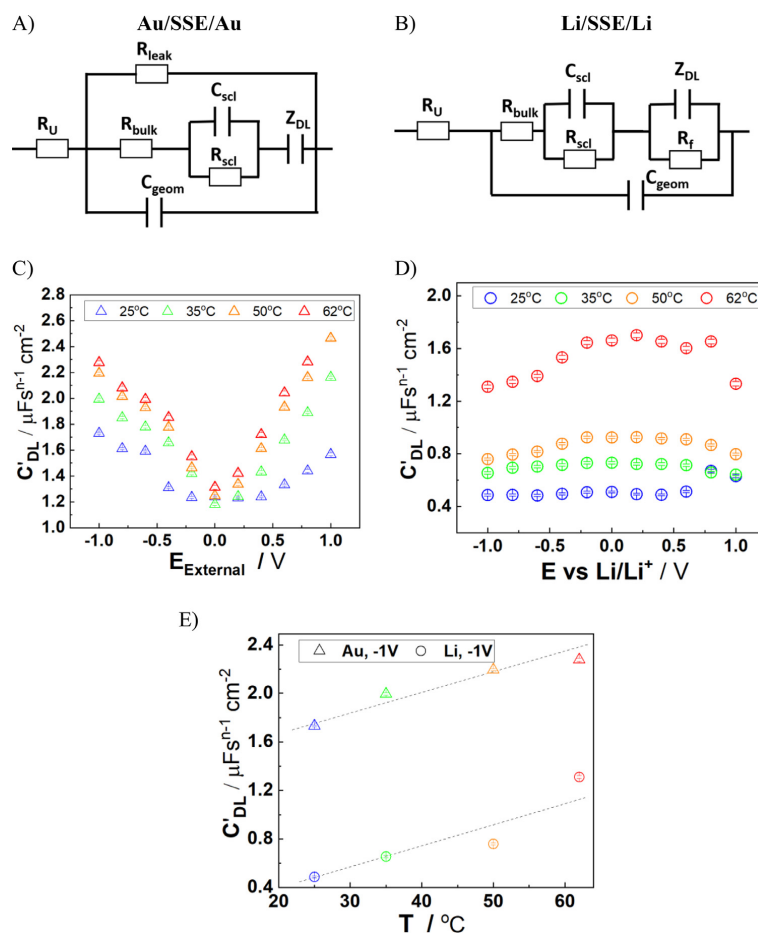


Fig. 4. Solid electrode/solid electrolyte interface EDL characterization. (A) and (B) show the EECs for the whole spectrum fit for the Au/SSE and Li/SSE, respectively. (C) The constant phase element value related to the double layer capacitance for the Au/SSE interface plotted over the applied external bias. Overall, the C'_{DL} values increase with increasing temperature. (D) The corresponding C'_{DL} values for the Li/SSE interface. While the applied potential only impacts the C'_{DL} moderately, the values increase drastically at higher temperatures. (E) Comparison of the C'_{DL} values for blocking and non-blocking electrode configurations at -1.0 V cell potential over temperature, dashed lines are guide to the eyes only.

depletion layer near the electrically positive biased side, and (iii) the double layer capacitance. In parallel, there is either a minor leakage or charge-transfer resistance for blocking and non-blocking conditions, respectively. The EECs for both cases are shown in **Figure 4A** and **B** for Au and Li electrodes, respectively. They only differ in the leakage and the charge-transfer resistance elements. The equivalent circuits represent the aforementioned contributions (i) – (iii), with (i) R_{bulk} and C_{geom} representing the bulk contributions, (ii) R_{scl} and C_{scl} – the space charge layer contribution [20,2], and (iii) the double layer constant phase element, Z_{DL} . The resistances, R_{leak} and R_f , are the electronic leakage under blocking conditions and the Faradaic resistance under non-blocking conditions, respectively. The values for the non-ideal double layer capacitance C'_{DL} (derived from the constant phase element) ranges from 0.2 to $2.8 \mu Fs^{-1} cm^{-2}$. Based on $C'_{DL} = \frac{\epsilon A}{d}$, where ϵ is the dielectric

constant, A is the contact area and d the electrolyte thickness, the thickness can be roughly estimated to range from sub-nm to a few nm.

Comparing the case of blocking (**Fig. 4C**) vs. non-blocking electrodes (see **Fig. 4D**), the overall capacitance for the non-blocking case is lower, which indicates either a wider layer or worse contact between two solids. If one assumes an equally good contact for the cases of Au and Li, this can be explained in light of the fact that constant flux of Li-ions will smear the double layer structure by inherently increasing the disorder near the interface. This effect is even more prominent for non-zero potentials where slightly lower C'_{DL} values are observed. Of course, an additional contribution could come from the imperfect interface between metallic Li and the SSE, which has been previously reported [40]. However, the potential change in the symmetric setup between two Li metal

electrodes leads to only a minor change in the C_{DL} , which induces a plating/stripping reaction (as shown in a similar material system in reference [41]).

Rather similar behavior of the C_{DL} with temperature is observed for both blocking and non-blocking conditions, as shown in Fig. 4E. With an increase of temperature from 25 to 62 °C, the double layer capacitance increases by a three-fold in the case of Li electrodes. Assuming a constant dielectric constant within the vicinity of the interface, this can be explained that the effective double layer thickness decreases by nearly a factor of three within this temperature range.

For non-zero applied biases, the constant oxidation and reduction of Li-ions at the electrodes lead to a slight decrease in the double layer capacitance, as seen in Fig. 4D. On the other hand, a higher temperature leads to higher ion mobility and increased number of ions taking part in the conduction process. However, the increase in the capacitance (Fig. 4E) indicates a higher charge carrier density at the interface. Therefore, the dominant factor must lie in the nature of the single-ion layer, as a higher temperature allows for more ions to accumulate within a single layer at the electrode surface.

As a potential in the blocking electrode case increases to +1 V, the C_{DL} almost doubles. This possibly indicates that the higher potential difference between the metal electrode and SSE leads to the Li-ions being drawn closer to the interface and therefore building a more compact layer.

4. Conclusion

In this study, the influence of the temperature on the double layer capacitance of various systems, namely, polycrystalline Pt electrode in acidic solution, PEMFC cathode, and SSE in contact with Au and Li electrodes, are presented. The C_{DL} decreased with an increase in the solution temperature for solid Pt electrodes in contact with aqueous $HClO_4$ solutions. We suggest that this is mainly due to the decrease in the dielectric constant, ϵ_r , at elevated temperatures, which leads to such an effect. In contrast, the double layer capacitances of the PEMFC cathode and the SSE increased with an increase in temperature. In the PEMFC cathode catalyst layers, the capacitance increase can be due to a lower proportion of free ions at lower temperatures. In addition, the temperature-dependent volume changes at the catalyst layer cannot be neglected. In the case of SSE, the increase in the C_{DL} can be attributed to the higher mobility and polarizability of the mobile ions.

Declaration of Competing Interest

The authors declare no competing interests.

Credit authorship contribution statement

Sebastian A. Watzele: Data curation, Investigation, Writing – original draft, Writing – review & editing. **Leon Katzenmeier:** Data curation, Investigation, Writing – review & editing. **Jarek P. Sabawa:** Investigation, Writing – original draft, Writing – review & editing. **Batyr Garlyyev:** Conceptualization, Investigation, Writing – original draft, Writing – review & editing. **Aliaksandr S. Bandarenka:** Writing – original draft, Writing – review & editing.

Acknowledgments

We are grateful for the financial support from Deutsche Forschungsgemeinschaft under Germany's excellence strategy – EXC 2089/1 – 390776260, Germany's excellence cluster "e-conversion", DFG project BA 5795/5-1 and BA 5795/6-1. This work is part of the

ASSB Bayern project funded by the Bavarian Ministry of Economic Affairs, Regional Development and Energy.

Supplementary materials

Supplementary material associated with this article can be found, in the online version, at [doi:10.1016/j.electacta.2021.138969](https://doi.org/10.1016/j.electacta.2021.138969).

References

- [1] S. Trasatti, Structure of the metal/electrolyte solution interface: new data for theory, *Electrochim. Acta* 36 (1991) 1659–1667.
- [2] S. Trasatti, L.M. Doubova, Crystal-face specificity of electrical double-layer parameters at metal/solution interfaces, *J. Chem. Soc. Faraday Trans. 91* (1995) 3311–3325.
- [3] L.M. Doubova, A. Hamelin, L. Stoicoviciu, S. Trasatti, Temperature dependence of double-layer parameters of the silver (100) face: comparison with other silver faces, *J. Electroanal. Chem.* 325 (1992) 197–205.
- [4] A. Hamelin, L. Doubova, L. Stoicoviciu, S. Trasatti, The temperature dependence of the double layer parameters of the (111) face of silver, *J. Electroanal. Chem. Interfacial Electrochem.* 244 (1988) 133–145.
- [5] Y. Dong, S. Zhang, X. Du, S. Hong, S. Zhao, Y. Chen, X. Chen, H. Song, Boosting the electrical double-layer capacitance of graphene by self-doped defects through ball-milling, *Adv. Funct. Mater.* 29 (2019) 1901127.
- [6] E. Lust, In electrical double layers. Double layers at single-crystal and polycrystalline electrodes, in: A.J. Bard (Ed.), *Encyclopedia of Electrochemistry*, Wiley-VCH, 2007 (Ed.).
- [7] H. Yang, X. Zhang, J. Yang, Z. Bo, M. Hu, J. Yan, K. Cen, Molecular origin of electric double-layer capacitance at multilayer graphene edges, *J. Phys. Chem. Lett.* 8 (2017) 153–160.
- [8] Z.A. Goodwin, A.A. Kornyshev, Underscreening, overscreening and double-layer capacitance, *Electrochem. Commun.* 82 (2017) 129–133.
- [9] N.S. Choi, Z. Chen, S.A. Freunberger, X. Ji, Y.K. Sun, K. Amine, G. Yushin, L.F. Nazar, J. Cho, P.G. Bruce, Challenges facing lithium batteries and electrical double-layer capacitors, *Angew. Chem. Int. Ed.* 51 (2012) 9994–10024.
- [10] M. Chen, Z.A. Goodwin, G. Feng, A.A. Kornyshev, On the temperature dependence of the double layer capacitance of ionic liquids, *J. Electroanal. Chem.* 819 (2018) 347–358.
- [11] R. Parsons, The electrical double layer: recent experimental and theoretical developments, *Chem. Rev.* 90 (1990) 813–826.
- [12] I. Yang, S.G. Kim, S.H. Kwon, M.S. Kim, J.C. Jung, Relationships between pore size and charge transfer resistance of carbon aerogels for organic electric double-layer capacitor electrodes, *Electrochim. Acta* 223 (2017) 21–30.
- [13] A. Auer, X. Ding, A.S. Bandarenka, J. Kunze-Liebhäuser, The potential of zero charge and the electrochemical interface structure of Cu(111) in alkaline solutions, *J. Phys. Chem. C* 125 (2021) 5020–5028.
- [14] B. Garlyyev, S. Xue, S. Watzele, D. Scieszka, A.S. Bandarenka, Influence of the nature of the alkali metal cations on the electrical double layer capacitance of model Pt(111) and Au(111) electrodes, *J. Phys. Chem. Lett.* 9 (2018) 1927–1930.
- [15] S. Xue, B. Garlyyev, A. Auer, J. Kunze-Liebhäuser, A.S. Bandarenka, How the nature of the alkali metal cations influences the double layer capacitance of Cu, Au and Pt single crystal electrodes, *J. Phys. Chem. C* 124 (2020) 12442–12447.
- [16] B. Garlyyev, S. Xue, M.D. Pohl, D. Reinisch, A.S. Bandarenka, Oxygen electroreduction at high-index Pt electrodes in alkaline electrolytes: a decisive role of the alkali metal cations, *ACS Omega* 3 (2018) 15325–15331.
- [17] S. Xue, B. Garlyyev, S. Watzele, Y. Liang, J. Fichtner, M.D. Pohl, A.S. Bandarenka, Influence of alkali metal cations on the hydrogen evolution reaction activity of Pt, Ir, Au and Ag electrodes in alkaline electrolytes, *ChemElectroChem* 5 (2018) 2326–2329.
- [18] E. Pérez-Gallent, G. Marcandalli, M.C. Figueiredo, F. Calle-Vallejo, M.T.M. Koper, Structure- and potential dependent cation effects on CO reduction at copper single-crystal electrodes, *J. Am. Chem. Soc.* 139 (2017) 16412–16419.
- [19] I. Ledezma-Yanez, W.D.Z. Wallace, P. Sebastián-Pascual, V. Climent, J.M. Feliu, M.T.M. Koper, Interfacial water reorganization as a pH-dependent descriptor of the hydrogen evolution rate on platinum electrodes, *Nat. Energy* 2 (2017) 17031.
- [20] L. Katzenmeier, S. Helmer, S. Braxmeier, E. Knobbe, A.S. Bandarenka, Properties of the space charge layers formed in Li-ion conducting glass ceramics, *ACS Appl. Mater. Interfaces* 13 (2021) 5853–5860.
- [21] R.D. Armstrong, B.R. Horrocks, The double layer structure at the metal-solid electrolyte interface, *Solid State Ion.* 94 (1997) 181–187.
- [22] A. Lasia, Impedance of the faradaic reactions in the presence of adsorption, in: A. Lasia (Ed.), *Electrochemical Impedance Spectroscopy and Its Applications*, Springer, New York, 2014, pp. 127–145.
- [23] A.S. Bandarenka, Exploring the interfaces between metal electrodes and aqueous electrolytes with electrochemical impedance spectroscopy, *Analyst* 138 (2013) 5540–5554.
- [24] J.P. Sabawa, F. Haimerl, F. Riedmann, T. Lochner, A.S. Bandarenka, Dynamic and precise temperature control unit for PEMFC single-cell testing, *Eng. Rep.* (2020) e12345.
- [25] J.P. Sabawa, A.S. Bandarenka, Applicability of double layer capacitance measurements to monitor local temperature changes at polymer electrolyte membrane fuel cell cathodes, *Results Chem.* 2 (2020) 100078.

- [26] J. Solla-Gullón, P. Rodríguez, E. Herrero, A. Aldaz, J.M. Feliu, Surface characterization of platinum electrodes, *Phys. Chem. Chem. Phys.* 10 (2008) 1359–1373.
- [27] G.A. Ragoisha, N.P. Osipovich, A.S. Bondarenko, J. Zhang, S. Kocha, A. Iiyama, Characterisation of the electrochemical redox behaviour of Pt electrodes by potentiodynamic electrochemical impedance spectroscopy, *J. Solid State Electrochem.* 14 (2010) 531–542.
- [28] M.D. Pohl, V. Colic, D. Scieszka, A.S. Bandarenka, Elucidation of adsorption processes at the surface of Pt(331) model electrocatalysts in acidic aqueous media, *Phys. Chem. Chem. Phys.* 18 (2016) 10792–10799.
- [29] G.A. Ragoisha, N.P. Osipovich, A.S. Bondarenko, J. Zhang, S. Kocha, A. Iiyama, Characterisation of the electrochemical redox behaviour of Pt electrodes by potentiodynamic electrochemical impedance spectroscopy, *J. Solid State Electrochem.* 14 (2010) 531–542.
- [30] N. Garcia-Araez, V. Climent, E. Herrero, J.M. Feliu, J. Lipkowski, Thermodynamic approach to the double layer capacity of a Pt (111) electrode in perchloric acid solutions, *Electrochim. Acta* 51 (2006) 3787–3793.
- [31] D. Bolmatov, V. Brazhkin, K. Trachenko, The phonon theory of liquid thermodynamics, *Sci. Rep.* 2 (2012) 1–6.
- [32] S. Moldoveanu, V. David, *Essentials in Modern HPLC Separations*, Elsevier, Waltham, USA, 2013.
- [33] J. Tymoczko, F. Calle-Vallejo, V. Colic, M.T.M. Koper, W. Schuhmann, A.S. Bandarenka, Oxygen reduction at a Cu modified Pt(111) model electrocatalyst in contact with NAFION polymer, *ACS Catal.* 4 (2014) 3772–3778.
- [34] M. Obermaier, A.S. Bandarenka, C. Lohri-Tymozhynsky, A comprehensive physical impedance model of polymer electrolyte fuel cell cathodes in oxygen-free atmosphere, *Sci. Rep.* 8 (2018) 4933.
- [35] T.D. Gierke, G.E. Munn, F.C. Wilson, The morphology in nafion[®] perfluorinated membrane products, as determined by wide- and small-angle x-ray studies, *J. Polym. Sci., Polym. Phys. Ed.* 19 (1981) 1687–1704.
- [36] W.Y. Hsu, T.D. Gierke, Ion transport and clustering in nafion perfluorinated membranes, *J. Membr. Sci.* 13 (1983) 307–326.
- [37] S. Cui, J. Liu, M.E. Selvan, D.J. Keffer, B.J. Edwards, W.V. Steele, A molecular dynamics study of a Nafion polyelectrolyte membrane and the aqueous phase structure for proton transport, *J. Phys. Chem. B* 111 (2007) 2208–2218.
- [38] T. Thompson, A. Sharafi, M.D. Johannes, A. Huq, J.L. Allen, J. Wolfenstine, J. Sakamoto, A tale of two sites: On defining the carrier concentration in Garnet-based ionic conductors for advanced Li batteries, *Adv. Energy Mater.* 5 (2015) 1–9.
- [39] L. Katzenmeier, L. Carstensen, S.J. Schaper, P. Müller-Buschbaum, A.S. Bandarenka, Characterization and quantification of depletion and accumulation layers in solid-state Li⁺-conducting electrolytes using in situ spectroscopic ellipsometry, *Adv. Mater.* 33 (2021), doi:10.1002/adma.202100585.
- [40] S.A. Pervez, M.A. Cambaz, V. Thangadurai, M. Fichtner, Interface in solid-state lithium battery: challenges, progress, and outlook, *ACS Appl. Mater. Interfaces* 11 (2019) 22029–22050.
- [41] K. Okita, K.I. Ikeda, S. H., Y. Iriyama, H. Sakaebe, Stabilizing lithium plating-stripping reaction between a lithium phosphorus oxynitride glass electrolyte and copper thin film by platinum insertion, *J. Power Sources* 196 (2011) 2135–2142.

9.3 Visualizing SCLs with Spectroscopic Ellipsometry.

RESEARCH ARTICLE

ADVANCED
MATERIALS
www.advmat.deCharacterization and Quantification of Depletion and Accumulation Layers in Solid-State Li⁺-Conducting Electrolytes Using In Situ Spectroscopic Ellipsometry

Leon Katzenmeier, Leif Carstensen, Simon J. Schaper, Peter Müller-Buschbaum, and Aliaksandr S. Bandarenka*

The future of mobility depends on the development of next-generation battery technologies, such as all-solid-state batteries. As the ionic conductivity of solid Li⁺-conductors can, in some cases, approach that of liquid electrolytes, a significant remaining barrier faced by solid-state electrolytes (SSEs) is the interface formed at the anode and cathode materials, with chemical instability and physical resistances arising. The physical properties of space charge layers (SCLs), a widely discussed phenomenon in SSEs, are still unclear. In this work, spectroscopic ellipsometry is used to characterize the accumulation and depletion layers. An optical model is developed to quantify their thicknesses and corresponding concentration changes. It is shown that the Li⁺-depleted layer (≈190 nm at 1 V) is thinner than the accumulation layer (≈320 nm at 1 V) in a glassy lithium-ion-conducting glass ceramic electrolyte (a trademark of Ohara Corporation). The in situ approach combining electrochemistry and optics resolves the ambiguities around SCL formation. It opens up a wide field of optical measurements on SSEs, allowing various experimental studies in the future.

1. Introduction

The ever increasing demand for energy storage has led to the lithium-ion battery (LiB) invention with its first commercialization in 1991.^[1] After 30 years, this battery technology still dominates the market today with its ubiquitous use in mobile phones and battery electric vehicles.^[2] However, the holy grail of anode materials, metallic Lithium, is thought of as being inapplicable to conventional LiBs as the dendrite formation cannot be mitigated so far in a system using liquid electrolytes.^[3] All-solid-state batteries could be a possible solution,^[4] in which a solid-state electrolyte (SSE) replaces the liquid electrolyte and the separator of a conventional battery, posing an impenetrable barrier to lithium dendrites.^[5] The resulting thin-film battery should then have a much

higher gravimetric and volumetric energy density, provided that the SSE is sufficiently thin.^[6] However, a stack of solid materials introduces a set of different challenges, mainly at the interfaces. The issues of mechanical instability^[7] and interphase formation^[8] leading to a high interface resistance need to be addressed.^[9] One can mitigate these problems by using an additional layer^[10] or controlled formation of Li-ion conducting passivation layers.^[11] Mitigating these problems leaves the high interface resistance's physical origin unexplained. Space charge layer (SCL) formation in SSEs with a single mobile charge species has been suggested as early as 1981.^[12] Similar to the double layer formation in liquids, the SCL forms at any interface between two materials with different (electro-)chemical potentials. The prime example is the solid-solid interface between electrode and electrolyte.

In liquid electrolytes, the interface of two materials with different ionic and electronic conductivities is well understood.^[13] The theory of the so-called electrochemical double layers has been under development for more than 100 years with the description of a very compact (sub-nm) Helmholtz layer and a diffuse layer (up to 50 nm) reaching further into the electrolyte but with a lower ion concentration change.^[14]

The same layer structure was found when investigating the electrochemical nature of these SCLs in blocking conditions, with no interfacial Li⁺ transfer, as elucidated in previous work.^[15]

L. Katzenmeier, L. Carstensen, Prof. A. S. Bandarenka
Physics of Energy Conversion and Storage
Department of Physics
Technische Universität München
James-Franck-Str. 1, Garching 85748, Germany
E-mail: bandarenka@ph.tum.de

L. Katzenmeier
Bayerisches Zentrum für Angewandte Energieforschung
Magdalene-Schoch-Str. 3, Würzburg 97074, Germany
S. J. Schaper, Prof. P. Müller-Buschbaum
Lehrstuhl für Funktionelle Materialien
Physik-Department
Technische Universität München
James-Franck-Str. 1, Garching 85748, Germany

Prof. P. Müller-Buschbaum
Heinz Maier-Leibnitz Zentrum (MLZ)
Technische Universität München
Lichtenbergstr. 1, Garching 85748, Germany
Prof. A. S. Bandarenka
e-conversion Excellence Cluster
Lichtenbergstr. 4, Garching 85748, Germany

The ORCID identification number(s) for the author(s) of this article can be found under <https://doi.org/10.1002/adma.202100585>.

© 2021 The Authors. Advanced Materials published by Wiley-VCH GmbH. This is an open access article under the terms of the Creative Commons Attribution License, which permits use, distribution and reproduction in any medium, provided the original work is properly cited.

DOI: 10.1002/adma.202100585

Adv. Mater. 2021, 2100585

2100585 (1 of 6)

© 2021 The Authors. Advanced Materials published by Wiley-VCH GmbH

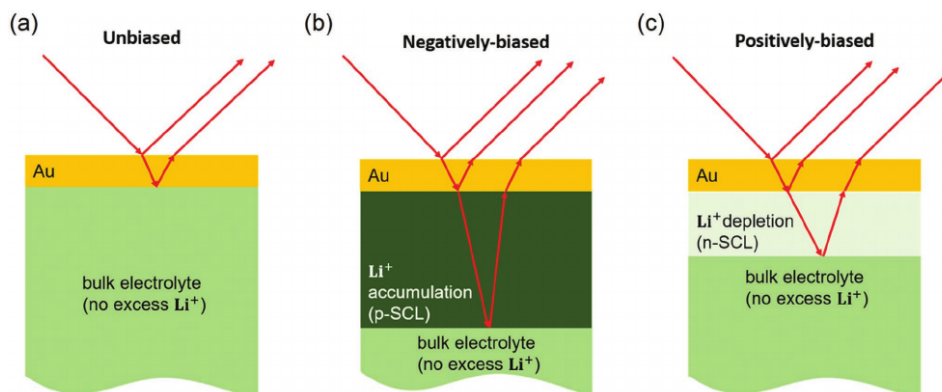


Figure 1. Schematic representation of the sample set-up consisting of the solid-state electrolyte (green) and the gold electrode (yellow). The red arrows schematically mark the light path during the ellipsometer measurement: a) layer model without bias potential, b) with an additional Li^+ -accumulation layer (dark green), and c) with an Li^+ -depletion layer (light green).

Upon applying a bias potential to the SSE under blocking conditions, the bulk of the electrolyte will be shielded by two oppositely charged layers formed at the interfaces between electrodes and electrolyte. Adjacent to the negatively biased electrode, the only mobile species (Li^+) will accumulate on vacant lattice sites to form an accumulation layer. In the following, we call this a “positive SCL” (p-SCL). Hence, the vacancies’ density creates a boundary condition to the maximum concentration of Li^+ in such a layer. As global charge neutrality must hold for the electrolyte in blocking conditions, the p-SCL must have a counterpart, that is, a Li^+ -depletion layer. This “negative SCL” (n-SCL) will form at the SSE’s positively biased side. Here, the concentration of mobile Li^+ forms the boundary condition, as this is the maximum depletion achievable. It is essential to notice that the concentration of free vacancies and mobile Li^+ does not have to be equal, leading to a possible asymmetry of both SCL thickness and concentration. However, the total charge depleted and accumulated has to match if the electrolyte is under blocking conditions.

The advancement of SSE’s led researchers working on battery technology to investigate this issue experimentally and theoretically. However, the conclusions are contradictory and range from: i) layers of a few hundred nanometers thickness and significant impact^[16,17] to ii) negligible impact and only a single nanometer thickness.^[18,19]

Within the class of solid electrolytes, oxides excel at atmospheric stability and processability, making them an attractive model material system.^[20] A commonly used glass-ceramic of this type is the lithium-ion-conducting glass ceramic (LICGC), a trademark of Ohara Corporation, a polycrystalline material with main crystalline compounds of $\text{Li}_2\text{O}-\text{Al}_2\text{O}_3-\text{SiO}_2-\text{P}_2\text{O}_5-\text{TiO}_2-\text{GeO}_2$, which is the material studied in this work. Although it is such a well-studied material, the exact material parameters, for example, the cation and vacancy densities, still remain unknown. Knowledge about these parameters would greatly benefit theoretical work and could be used to validate experimental findings mathematically.

In this work, we show that an optical method, spectroscopic ellipsometry, combined with a semi-empirical model for the optical properties of the SCL can be used to elucidate the formation of asymmetric SCLs. It is important to note, that the experimental resolution (nm) does not allow to account for the compact double layer (sub-nanometer). **Figure 1** shows the layer structure of the charge accumulation and depletion depending on the bias for only the top electrode for three cases. Figure 1a) corresponds to no applied potential, Figure 1b) corresponds to the negative applied potential, and Figure 1c) corresponds to the positive applied potential.

The in situ approach allows comparison of these findings to previously published work.^[15] Furthermore, the exact concentration changes in and the thickness of these layers are determined with fits using an effective medium approximation (EMA). Similar to the eye visible, optical changes of Li-intercalation into a graphite anode,^[21] we assumed that the presence and absence of Lithium do change the optical properties in a way detectable by the ellipsometer. Significant changes of the refractive index and extinction coefficient in the visible range upon Li^+ de-/intercalation were quantified for lithium manganese oxide.^[22]

2. Results and Discussion

The SSE’s polycrystalline nature can be observed in the scanning electron microscopy image (**Figure 2a**), with grain sizes of a few hundred nanometers. The interface toward the blocking electrode (marked red in **Figure 2a**) is planar and smooth, indicating a surface roughness below ten nanometers. Knowledge of the physical layer structure is key to building an optical model, and surface roughness is generally considered an obstacle for building quantitative ellipsometry fits.^[23] Therefore, the thickness of the gold electrode and the interface roughness are investigated using X-ray reflectivity (XRR) measurements

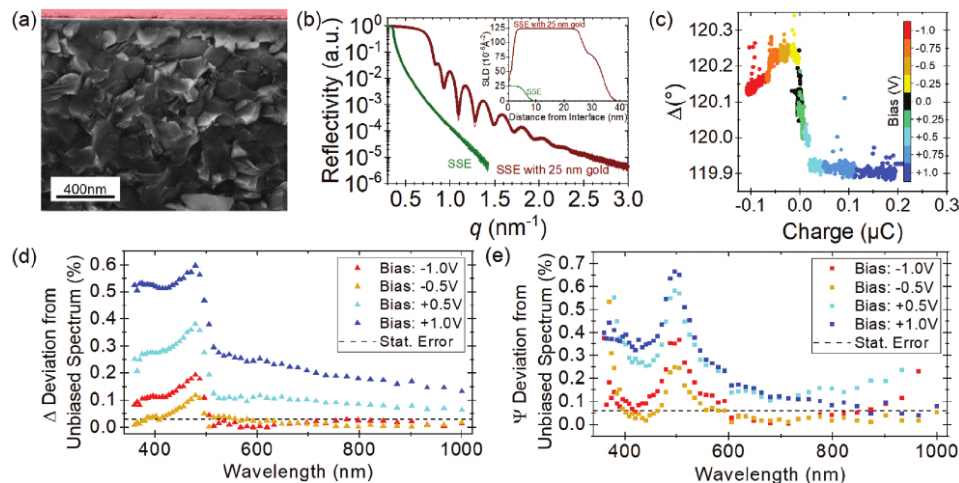


Figure 2. a) Scanning electron microscopy image of the electrolyte in a cross-sectional view with the gold electrode marked in red. b) XRR and SLD (embedded diagram) of the SSE with (red) and without gold electrode (green). c) The dependency of the ellipsometric angle Δ on the electric charge at different bias potentials. d,e) Changes to the unbiased spectrum in Δ (d) and Ψ (e) as a function of the wavelength at different bias potentials. The average statistical errors are given as a dashed black line in both plots to show the sensitivity of the ellipsometer.

(Figure 2b). As can be observed in the scattering length distribution (SLD) (inset in Figure 2b) resulting from the analysis of the XRR data, the gold surface and the gold/electrolyte interface show a non-negligible roughness and mixing. The bare electrolyte ($SLD_{SSE} = (25.773 \pm 0.001) \times 10^{-6} \text{ \AA}^{-2}$) is fitted with the Motofit²⁴ plugin for Igor, while a surface layer ($SLD_{SSE \text{ surface}} = (25.217 \pm 0.006) \times 10^{-6} \text{ \AA}^{-2}$) with a thickness of $(5.1 \pm 0.1) \text{ nm}$ and roughness of $(1.5 \pm 0.1) \text{ nm}$ is present. Using a three-layer model on top of the bulk SSE (SSE/Au-interface, Au, Au/air-surface) for the XRR of the Au/SSE sample, the SSE/Au-interface is determined to be less than 2 nm thick, which is in good agreement with the roughness of the SSE surface layer. The best fit for the SSE/Au-interface layer is achieved with a thickness of $(0.5 \pm 0.8) \text{ nm}$ and a roughness of $(0.9 \pm 0.2) \text{ nm}$. The thickness of the Au layer ($SLD_{Au} = 124.0 \times 10^{-6} \text{ \AA}^{-2}$) is fit to $(24.9 \pm 0.2) \text{ nm}$ with a roughness of $(1.3 \pm 0.1) \text{ nm}$, and the Au/air surface layer ($SLD_{Au/air} = (81 \pm 5) \times 10^{-6} \text{ \AA}^{-2}$) has a thickness of $(7.4 \pm 0.5) \text{ nm}$ with a roughness of $(2.2 \pm 0.2) \text{ nm}$. The surface layer found on the bare SSE cannot be resolved with evaporated Au on top due to the high contrast of Au compared to very small SLD difference between the surface layer and bulk SSE. At the SSE-(interlayer)-lithium electrode interfaces, alloy formation of Li-Ge, Li-In, Li-Al, Li-Pt, and Li-Au is reported in the literature,^[25] but the structure of the SSE affects the type of species forming at the interface.^[26] Without a lithium electrode present in our sample, it is unlikely that an alloy is forming at the SSE-Au interface.

As SSE optics are not frequently investigated, and optical properties are largely unknown, UV-vis transmission measurements are performed on both pure SSE and Au/SSE samples (Figure S1, Supporting Information). The transmission

spectrum of the Au/SSE/Au sample later used for in situ experiments, shows $\approx 3.8\%$ transmission for wavelengths above 500 nm. While no transmission spectra for the Au/SSE system are known in the literature, thermally evaporated Au thin films have shown similar transmission values in the investigated range.^[27] The penetration of light through the Au layer into the SSE is a prerequisite for any ellipsometric investigation of the SCL underneath the Au electrode. In a spectroscopic ellipsometry measurement of the bare SSE at an angle of incidence (AOI) of 50° shown in Figure S2, Supporting Information, the ellipsometric angles Ψ and Δ follow a well-defined trend. A Cauchy model is used to fit the dispersion relation (parameters in Figure S2b, Supporting Information) and forms the baseline for the SSE's optical description. When an Au layer is added to the SSE, the model includes the bare SSE, the Au, and an additional mixing layer accounting for the interface roughness. The spectroscopic measurement of the Au/SSE is shown in Figure S2c, Supporting Information. This completes the description of the sample in electrochemical equilibrium.

With these prerequisites in mind, we link electrochemistry and ellipsometry in situ. To show that changes in the electrochemical condition of the sample can be correlated with a change of optical properties, the ellipsometric angles Ψ and Δ are recorded while applying a staircase potential bias between -1 and 1 V . The in situ approach allows for simultaneous measurement of the current flow, which is integrated over time to give the amount of charge. Figure 2c shows the correlation of Δ and charge, which indicates that the formation of an additional layer at the Au/SSE interface can be observed with monochromatic ellipsometry ($\lambda = 658 \text{ nm}$, AOI 65°). While the monochromatic in situ observation of the ellipsometric angles shows

that the impact of the electrochemistry can be measured using ellipsometry, spectroscopic measurements are required to fit a quantitative model to the data.

The elemental distribution for all constituents is determined with energy-dispersive X-ray (EDX) measurements and independent of the bias potentials (see Figure S3, Supporting Information). This rules out that any other stoichiometric change at the Au/SSE interface causes the probed changes in optical parameters.

The changes in spectroscopic ellipsometry angles under the application of a bias potential with respect to the 0 V baseline are shown in Figure 2d,e. The model to fit the spectroscopic ellipsometry data (see Figure S4, Supporting Information) consists of dispersion relations and a thickness for each layer, as sketched in Figure 1. The model Au-Gold_Q-Sense-Quartz to describe the Au layer is part of the EP4Model software, which only leaves the thickness as a fitting parameter. The model for the bare SSE is the Cauchy model as described in Figure S2, Supporting Information, which is a semi-empirical description. The SCL is modeled by an EMA, a common tool in optics. In an EMA, the dispersion relation of a host material, here the SSE described by the Cauchy model, is mixed with that of a guest material (here: Li^+). The Bruggemann model for EMAs is based on ellipsoidal inclusions of a phase with different optical properties.^[28] The SCL is described by the mixing coefficient c_{SCL} (fraction of Li^+ in SSE) and the layer thickness d_{SCL} , which are two degrees of freedom of the final layer model fitted to the ellipsometric spectra obtained at different bias potentials. As the bulk already contains a certain amount of Li^+ , negative concentration changes are allowed to account for the depletion of Li^+ . Therefore, the changes in Li^+ concentration are measured as a deviation from the bulk concentration in vol%. The change of the

Li^+ concentration directly impacts the optical properties of the mixed layer, as shown in Figure S5, Supporting Information.

It is important to notice that the bulk electrolyte is mathematically represented as a substrate within the model, which leads to an infinite layer thickness. Practically, this means that only the interface closer to the incident light beam is present in the model, an assumption based on the ellipsometer's focus point. Thus, for negative bias potentials, the p-SCL is observed, whereas, for positive bias potentials, the n-SCL is observed, as shown in Figure 1.

While polarization of the electrolyte can cause a change in optical properties,^[29] this effect can be ruled out based on two arguments: i) a polarization should cause a symmetric change in isotropic materials and ii) the potential drop in case of SCLs only happens in the vicinity of the electrodes and therefore the bulk stays unpolarized.

The results of the model fit for the SCL to the spectroscopic ellipsometry data under different bias conditions are shown in Figure 3. The small parameter errors <10% relative to absolute change >100% (d_{SCL} , c_{SCL}) and the RMSE <11.5% (see Table S1, Supporting Information) prove the mathematical validity of this approach and the model. As no literature precedent exists to our knowledge, future work can replace the semi-empirical description with a physically motivated model.

Noticeably, the changes in Li^+ concentration c_{SCL} and layer thickness d_{SCL} show a highly asymmetric behavior. The n-SCL shows a more significant change in concentration, together with a thinner thickness than the p-SCL, which matches the expectation of an asymmetric formation of SCLs in SSE. To further validate the model, it is also used to fit the 0 V ellipsometric spectrum yielding a vanishing layer thickness and a concentration with a large error.

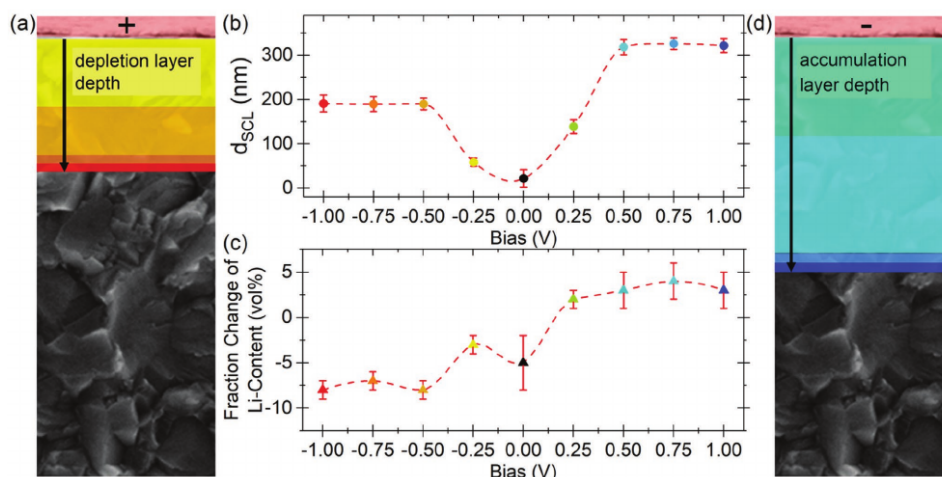


Figure 3. a,d) Color-coded representation of the SCL growth of the n-SCL (a) and the p-SCL (d) at different bias potentials. b) Layer thickness and c) change in Li^+ concentration compared to the bulk concentration as a function of the bias potential. The red lines in (b) and (c) are auxiliary lines for better visual guidance.

As expected, the concentrations reach an upper and lower limit for the corresponding polarizations, which is in good agreement with theoretical considerations of boundary conditions of the SSE's crystal lattice. The maximum concentration change is (-8 ± 1) vol% and $(+4 \pm 2)$ vol% for the n-SCL and the p-SCL, respectively.

For higher polarizations, above an absolute value of 0.5 V, the SCLs grow into the electrolyte to hold the additional charges. The extension of the n-SCL perpendicular to the surface reaches a maximum of (190 ± 19) nm at -1 V. The much less concentrated p-SCL is growing to a maximum thickness of (321 ± 15) nm at 1 V.

Comparability of the different measurements is ensured by the fact that the illuminated spot is the same throughout all spectra. Hence, we are not looking at other areas of the material but only at its electrochemical state in situ. The calculated n-SCL thickness is in good agreement with the order of magnitude found using impedance spectroscopy in earlier work.^[15]

The absolute number of charges $n_{\text{Li,excess}}$ can be calculated using Equation (1) to be of the order of $1 \mu\text{mol Li}^+$ (see Table S1, Supporting Information) and matches the expected symmetric behavior of charge redistribution in blocking conditions. As blocking conditions are used in this work, this can be seen as further proof of the method's accuracy.

$$n_{\text{Li,excess}} [\text{mol}] = \frac{V_{\text{Li,excess}} [\text{cm}^3] \rho_{\text{Li}} [\text{g cm}^{-3}]}{m_{\text{Li}} [\text{g mol}^{-1}]} \quad (1)$$

$$V_{\text{Li,excess}} [\text{cm}^3] = c_{\text{SCL}} [\%] A [\text{cm}^2] d_{\text{SCL}} [\text{cm}]$$

Here m_{Li} is the Li molar mass, ρ_{Li} the Li density and A the electrode area. The variables c_{SCL} and d_{SCL} are the concentration change and thickness of the charged layer, respectively.

A comparison to the recorded current and its integration over time, that is the charge accumulation, is hindered by the ambiguous contributions of electronic leakage, polarization, and the very low current (nA) measured by the potentiostat as possible errors are integrated over time. Even a three-electrode setup, which would allow accounting for the polarization and electronic leakage, would not give the true current flow from the n-SCL to the p-SCL as some space charge would form around the reference electrode. A dynamic analysis of the space charge formation is beyond the scope of this study.

3. Conclusion

In situ ellipsometry allows detection of the formation of SCL under different bias potentials. With monochromatic transient measurements, the formation of an additional layer at the interface is proven once a bias potential is applied. The correlation of ellipsometric angles and the redistributed charge is not unambiguous. A semi-empirical model, based on a three-layer model with a dispersion relation for each constituent of the structure, is used to fit the spectroscopic ellipsometry data and quantify the SCL formation. The suspected asymmetry is visible in the data with a wider, but less concentrated p-SCL ((322 ± 16) nm at 1 V) compared to the thinner n-SCL ((191 ± 19) nm at -1 V).

Charges are shown to be only redistributed, as the impact of total charge redistribution is symmetric for n-SCL and p-SCL. These findings are a proof-of-concept for applying spectroscopic ellipsometry in the detection of thin, electrochemical layers with a resolution in the nanometer-scale. The quantification of concentration changes of Li^+ inside the SCLs can be used to parameterize and validate a wide range of theoretical models. A profound understanding of the physical extent to which the SSE can be depleted of mobile charges is fundamental to understanding possible mitigation strategies, and we believe that future research in this area can use the findings of this work.

4. Experimental Section

SSE: LICGC (Ohara Inc, Japan) was used for electrochemical and optical experiments conducted in this study. The SSE had a thickness of 150 μm and was stable in the ambient atmosphere.

Gold Electrodes: The gold current collectors were deposited using an e-beam evaporator, Leybold 540 (Leybold, Germany), using a circular mask (radius = 7.5 mm) under high vacuum conditions (value is 3×10^{-7} mbar). The deposition rate (1 \AA s^{-1}) and final thickness (25 nm) were controlled with an IC6000 deposition controller (Inficon, Switzerland).

Spectroscopic Ellipsometry: An EP4 imaging ellipsometer (Accurion, Germany) was used to perform spectroscopic ellipsometry at different potentials and in situ ellipsometry was done at an AOI of 65° using a 658 nm solid-state laser. For spectroscopic measurements, the wavelength from 360 to 1000 nm in 50 equidistant photon energy steps was adjusted using a built-in grating monochromator, and a laser stabilized xenon arc lamp. A resting period of 2.5 h after applying the bias potential and before the spectroscopic scans was used to allow the system to reach electrochemical equilibrium.

Sample Polarization: The samples were contacted with a gold pin-contact on the front and a copper plate on the back. A proper contact was ensured by electrochemical impedance spectroscopy. A SP-150 Potentiostat (BioLogic, France) was used for applying the potentials. The working electrode connected to the gold pin-contact was set to the given voltage versus the counter electrode connected to the copper plate. The leakage currents after the aforementioned rest period of 2.5 h were consistent with the expected electronic leakage.

XRR: A D8 Advanced X-ray reflectometer (Bruker AXS, Germany) with a copper K_α source (wavelength 0.154 nm) and a scintillation detector was used.

EDX: An INCA PentaFET-x3 EDX (Oxford Instruments, UK) together with the INCA software was used to measure the EDX spectra and determine the chemical compositions.

Supporting Information

Supporting Information is available from the Wiley Online Library or from the author.

Acknowledgements

This work is part of the ASS Bayern project funded by the Bavarian Ministry of Economic Affairs, Regional Development and Energy and it was supported by funding from the Deutsche Forschungsgemeinschaft (DFG, German Research Foundation) under Germany's Excellence Strategy-EXC 2089/1-390776260 (e-conversion). The authors would like to thank the BMW Group for their financial support of this study. The authors would like to thank Stephan Braxmeier for help with the EDX measurements.

Open access funding enabled and organized by Projekt DEAL.

Conflict of Interest

The authors declare no conflict of interest.

Author Contributions

The manuscript was written through the contributions of all authors. All authors approved the final version of the manuscript. L.K., L.C., and S.J.S. contributed equally to this work.

Data Availability Statement

The data that support the findings of this study are available from the corresponding author upon reasonable request.

Keywords

accumulation layers, solid Li-ion conductors, solid-state electrolytes, space charge layer, spectroscopic ellipsometry

Received: January 22, 2021

Revised: March 8, 2021

Published online:

- [1] J. Xie, Y.-C. Lu, *Nat. Commun.* **2020**, *11*, 113.
 [2] X. Zuo, J. Zhu, P. Müller-Buschbaum, Y.-J. Cheng, *Nano Energy* **2017**, *31*, 113.
 [3] D. Lin, Y. Liu, Y. Cui, *Nat. Nanotechnol.* **2017**, *12*, 194.
 [4] Y. Shen, Y. Zhang, S. Han, J. Wang, Z. Peng, L. Chen, *Joule* **2018**, *2*, 1674.
 [5] C.-Z. Zhao, H. Duan, J.-Q. Huang, J. Zhang, Q. Zhang, Y.-G. Guo, L.-J. Wan, *Sci. China: Chem.* **2019**, *62*, 1286.
 [6] F. Zheng, M. Kotobuki, S. Song, M. O. Lai, L. Lu, *J. Power Sources* **2018**, *389*, 198.

- [7] G. Bucci, B. Talamini, A. Renuka Balakrishna, Y.-M. Chiang, W. C. Carter, *Phys. Rev. Mater.* **2018**, *2*, 105407.
 [8] S. Wenzel, D. A. Weber, T. Leichtweiss, M. R. Busche, J. Sann, J. Janek, *Solid State Ionics* **2016**, *286*, 24.
 [9] H.-D. Lim, J.-H. Park, H.-J. Shin, J. Jeong, J. T. Kim, K.-W. Nam, H.-G. Jung, K. Y. Chung, *Energy Storage Mater.* **2020**, *25*, 224.
 [10] F. J. Q. Cortes, J. A. Lewis, J. Tippens, T. S. Marchese, M. T. McDowell, *J. Electrochem. Soc.* **2020**, *167*, 050502.
 [11] Y. Li, W. Zhou, X. Chen, X. Lü, Z. Cui, S. Xin, L. Xue, Q. Jia, J. B. Goodenough, *Proc. Natl. Acad. Sci. USA* **2016**, *113*, 13313.
 [12] A. A. Kornyshev, M. A. Vorotyntsev, *Electrochim. Acta* **1981**, *26*, 303.
 [13] D. C. Grahame, *Chem. Rev.* **1947**, *41*, 441.
 [14] O. Stern, *Z. Elektrochem. Angew. Phys. Chem.* **1924**, *30*, 508.
 [15] L. Katzenmeier, S. Helmer, S. Braxmeier, E. Knobbe, A. S. Bandarenka, *ACS Appl. Mater. Interfaces* **2021**, *13*, 5853.
 [16] T. Tsuchiya, Y. Itoh, Y. Yamaoka, S. Ueda, Y. Kaneko, T. Hirasawa, M.-a. Suzuki, K. Terabe, *J. Phys. Chem. C* **2019**, *123*, 10487.
 [17] N. J. J. de Klerk, M. Wagemaker, *ACS Appl. Energy Mater.* **2018**, *1*, 3230.
 [18] Y. Nomura, K. Yamamoto, T. Hirayama, S. Ouchi, E. Igaki, K. Saitoh, *Angew. Chem.* **2019**, *131*, 5346.
 [19] S. Braun, C. Yada, A. Latz, *J. Phys. Chem. C* **2015**, *119*, 22281.
 [20] Z. Wu, Z. Xie, A. Yoshida, Z. Wang, X. Hao, A. Abudula, G. Guan, *Renewable Sustainable Energy Rev.* **2019**, *109*, 367.
 [21] S. Kang, S. J. Yeom, H.-W. Lee, *ChemSusChem* **2020**, *13*, 1480.
 [22] Y. Joshi, E. Hadjixenophontos, S. Nowak, R. Lawitzki, P. K. Ghosh, G. Schmitz, *Adv. Opt. Mater.* **2018**, *6*, 1701362.
 [23] C. A. Fenstermaker, F. L. McCrackin, *Surf. Sci.* **1969**, *16*, 85.
 [24] A. Nelson, *J. Appl. Crystallogr.* **2006**, *39*, 273.
 [25] Z. Gao, H. Sun, L. Fu, F. Ye, Y. Zhang, W. Luo, Y. Huang, *Adv. Mater.* **2018**, *30*, 1705702.
 [26] L. Sang, R. T. Haasch, A. A. Gewirth, R. G. Nuzzo, *Chem. Mater.* **2017**, *29*, 3029.
 [27] A. Azelevitch, B. Apter, G. Golan, *Opt. Express* **2013**, *21*, 4126.
 [28] C. G. Granqvist, O. Hunderi, *Phys. Rev. B: Condens. Matter Mater. Phys.* **1978**, *18*, 1554.
 [29] V. Dimitrov, S. Sakka, *J. Appl. Phys.* **1996**, *79*, 1736.

9.4 Electrochemical Properties of Negative SCLs.

Properties of the Space Charge Layers Formed in Li-Ion Conducting Glass Ceramics

Leon Katzenmeier, Simon Helmer, Stephan Braxmeier, Edwin Knobbe, and Aliaksandr S. Bandarenka*

Cite This: *ACS Appl. Mater. Interfaces* 2021, 13, 5853–5860

Read Online

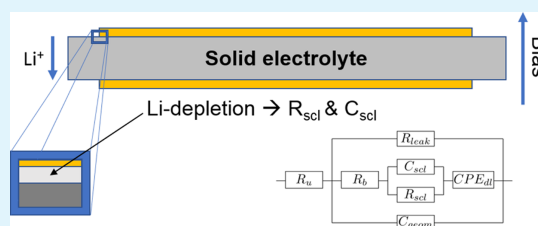
ACCESS |

Metrics & More

Article Recommendations

Supporting Information

Downloaded via Leon Katzenmeier on February 9, 2021 at 09:05:37 (UTC).
See <https://pubs.acs.org/sharingguidelines> for options on how to legitimately share published articles.



ABSTRACT: For years, the space charge layer formation in Li-conducting solid electrolytes and its relevance to so-called all solid-state batteries have been controversially discussed from experimental and theoretical perspectives. In this work, we observe the phenomenon of space charge layer formation using impedance spectroscopy at different electrode polarizations. We analyze the properties of these space charge layers using a physical equivalent circuit describing the response of the solid electrolytes and solid/solid electrified interfaces under blocking conditions. The elements corresponding to the interfacial layers are identified and analyzed with different electrode metals and applied biases. The effective thickness of the space charge layer was calculated to be ~ 60 nm at a bias potential of 1 V. In addition, it was possible to estimate the relative permittivity of the electrolytes, specific resistance of the space charge layer, and the effective thickness of the electric double layer (~ 0.7 nm).

KEYWORDS: solid Li-ion conductor, space charge layer, impedance spectroscopy, all solid-state batteries, double layer, space charge capacitance

INTRODUCTION

All solid-state batteries (ASSBs) are among the most promising candidates for the next-generation energy-storage devices and battery electric vehicles.^{1,2} Their potential inflammability and possible stability against dendrite formation³ can target at least two major challenges currently faced by traditional Li-ion batteries (LIBs):⁴ inflammability and energy density. The choice of the electrodes for ASSBs is in that case not restricted to those currently used in conventional LIBs, as the wide electrochemical stability window⁵ allows to use high-voltage cathodes and anodes. For instance, even the use of lithium metal anodes,⁶ the “holy-grail” of anode materials, has been proposed.

Polycrystalline solid Li-ion conductors, which should replace liquid electrolytes, however, introduce a set of new challenges. On one hand, the intergranular transport across and along grain boundaries poses an additional ion transport barrier.⁷ Although grain-boundaries have been shown to be another ion-conducting pathway with a lower ionic conductivity,⁶ the advances in sintering processes and the resulting decrease in porosity have mitigated these problems.⁸ On the other hand, the solid/solid interfaces between the electrodes and solid

electrolytes exhibit a higher interface impedance⁹ as well as certain stability issues,¹⁰ which can be grouped into a few categories: charge accumulation (which we explore in this work), mechanical stress,¹¹ and chemical decomposition.¹²

The solid electrolyte grains themselves have a crystal structure with fixed anions,¹³ in which Li-ions are normally transported by a hopping mechanism between certain adjacent lattice defects.¹⁴ The Li-ion concentration is limited by the number of defects per unit volume in the lattice¹⁵ with an upper and a lower boundary to the (local) Li-ion concentration. A defect lattice with no empty vacancies is positively charged due to an excess of Li-ions, whereas complete depletion of mobile Li-ions leads to an excess of

Received: November 30, 2020

Accepted: January 15, 2021

Published: January 25, 2021



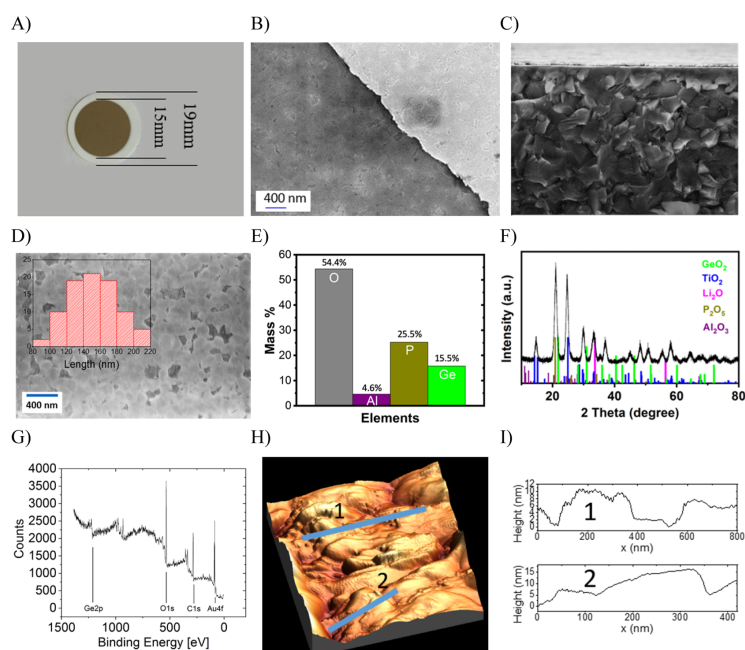


Figure 1. (A) Optical image of an Ohara glass sheet with 15 mm diameter Au-electrode. (B) SEM image of the gold/electrolyte (in-plane) boundary, spot darkened after the EDX measurement. (C) SEM cross-sectional image in breaking edge, thin Au layer on the planar surface. (D) Cross-sectional SEM image showing the grains and grain-boundaries with distribution of grain sizes. (E) Cross-sectional EDX element distribution of the pristine material; quantitative fits are given only for O, Al, P, and Ge. Li, Ti, and Si were not quantifiable with EDX. (F) XRD spectra of the pristine material with peak assignment to the metal oxides. (G) XPS data of the sample after gold evaporation indicating the presence of carbon on the surface layer. (H) Typical AFM image showing the surface morphology. (I) Two AFM line scans highlighting relatively small surface roughness.

negative (“anionic”) charge and consequently to a negatively charged region.

While several phenomena have been reasoned to explain interface resistance, theoretical works suggest the presence of two charge accumulation layers (ALs) on different depth scales in the form of Li-ion accumulation or depletion. While one phenomenon happens on the scale of a few nanometers, as suggested by a kinetic model,¹⁶ the other is a diffuse charge layer, which is validated in experiments^{17,18} and predicted by a thermodynamic model¹⁹ extending to as far as 1 μm into the electrolyte.²⁰

Experimental evidence for a charge layer hidden beneath an electrode is hard to achieve. Stoichiometry-sensitive techniques, such as X-ray photoelectron spectroscopy (XPS),²¹ X-ray diffraction (XRD),²² and energy dispersive X-ray spectroscopy (EDX)²³ in cross-sectional experiments show an additional interface toward air and face problems of nonuniform element distribution along the grains and grain-boundaries regardless of the presence of a charged layer. Electrochemical techniques, such as impedance spectroscopy or cyclic voltammetry, require a fundamental a priori understanding of the system before the data can be analyzed.

To explore the impact and formation of the space charge layers (SCLs), one should consider the nature of charge

accumulation and charge-neutral regions in solid electrolytes: the bulk of a solid electrolyte in electrochemical equilibrium should be charge neutral. Therefore, the numbers of Li-ions and negatively charged anions per unit volume are equal. An applied bias potential forces the only mobile charge species, that is Li-ions, to compensate for the electrochemical driving force near the electrodes, and a charged layer will form to shield the bulk electrolyte.²⁴ For liquid electrolytes, this behavior has been extensively described both in theory and experiments and is known as the formation of a diffuse double layer.²⁵ In solid electrolytes, the presence of an electrochemical potential difference, therefore, leads to the formation of a SCL on the “positive” electrode and an AL on the “negative” electrode. The formation of these layers is dependent on the external parameters such as the pressure, temperature, and sample geometry, as well as intrinsic material properties such as maximum number of Li-ions per unit volume, the dielectric properties, and most importantly, the free charge carrier density. While the external parameters are easily varied under experimental conditions, the intrinsic material properties remain only vaguely determined or completely unexplored. This fact not only hinders a straightforward interpretation of the experimental findings, but the missing parameterization renders theoretical models to be only qualitatively useful. A

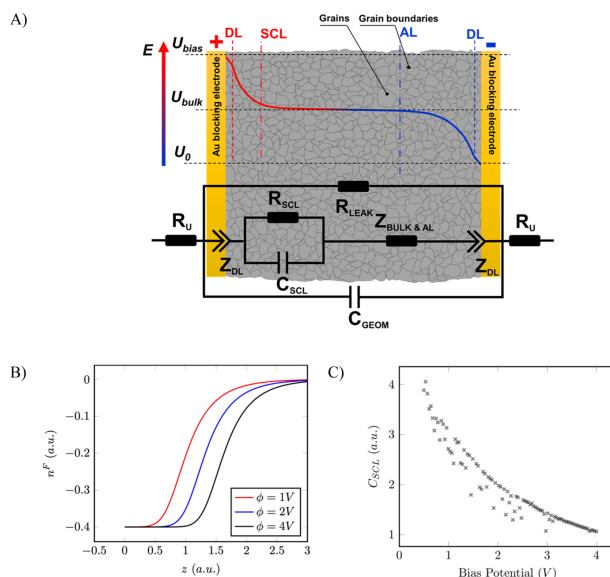


Figure 2. (A) Schematic representation of the proposed impedance model. It describes the response of the polycrystalline electrolyte and the interfaces between blocking Au electrodes and the electrolyte. R_U stands for the wire and side resistances. Z_{DL} is the impedance of the electrical double layer. R_{SCL} and C_{SCL} are the resistance and capacitance of the SCL, respectively. $Z_{BULK \& AL}$ is the impedance related to the bulk electrolyte, and the AL C_{GEOM} —geometrical capacitance and R_{LEAK} account for the leakage, e.g., because of electrolyte electron conductivity. (B) Free charge carrier spatial distribution in arbitrary units near the positively biased electrode interface obtained using a thermodynamic model described in the literature.¹⁹ Depending on the external bias, the SCL widens, as more charge accumulates in the limited vacancy lattice. Based on this, (C) shows the SCL capacitance calculated for different potentials in arbitrary units (fluctuations are due to the singularities in the thermodynamic model).

careful analysis of the experimental data for different external conditions in combination with a qualitative modeling approach is therefore needed to find the physical origin of the interface-related ion-transport barriers.

In this work, we use a model electrolyte with a blocking electrode configuration, and electrochemical impedance spectroscopy (EIS) was used to investigate the behavior of the solid/solid electrified interface. A physical model in terms of equivalent circuits has been developed to analyze the impedance data, reflecting bulk and interface contributions, and which is valid for a variety of external conditions. The resulting model parameters are logically correlated to the physical origin of the SCL, and its depth is in good qualitative agreement with the output of the theoretical modeling. The interface resistance caused by the SCL is quantified and found to be a major contribution to the overall interfacial impedance.

MATERIALS AND EXPERIMENTAL SECTION

Electrolytes. The solid electrolyte samples used in this work were 150 μm thick, 19 mm diameter Ohara LICG glass substrates. The main crystalline phase is $\text{La}_{1-x-y}\text{Al}_x(\text{Ti,Ge})_{2-y}\text{Si}_y\text{P}_{3-y}\text{O}_{12}$ with further AlPO_4 as stated by the manufacturer.²⁶ The results of in-depth characterization of the samples used in this work can be found in Figure 1. Figure 1A shows an optical image of the sample with formed blocking Au-electrode, and a uniform surface of the electrolyte can be seen in Figure 1B,C. Very small gaps between the grains with a mean diameter of 151 nm are found in Figure 1D. The composition of the

material is confirmed with EDX, XRD, and XPS in Figure 1E–G, respectively. Negligible surface roughness can be seen in Figure 1H,I.

Electrode Deposition. The electrodes (Au, Ti, Cr) were e-beam evaporated using an L560 (Leybold, Germany) evaporator under high vacuum conditions with a stainless-steel mask ($r = 7.5$ mm). The deposition rate of 1 $\text{\AA}/\text{s}$ was controlled by an IC-6000 deposition controller (Inficon, Switzerland). After electrode deposition, the samples were transferred to an argon glovebox with a highly inert atmosphere ($\text{O}_2 < 2$ ppm, $\text{H}_2\text{O} < 0.7$ ppm).

Electrochemical Impedance Spectroscopy. The AC impedance measurements were carried out with a VSP300 potentiostat (Biologic, France) in the frequency range between 5 MHz and 0.5 Hz with a probing signal amplitude of 10 mV. The metal-contacted samples were assembled into a PAT-Cell (EL-CELL, Germany) with polished stainless-steel plungers to contact the electrode area. The cells were placed into a PAT-Stand (EL-CELL, Germany) with a 3 m lead to the potentiostat. The impedance of the samples was measured in the temperature range between 5 and 60 $^\circ\text{C}$. For the temperature-dependent measurements, the cells were left to stabilize at the chosen temperature for 1 h before the EIS measurements were started. After applying the bias potential, a waiting time of 15 min was used to ensure electrochemical equilibrium. The impedance data were analyzed using the “EIS Data Analysis 1.3” software.²⁷

X-ray Diffraction. XRD data were obtained by a Siemens Bruker D5000 X-ray diffractometer (Siemens, Germany) with $\text{Cu K}\alpha$ X-ray radiation, in the 2θ of 10–70 $^\circ$ at an increment of 0.05 $^\circ$.

Scanning Electron Microscopy and EDX Spectroscopy. Measurements were performed using an Ultra Plus field emission-scanning electron microscope (Carl Zeiss Microscopy GmbH,

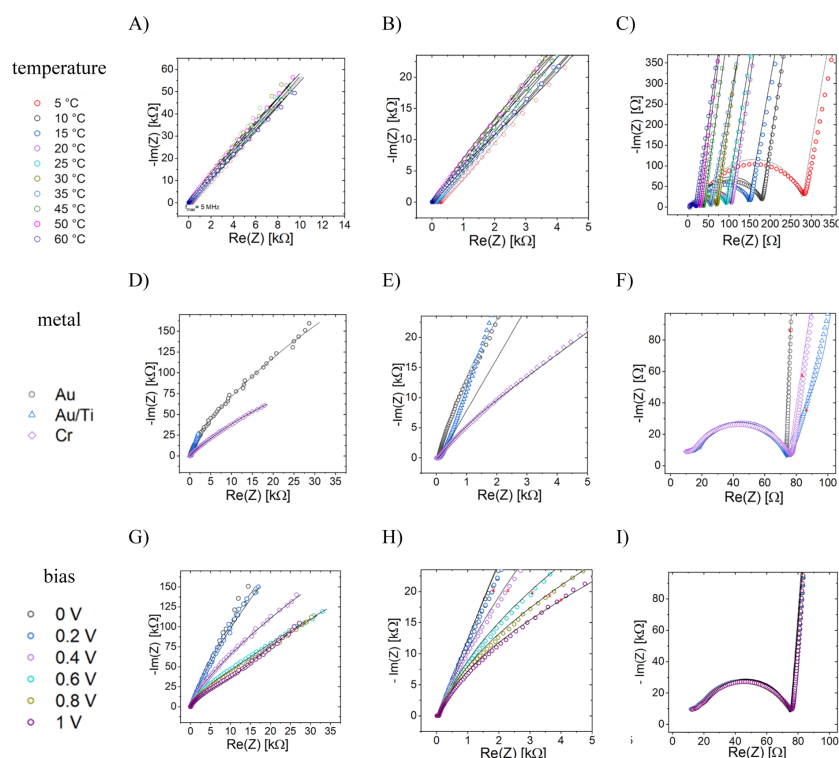


Figure 3. Nyquist plots of impedance spectra recorded under a variety of conditions (default: Au, 25 °C, $U_{\text{bias}} = 0$ V). Solid lines show the corresponding fit to the proposed equivalent circuit in Figure 2A. The red crosses in the plots indicate the same frequency in each plot. (A) Overview for the temperature range 5–60 °C, which shows a similar low-frequency behavior. (B) Mid-frequency region up to 1.5 Hz. (C) High-frequency semicircle showing a strong dependence on the temperature. (D–F) Different metals used as blocking electrodes: a clear impact on low- and mid-frequency behavior can be observed, while the high-frequency semicircle remains unchanged. (G–I) DC bias potential variation showing its strong impact on the spectra at lower frequencies.

Germany) with an INCAPentaFET-x3 EDX (Oxford Instruments, UK). For evaluation, the manufacturer's INCA software was used.

Thermodynamic Modeling. The complete set of equations and boundary conditions can be found in the literature.¹⁶ They were implemented in a single-client COMSOL Multiphysics runtime to calculate the one-dimensional (1D) concentration and potential profiles along the electrolyte lattice. An unevenly distributed mesh with elements in symmetric arithmetic spacing toward either end of the solid electrolyte was used to account for the thin interface features while not neglecting charge neutrality of the bulk.

RESULTS AND DISCUSSION

Model Development. When developing a physics-based equivalent circuit impedance model for a solid electrolyte, there are multiple processes and parameters to be considered. On a larger scale, the electrolyte between two electrified metal plates is a capacitor. Within the electrolyte, besides its ionic conductivity, the grain structure can impact the impedance and grain boundary effects must be considered. Different charge

accumulations can occur under bias conditions. The role of each physical contribution to the overall impedance equivalent circuit is explained in the following.

A geometric capacitance C_{GEOM} describes the behavior of the ionic conductor with moderate specific conductivity between two electron conductors (current collectors) under high-frequency AC probing and is connected in parallel to the other elements (Figure 2A). The impedance of the bulk electrolyte cannot only include the bulk resistance, as would be in the case of liquid electrolytes, but should also include contributions from the grain boundaries and, possibly, the SCL and is therefore summarized as $Z_{\text{BULK\&AL}}$. The grain boundary and space charge impedances are still widely discussed points in the literature, where the grain boundary effects are typically observable at temperatures well below room temperature.⁷ The model electrolyte of this work shows a very dense structure, as confirmed by the SEM image shown in Figure 1C. For these well-sintered samples, we assume a negligible contribution of

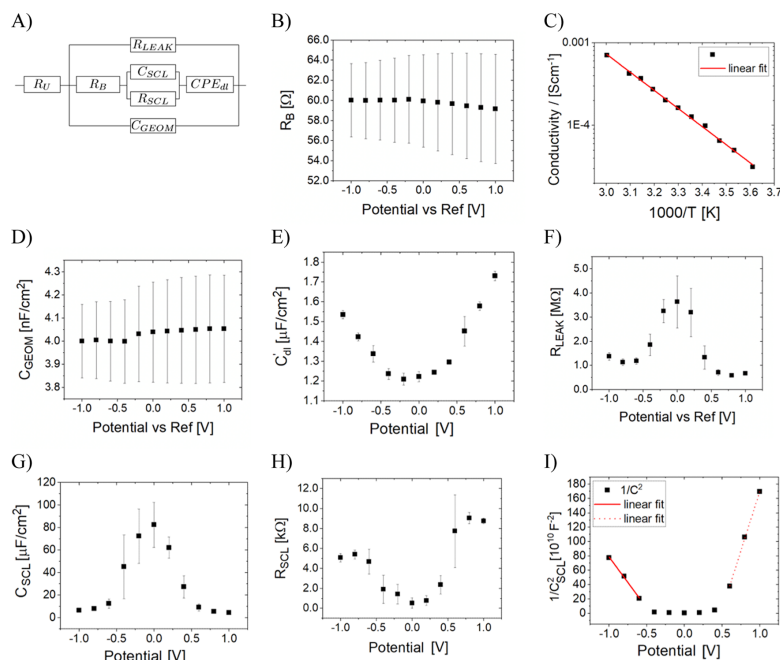


Figure 4. Dependencies of fitted impedance parameters of (A) simplified equivalent circuit model on the external bias (2-electrode configuration) ranging from -1 to 1 V (vs Au). (B) Bulk resistance (R_B). (C) Arrhenius behavior of the bulk conductivity. (D) Geometric capacitance (C_{GEOM}). (E) Double-layer capacitance (C_{DL}). (F) Leakage resistance (R_{LEAK}). (G) SCL capacitance (C_{SCL}). (H) SCL resistance (R_{SCL}). (I) Quasi Mott-Schottky behavior of the SCL capacitance.

the grain boundaries to the overall impedance response in accordance with work on a similar LAGP/LATP-electrolyte.²⁸

Within the phenomenon of the space charge formation, the effect of AL and SCL should be considered separately since they describe different kinds of physics ("collection" of ions vs "collection" of vacancies). The AL is assumed to be much wider with lower capacitance because it is based on the vacancy concentration distribution in the bulk. The impedance contributions of the bulk electrolyte, AL, and grain boundaries are assumed to convolute to a single model parameter, the aforementioned $Z_{\text{BULK\&AL}}$. As in most electrochemical systems, we also include a resistance R_U to account for unwanted wire and cell resistances.

The double-layer response and a possible leakage resistance due to electronic conductivity of the electrolyte are modeled with the constant phase element $Z_{\text{DL}} = C_{\text{dl}}^{n-1}(j\omega)^{-n}$ (where j is an imaginary unit, ω is the angular frequency, C_{dl} is assumed to be close to the double-layer capacitance, and exponent $1 > n > 0.7$ describes dissipation of the probing signal energy) and R_{LEAK} , respectively. A graphical representation of the proposed impedance model and the physical origins of its elements are schematically presented in Figure 2A in which the elements are arranged in a way corresponding to the geometry of the cell.

In addition to the analyses based on impedance spectroscopy, a thermodynamic model with finite element method

approximation was used to predict the trends in the space charge formation based on the thermodynamic model developed by Braun et al.¹⁹ In brief, this model assumes the Li-ions to move in a continuum of anions with thermodynamic equilibrium achieved by a redistribution at the interface. The formed SCL is shown in a 1D representation in Figure 2B and results in a capacity potential behavior shown in Figure 2C. A distinction between depletion and accumulation cannot be made within the scope of this model. A more detailed description can be found in the Supporting Information. While quantitative analysis is not possible due to missing material parameters (i.e., ion and defect concentration), the qualitative decrease in the SCL capacitance of 25% between 0 and 1 V can be later compared to our experimental findings.

Model Evaluation. Figure 3 shows the impedance spectra of the samples related to different experimental parameters, such as temperature, bias potentials, and the nature of the blocking electrodes. The developed equivalent circuit, mathematically simplified to that shown in Figure 4A, fits all frequency regions of the spectra well with the mean deviation below 2% and low individual parameter errors (less than 10%). This statistical evaluation of the impedance data shows that each element of the circuit has a significant contribution to the fit. To resolve possible ambiguity (e.g., SCL vs possible grain boundary contributions) of the central RC-element, viz. R_{SCL}

Parameter	Value
dielectric constant ϵ_r	677
SCL – thickness d_{SCL}	60nm
DL – thickness d_{DL}	0.7nm
SCL – specific resistance ρ_{SCL}	2580 M Ω cm

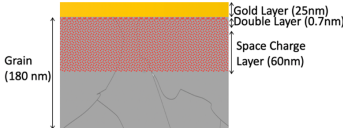


Figure 5. Results obtained in this work in table and geometric representations. Beneath the gold electrode, a thin electrochemical double layer forms followed by a thick SCL of up to ~ 60 nm at a bias potential of 1 V.

and C_{SCL} , it should be considered that the nature of metals used as the blocking electrodes should not influence the impedance of the grain boundaries, as this intragrain phenomenon is happening throughout the complete bulk of the electrolyte. If the RC-element, however, is linked to an interface phenomenon like SCL formation, the nature of the current collectors should have a significant impact on the values of the R and C element. The fitting results (equivalent circuit parameters are presented in Table S1), and the spectra shown in Figure 3D–F demonstrate that the capacitance and resistance designated in the equivalent circuit in Figure 4A as R_{SCL} and C_{SCL} depend on the nature of the electrodes. Therefore, we conclude that indeed those R and C elements correspond to the electrode/electrolyte (pre-)interfacial structures, namely the SCLs.

Dependency of the Equivalent Circuit Parameters. In the following, we focus on the electrolyte under blocking conditions with symmetric gold current collectors. Figure 4B–I shows a variation of the individual parameters as a function of the bias potentials. As expected, the bulk resistance $R_B = 60(\pm 2.7) \Omega$ (Figure 4B) stays practically constant, which is equivalent to $\sigma_{Li} = 1.5 \times 10^{-4} S/cm$ at room temperature, close to the manufacturer's specifications²⁶ of $\sigma_{Li,ref} = 1 \times 10^{-4} S/cm$ at $T = 25^\circ C$. As one would expect, the ionic conductivity of the bulk electrolyte does not change upon a modification of the interface (see Table S1). The activation energy of ~ 0.35 eV, which is calculated based on the Arrhenius plot shown in Figure 4C, is slightly higher than stated in the literature for similar materials.⁵⁹ This confirms that the estimated R_B arises indeed primarily from the bulk electrolyte. The values of the geometric capacitance (C_{GEOM}) remain also essentially constant with the change in the bias potential (Figure 4D) and are in the order of nano-farad. They are also well below those estimated for the other capacitances in the model. The dielectric constant of the solid electrolyte can thus be determined using $C_{GEOM} = \sim 4$ nF/cm², which results in the relative permittivity values of $\epsilon_r = \sim 677$ based on $C = \epsilon_0 \epsilon_r A/d$ (ϵ_0 : dielectric constant of vacuum, ϵ_r : dielectric constant of medium, A : electrode area, and d : the electrolyte thickness). The geometric capacitance does not depend on the nature of the electrodes, which supports the hypothesis that the origin of it lays in the bulk electrolyte.

It should be noted that the impedance behavior of the solid-state electrochemical systems under external polarization is rarely discussed in the literature. For instance, there are only a few studies that link the impedance spectra at different polarizations and loss functions to underlying physical quantities such as the jump-rate³⁰ and relaxation processes.³¹ The dielectric constant, as it is determined in this work, is used in the following for the calculation of the thickness of the SCL, although this implies that the impact of the changes in the

charge carrier concentration on the dielectric properties is neglected.

A typical double-layer capacitance dependency is shown in Figure 4E. Note that the double-layer impedance Z_{dl} is assumed to be a true capacitor C_{dl} . The capacitance increases when the bias is applied, with the minimum at ~ 0 V as expected for the case for anion-immobilized solid electrolytes.³² The double-layer capacitance for solid-state electrochemical systems has been proven to be on a microfarad scale for oxygen-conducting electrolytes,³³ which is close to the case presented in Figure 4E. Based on the measured values of the double-layer capacitance, which are close to ~ 0.0 V, $C_{dl} = 1.2 \mu F/cm^2$, and taking into account the relative vacuum permittivity of $\epsilon_r = 1$ (i.e., a void), a double-layer thickness of ~ 0.7 nm or approximately 1.5 Li-ionic radii can be calculated. Theoretical approaches based on classical theory³¹ and low-frequency Monte-Carlo simulations³⁴ give similar double-layer thicknesses. The increase of C_{dl} with the bias potential can be interpreted through the formation of a more compact layer, as Li-ions compactly fill the voids toward the gold electrode, but a more detailed study of this phenomenon is yet to be conducted.

The leakage resistance in Figure 4F shows a strong, symmetric correlation to the applied bias potential, which indicates a variable electronic conductivity of the electrolyte. The leakage resistance also accounts for reactions at the electrodes (such as alloy formation) and therefore depends on the nature of the blocking electrodes (see Table S1). Values of the R_{LEAK} of several M Ω can be correlated to the high transference number found in solid electrolytes,³⁵ but the details related to the potential and temperature dependencies remain unclear and will be the focus of further studies.

The SCL capacitance (Figure 4G) and resistance (Figure 4H) strongly depend on the applied voltage. The former ranges from $C_{SCL,0V} = \sim 80 \mu F/cm^2$ to $C_{SCL,1V} = 6.42 \mu F/cm^2$, which indicates a widening of the SCL upon increasing the bias potential. The corresponding thickness of the SCL is estimated to be between $d_{SCL,0V} = \sim 7.4$ nm and $d_{SCL,1V} = \sim 59.5$ nm using the plate capacitor equation and the bulk dielectric constant $\epsilon_r = 677$. The SCL widens because the increasing number of depleted charges are held within a lattice that has a limited vacancy density. Once this concentration is reached, the additional electrical potential causes a perpendicular growth of the SCL into the electrolyte. While the SCL builds up on the positively biased side, the negatively biased side undergoes an accumulation of Li-ions. Because of the smaller number of vacancies, this AL is of much wider nature and therefore does not result in measurable capacitance. Thus, the impedance of the AL is not distinguishable from the spectra.

Notice that the calculated thickness of the SCL at zero bias does not go to zero. This has two prevailing reasons. One reason can arise from the accuracy of the measurement method

itself. Another reason is related to the nature of the electrodes, whose electrochemical potential force a redistribution of the ions near the interface at equilibrium.

Figure 4I shows a plot of the space charge capacitance commonly used in semiconductor physics, the so-called Mott–Schottky plot. While this type of analysis is typically used to characterize the SCLs formed at the semiconductor/electrolyte interface,³⁶ one can surprisingly observe an almost linear trend for the bias potentials above 0.5 V.

With the widening of the SCL, the corresponding resistance shown in Figure 4H increases to nonsymmetric maxima of $R_{-IV,SCL} = 5 \text{ k}\Omega$ and $R_{+IV,SCL} = 9 \text{ k}\Omega$ for negative and positive polarizations, respectively. The decrease of the absolute Li-ion concentration within the defect lattice causes the charge-transfer resistance to rise. A depletion of mobile charge carriers leading to a decrease in ion conductivity is observed in temperature variation as well.³⁷ For high bias potentials, the minimum lithium concentration is reached, and the resistance stabilizes at a fixed value, as can be observed in Figure 4H.

Figure 5 summarizes the obtained results and shows the charge layer structure near the positively biased gold electrode. The reasonably thick layer of 60 nm thickness causes a non-negligible resistance of $2580 \text{ M}\Omega \text{ cm}$. The double layer of 0.7 nm indicates a row of ionic charges right on the interface to the gold electrode, which is followed by the SCL.

CONCLUSIONS

A physical impedance model has been developed and validated for a variety of experimental conditions for the model Li-ion conductor. The SCL formation is elucidated by EIS measurements. The layer structure near the interface between the positive blocking Au electrode and LICGC glass electrolytes can be accurately described as consisting of a near-interface compact double layer, a diffuse but well-defined SCL, and the bulk electrolyte. An electric circuit model is proposed to interpret the observed capacitive and resistive behavior of the systems at different frequencies: each element of the model is found to be influenced differently by the experimental parameters, such as the material of the blocking electrode, the temperature, and the bias potential. As the SCLs are formed, a correlated resistance appears, which imposes a transport barrier for Li-ions from being transported through this highly charged layer. An SCL with a lower degree of depletion, that is at lower bias potentials, does not show this high resistance. Interface engineering, such as the introduction of stacked layers with different ionic conductivities could be used to mitigate this problem. The positively charged Li-ion accumulation on the other side of the electrolyte does not manifest itself in the impedance spectra under the conditions of this work due to its much larger width. The effective width of the double layer and SCL, the specific bulk and SCL ionic resistances, and the dielectric constant were calculated using the impedance data at different biases and temperatures. In further work, the space charge occurrence under constant current will be investigated, and the influence of temperature as an additional parameter should shed light on further details on the SCL formation in solid Li-conducting electrolytes.

ASSOCIATED CONTENT

Supporting Information

The Supporting Information is available free of charge at <https://pubs.acs.org/doi/10.1021/acsami.0c21304>.

Derivation of thermodynamic model and equivalent circuit parameters for each electrode metal (PDF)

AUTHOR INFORMATION

Corresponding Author

Aliaksandr S. Bandarenka – *Physik-Department ECS, Technische Universität München, 85748 Garching, Germany*; orcid.org/0000-0002-5970-4315; Phone: +49(0) 89289 12531; Email: bandarenka@ph.tum.de

Authors

Leon Katzenmeier – *Physik-Department ECS, Technische Universität München, 85748 Garching, Germany; Bayerisches Zentrum für Angewandte Energieforschung, 97074 Würzburg, Germany*

Simon Helmer – *Physik-Department ECS, Technische Universität München, 85748 Garching, Germany*

Stephan Braxmeier – *Bayerisches Zentrum für Angewandte Energieforschung, 97074 Würzburg, Germany*

Edwin Knobbe – *BMW Group, 80809 München, Germany*

Complete contact information is available at: <https://pubs.acs.org/doi/10.1021/acsami.0c21304>

Author Contributions

The manuscript was written through contributions of all authors. All authors have given approval to the final version of the manuscript.

Notes

The authors declare no competing financial interest.

ACKNOWLEDGMENTS

The authors would like to thank Regina Kluge for the AFM image. This work is part of the ASS Bayern project funded by the Bavarian Ministry of Economic Affairs, Regional Development and Energy. Additional financial support in the framework of Germany's Excellence Strategy—EXC 2089/1-390776260, cluster of excellence "e-conversion", is gratefully acknowledged.

REFERENCES

- Kim, J. G.; Son, B.; Mukherjee, S.; Schuppert, N.; Bates, A.; Kwon, O.; Choi, M. J.; Chung, H. Y.; Park, S. A Review of Lithium and non-Lithium Based Solid State Batteries. *J. Power Sources* **2015**, *282*, 299–322.
- Horowitz, Y.; Schmidt, C.; Yoon, D.-h.; Riegger, L. M.; Katzenmeier, L.; Bosch, G. M.; Noked, M.; Ein-Eli, Y.; Janek, J.; Zeier, W. G.; Diesendruck, C. E.; Golodnitsky, D. Between Liquid and All Solid: A Prospect on Electrolyte Future in Lithium-Ion Batteries for Electric Vehicles. *Energy Technol.* **2020**, *8*, 2000580.
- Porz, L.; Swamy, T.; Sheldon, B. W.; Rettenwander, D.; Frömling, T.; Thaman, H. L.; Berendts, S.; Uecker, R.; Carter, W. C.; Chiang, Y.-M. Mechanism of Lithium Metal Penetration through Inorganic Solid Electrolytes. *Adv. Energy Mater.* **2017**, *7*, 1701003.
- Jiang, F.; Peng, P. Elucidating the Performance Limitations of Lithium-Ion Batteries due to Species and Charge Transport through five Characteristic Parameters. *Sci. Rep.* **2016**, *6*, 32639.
- Nolan, A. M.; Zhu, Y.; He, X.; Bai, Q.; Mo, Y. Computation-Accelerated Design of Materials and Interfaces for All-Solid-State Lithium-Ion Batteries. *Joule* **2018**, *2*, 2016–2046.
- Shen, Y.; Zhang, Y.; Han, S.; Wang, J.; Peng, Z.; Chen, L. Unlocking the energy capabilities of Lithium Metal Electrode with Solid-State Electrolytes. *Joule* **2018**, *2*, 1674–1689.

- (7) Breuer, S.; Prutsch, D.; Ma, Q.; Epp, V.; Preishuber-Pflügl, F.; Tietz, F.; Wilkening, M. Separating Bulk from Grain Boundary Li-ion Conductivity in the sol-gel prepared Solid Electrolyte $\text{Li}_{1-x}\text{Al}_x\text{Ti}_{1-x}\text{(PO}_4)_3$. *J. Mater. Chem. A* **2015**, *3*, 21343–21350.
- (8) Waetzig, K.; Rost, A.; Heubner, C.; Coeler, M.; Nikolowski, K.; Wolter, M.; Schilm, J. Synthesis and sintering of $\text{Li}_{1-x}\text{Al}_x\text{Ti}_{1-x}\text{(PO}_4)_3$ (LATP) electrolyte for ceramics with improved Li⁺ conductivity. *J. Alloys Compd.* **2020**, *818*, 153237.
- (9) Tateyama, Y.; Gao, B.; Jalem, R.; Haruyama, J. Theoretical picture of positive electrode/solid electrolyte interface in all-solid-state battery from electrochemistry and semiconductor physics viewpoints. *Curr. Opin. Electrochem.* **2019**, *17*, 149–157.
- (10) Lim, H.-D.; Park, J.-H.; Shin, H.-J.; Jeong, J.; Kim, J. T.; Nam, K.-W.; Jung, H.-G.; Chung, K. Y. A review of challenges and issues concerning interfaces for all-solid-state batteries. *Energy Storage Mater.* **2020**, *25*, 224–250.
- (11) Bucci, G.; Talamini, B.; Renuka Balakrishna, A.; Chiang, Y.-M.; Carter, W. C. Mechanical instability of electrode-electrolyte interfaces in solid-state batteries. *Phys. Rev. Mater.* **2018**, *2*, 105407.
- (12) Wenzel, S.; Randau, S.; Leichtweiß, T.; Weber, D. A.; Sann, J.; Zeier, W. G.; Janek, J. Direct observation of the interfacial instability of the fast ionic conductor $\text{Li}_{10}\text{GeP}_2\text{S}_{12}$ at the lithium metal anode. *Chem. Mater.* **2016**, *28*, 2400–2407.
- (13) He, Y.; Lu, C.; Liu, S.; Zheng, W.; Luo, J. Interfacial Incompatibility and Internal Stresses in All-Solid-State Lithium Ion Batteries. *Adv. Energy Mater.* **2019**, *9*, 1901810.
- (14) Park, M.; Zhang, X.; Chung, M.; Less, G. B.; Sastry, A. M. A review of conduction phenomena in Li-ion batteries. *J. Power Sources* **2010**, *195*, 7904–7929.
- (15) Stegmaier, S.; Voss, J.; Reuter, K.; Luntz, A. C. Li⁺ Defects in a Solid-State Li Ion Battery: Theoretical Insights with a Li_3OCl Electrolyte. *Chem. Mater.* **2017**, *29*, 4330–4340.
- (16) de Klerk, N. J. J.; Wagemaker, M. Space charge Layers in All-Solid-State Batteries; Important or Negligible? *ACS Appl. Energy Mater.* **2018**, *1*, 5609–5618.
- (17) Masuda, H.; Ishida, N.; Ogata, Y.; Ito, D.; Fujita, D. Internal potential mapping of charged solid-state-lithium ion batteries using in situ Kelvin probe force microscopy. *Nanoscale* **2017**, *9*, 893–898.
- (18) Tsuchiya, B.; Ohnishi, J.; Sasaki, Y.; Yamamoto, T.; Yamamoto, Y.; Motoyama, M.; Iriyama, Y.; Morita, K. In Situ Direct Lithium Distribution Analysis Around Interfaces in an All-Solid-State Rechargeable Lithium Battery by Combined Ion-Beam Method. *Adv. Mater. Interfaces* **2019**, *6*, 1900100.
- (19) Braun, S.; Yada, C.; Latz, A. Thermodynamically Consistent Model for Space-Charge-Layer Formation in a Solid Electrolyte. *J. Phys. Chem. C* **2015**, *119*, 22281–22288.
- (20) Yamamoto, K.; Iriyama, Y.; Asaka, T.; Hirayama, T.; Fujita, H.; Fisher, C. A. J.; Nonaka, K.; Sugita, Y.; Ogumi, Z. Dynamic visualization of the electric potential in an all-solid-state rechargeable lithium battery. *Angew. Chem., Int. Ed.* **2010**, *49*, 4414–4417.
- (21) Hartmann, P.; Leichtweiss, T.; Busche, M. R.; Schneider, M.; Reich, M.; Sann, J.; Adelhelm, P.; Janek, J. Degradation of NASICON-type materials in contact with lithium metal: Formation of mixed conducting interphases (MCI) on solid electrolytes. *J. Phys. Chem. C* **2013**, *117*, 21064–21074.
- (22) Zangina, T.; Hassan, J.; Matori, K. A.; Azis, R. A. S.; Ahmadu, U.; See, A. Sintering behavior, ac conductivity and dielectric relaxation of $\text{Li}_{1.3}\text{Ti}_{1.7}\text{Al}_{0.3}\text{(PO}_4)_3$ NASICON compound. *Results Phys.* **2016**, *6*, 719–725.
- (23) Luo, W.; Gong, Y.; Zhu, Y.; Li, Y.; Yao, Y.; Zhang, Y.; Hu, L. Reducing Interfacial Resistance between Garnet-Structured Solid-State Electrolyte and Li-Metal Anode by a Germanium Layer. *Adv. Mater.* **2017**, *29*, 1606042.
- (24) Zhao, C.-Z.; Duan, H.; Huang, J.-Q.; Zhang, J.; Zhang, Q.; Guo, Y.-G.; Wan, L.-J. Designing solid-state interfaces on lithium-metal anodes: a review. *Sci. China: Chem.* **2019**, *62*, 1286–1299.
- (25) Lück, J.; Latz, A. The electrochemical double layer and its impedance behavior in lithium-ion batteries. *Phys. Chem. Chem. Phys.* **2019**, *21*, 14753–14765.
- (26) Ohara Glass Inc. Retrieved Aug 01, 2020, <https://www.oharacorp.com/lic-gc.html>.
- (27) Bandarenka, A. S. Development of hybrid algorithms for EIS data fitting, a book chapter. In *Lecture Notes on Impedance Spectroscopy. Measurement, Modeling and Applications*; Kanoun, O., Ed.; CRC Press, Taylor and Francis Group: London, 2013; Vol. 4, pp 29–36.
- (28) Braun, P.; Uhlmann, C.; Weber, A.; Störmer, H.; Gerthsen, D.; Ivers-Tiffée, E. Separation of the bulk and grain boundary contributions to the total conductivity of solid lithium-ion conducting electrolytes. *J. Electroceram.* **2017**, *38*, 157–167.
- (29) Kahlaoui, R.; Arbi, K.; Sobrados, I.; Jimenez, R.; Sanz, J.; Ternane, R. Cation Miscibility and Lithium Mobility in NASICON $\text{Li}_{1-x}\text{Ti}_{2-x}\text{Sc}_x\text{(PO}_4)_3$ ($0 \leq x \leq 0.5$) Series: A Combined NMR and Impedance Study. *Inorg. Chem.* **2017**, *56*, 1216–1224.
- (30) Hamam, K. J.; Salman, F. Dielectric constant and electrical study of solid-state electrolyte lithium phosphate glasses. *Appl. Phys. A* **2019**, *125*, 621.
- (31) Zangina, T.; Hassan, J.; Matori, K. A.; Azis, R. S.; Ndikilar, C. E.; Naning, F. H. Dielectric Relaxation Analysis of Chemical Solid Electrolyte Lithium Aluminum Titanium Phosphate. *Asian J. Appl. Sci.* **2017**, *11*, 46–55.
- (32) Armstrong, R. The double layer structure at the metal-solid electrolyte interface. *Solid State Ionics* **1997**, *94*, 181–187.
- (33) Chebotin, V. N.; Remez, I. D.; Solovieva, L. M.; Karpachev, S. V. Electrical double layer in solid electrolytes-theory: oxide electrolytes. *Electrochim. Acta* **1984**, *29*, 1380–1388.
- (34) Loth, M. S.; Skinner, B.; Shklovskii, B. I. Non-mean-field theory of anomalously large double layer capacitance. *Phys. Rev. E: Stat., Nonlinear, Soft Matter Phys.* **2010**, *82*, 016107–16.
- (35) Chen, L.; Li, W.; Fan, L. Z.; Nan, C. W.; Zhang, Q. Intercalated Electrolyte with High Transference Number for Dendrite-Free Solid-State Lithium Batteries. *Adv. Funct. Mater.* **2019**, *29*, 1901047.
- (36) Shockley, W. The Theory of p-n Junctions in Semiconductors and p-n Junction Transistors. *Bell Syst. Tech. J.* **1949**, *28*, 435–489.
- (37) Thokchom, J. S.; Kumar, B. The effects of crystallization parameters on the ionic conductivity of a lithium aluminum germanium phosphate glass-ceramic. *J. Power Sources* **2010**, *195*, 2870–2876.

10 Table of Figures.

FIGURE 1. SCHEMATIC OF THE DIFFERENT ION CONDUCTION PHENOMENA IN LIQUID, (SOLID) POLYMER, AND INORGANIC SOLID-STATE ELECTROLYTES. THE IONIC MOVEMENT IN POLYMERS HAPPENS WITHIN (I) OR BETWEEN (II) THE POLYMER CHAINS. IN SSEs, IONIC CONDUCTION OFTEN OCCURS VIA ION TRANSPORT ALONG CRYSTALLOGRAPHIC PATHWAYS. GRAPH ADAPTED FROM ENERGY TECHNOLOGY, 2020, 8(11), 2000580, THE AUTHORS. ENERGY TECHNOLOGY PUBLISHED BY WILEY-VCH GMBH.12

FIGURE 2. IDEALIZED CRYSTAL LATTICE WITH MOBILE AND IMMOBILE CATIONS, FILLED AND FREE VACANCIES, AND A FIXED ANION BACKGROUND. IN THIS EXAMPLE, THE NUMBER OF MOBILE AND IMMOBILE CATIONS IS EQUAL, AND THE NUMBER OF VACANCIES IS DOUBLE THE NUMBER OF CATIONS. ANY CATION ACCUMULATION OR DEPLETION IS THEREFORE LIMITED BY THE IMMOBILE CATION CONCENTRATION AND THE VACANCY CONCENTRATION.22

FIGURE 3. A) A GENERAL LOGISTIC FUNCTION FOR A REALISTIC SET OF PARAMETERS, WHICH CLOSELY RESEMBLES THE CHARGE CARRIER CONCENTRATION OF A SINGLE SCL SHOWN IN **B)**. STANDARD PARAMETERS FOR THE SIMULATIONS ARE $\Delta\phi = 4V$, $\lambda 2 = 1.5 \cdot 10^{-3}$. THE LOWER BOUNDARY FOR CHARGE CONCENTRATION IS GIVEN BY THE PARAMETER na , WHICH RESEMBLES THE ANION CONCENTRATION AND IS THE MAXIMUM CHARGE ACCUMULABLE BY DEPLETION OF IONS.....34

FIGURE 4. CHARGE CARRIER CONCENTRATION PROFILES IN THE DEPLETION LAYER **A)** AND ACCUMULATION LAYER **B)** FOR $\lambda = 1.5 \cdot 10^{-3}$, $\Delta\phi = 4V$, $na = 0.4$. THE EMPIRICAL FITS USING THE SIGMOID FUNCTION ARE THE DASHED LINES, WHICH SHOW VERY GOOD AGREEMENT WITH THE NUMERICAL SOLUTION TO THE PDE. IN BOTH THE ACCUMULATION AND DEPLETION LAYERS, THE EMPIRICAL FIT OVERESTIMATES THE NUMERICAL SOLUTION TO A SMALL DEGREE.36

FIGURE 5. EMPIRICAL PARAMETERS ARE DETERMINED BY FITTING THE EQUATION TO NUMERICAL SIMULATIONS. THE PARAMETERS $B1, B2$ ARE INVERSELY PROPORTIONAL TO λ , WHEREAS $v1, v2$ ARE CONSTANT FOR A WIDE RANGE OF $\lambda \in 1.5 \cdot 10^{-6}, 1.5 \cdot 10^{-2}$. NOTE THAT THE OUTLIERS PRESENT IN **B)** ARE DUE TO ERRORS IN THE NUMERICAL CALCULATIONS AND ARE NOT FILTERED OR REMOVED HERE FOR THE SAKE OF COMPLETENESS.....37

FIGURE 6. OVERVIEW OF AN EIS STUDY. THE IMPEDANCE SPECTRUM IS RECORDED BY PROBING THE ELECTROCHEMICAL SYSTEM WITH A PERTURBATION SIGNAL AND MEASURING THE RESPONSE. THE RESULTING IMPEDANCE SPECTRUM IS THEN FITTED USING A PHYSICAL MODEL IN THE FORM OF AN ELECTRICAL EQUIVALENT CIRCUIT TO EXTRACT SYSTEM PARAMETERS AND GAIN MECHANISTIC INSIGHTS. GRAPH ADAPTED FROM *PHYS. CHEM. CHEM. PHYS.*, 2021, 23, 12926, THE AUTHORS. *PHYSICAL CHEMISTRY CHEMICAL PHYSICS PUBLISHED BY ROYAL SOCIETY OF CHEMISTRY.*40

FIGURE 7. WORKING PRINCIPLE OF A PEIS WITH A SINUSOIDAL EXCITATION VOLTAGE (RED) AND THE SYSTEM RESPONSE IN THE FORM OF A SINUSOIDAL CURRENT (BLUE). IF THE ASSUMPTIONS OF A LINEAR AND STATIONARY RESPONSE ARE FULFILLED, THE RESPONSE FREQUENCY WILL MATCH THE EXCITATION FREQUENCY WITH A PHASE SHIFT ϕ BETWEEN THE CURVES. THE EXCITATION AMPLITUDE OF 10 mV IS A TYPICAL VALUE, AND THE AMPLITUDE RATIO GIVES THE ABSOLUTE VALUE OF THE IMPEDANCE.43

FIGURE 8. TYPICAL REPRESENTATIONS OF IMPEDANCE DATA, THE NYQUIST PLOT IN **A)** AND BODE PLOT IN **B)**. THE NYQUIST PLOT TYPICALLY REVEALS THE EXISTENCE OF FEATURES AND ELECTROCHEMICAL PROCESSES AT A FIRST GLANCE, BUT HIDES FREQUENCY INFORMATION. THE BODE PLOT, CONSISTING OF TWO PLOTS FOR THE ABSOLUTE VALUE OF THE IMPEDANCE AND THE PHASE SHIFT, CONTAINS FREQUENCY INFORMATION, BUT IS USUALLY HARDER TO INTERPRET. **C)** APPLIED VOLTAGE OVER TIME IN A STAIRCASE POTENTIOSTATIC EIS MEASUREMENT WITH THE WAITING TIME t_w AND VOLTAGE STEP SIZE V_s44

FIGURE 9. 2D SCHEMATIC OF AN EFFECTIVE MEDIUM APPROXIMATION, IN WHICH A SMALL FRACTION OF GUEST MATERIAL IS PRESENT IN A HOST MATERIAL. THE OPTICAL PROPERTIES OF THE COMPOSITE CAN BE CALCULATED BY THE EMA, WHEN THE FRACTION AND INDIVIDUAL PROPERTIES OF GUEST AND HOST ARE KNOWN.55

FIGURE 10. SCHEMATIC OF A THREE-LAYER STRUCTURE FOR THE MODELING OF THE OPTICAL RESPONSE. EACH INDIVIDUAL LAYER IS DESCRIBED BY THE REFRACTIVE INDICES $ni\lambda, ki\lambda$ AND THE THICKNESS di . IN ADDITION TO THE INDIVIDUAL COMPONENTS OF LAYERS 1-3, MIXED LAYERS AS DRAWN BETWEEN LAYERS 2 AND 3 OR INTERFACE ROUGHNESS AS INDICATED BETWEEN LAYERS 1 AND 2 CAN BE PRESENT AND INFLUENCE THE OVERALL OPTICAL RESPONSE.56

FIGURE 11. SCHEMATIC DRAWING OF AN ELLIPSOMETER SETUP WITH A LIGHT BEAM DIRECTION FROM LEFT TO RIGHT. A LINEARLY POLARIZED LIGHT BEAM IS PRODUCED BY THE POLARIZATION STATE GENERATOR (PSG) AND AFTER THE REFLECTION FROM THE SAMPLE SURFACE ANALYZED BY THE POLARIZATION STATE ANALYZER (PSA). GRAPH REPRODUCED FROM REFERENCE57

FIGURE 12. PHOTOGRAPH OF THE SAMPLE STAGE OF THE SPECTROSCOPIC ELLIPSOMETRY. RED AND BLUE CLAMPS AND CABLES ARE THE WORKING AND COUNTER ELECTRODE, RESPECTIVELY. THE SSE IS PLACED ON A COPPER SURFACE AND HELD BY AN AU SPRING, WHICH ALSO SERVES AS THE ELECTRICAL CONNECTION FOR THE COUNTER ELECTRODE. THE COPPER PLATE BENEATH THE SAMPLE IS THE

TEMPERATURE STAGE, ASSURING A FIXED TEMPERATURE THROUGHOUT THE MEASUREMENTS. THE OPTICAL LENS IN THE BACK IS THE DETECTOR. THE LIGHT BEAM ORIGINATES FROM THE LEFT OF THE PICTURE.	61
FIGURE 13. RELATIVE CHANGES IN SPECTROSCOPIC ANGLES UPON APPLICATION OF BIAS POTENTIAL. ALTHOUGH VARIATIONS ARE SMALL, COMPARED TO THE STATISTICAL ERROR OF 0.05%, A RELEVANT CHANGE OCCURS FOR ALL APPLIED BIAS POTENTIALS. <i>GRAPHS ADAPTED FROM ADV. MATER. 2021, 33, 2100585, © 2021 THE AUTHORS. ADVANCED MATERIALS PUBLISHED BY WILEY-VCH GMBH.</i>	64
FIGURE 14. DRAWING OF THE SAMPLE WITH THE DIFFERENT LAYERS OF MATERIALS AND THE IN SITU FORMED SCLs. THE MODELS FOR THE DIFFERENT MATERIALS AND LAYERS ARE LISTED ON THE RIGHT, WITH A LITERATURE MODEL FOR THE AU ELECTRODES, A 2ND ORDER CAUCHY MODEL FOR THE SSE, AND THE EMA MODEL FOR THE SCLs.	65
FIGURE 15. ANALYSIS OF THE BARE SSE. A) ELLIPSOMETRY SPECTRA RECORDED ON A PRISTINE SSE COMBINED WITH A FIT USING A CAUCHY MODEL. B) FITTED DISPERSION RELATION USING A SECOND-ORDER CAUCHY MODEL. <i>GRAPHS REPRODUCED FROM SUPPORTING INFORMATION OF ADV. MATER. 2021, 33, 2100585, © 2021 THE AUTHORS. ADVANCED MATERIALS PUBLISHED BY WILEY-VCH GMBH.</i>	66
FIGURE 16. SENSITIVITY OF THE DEVELOPED BRUGGEMAN MODEL TO THE CONCENTRATION CHANGE. THE CALCULATIONS ARE BASED ON -8 VOL% AND 3 VOL% LITHIUM, REPRESENTING SCL FOR -1 V AND 1 V, RESPECTIVELY. <i>GRAPHS REPRODUCED FROM SUPPORTING INFORMATION OF ADV. MATER. 2021, 33, 2100585, © 2021 THE AUTHORS. ADVANCED MATERIALS PUBLISHED BY WILEY-VCH GMBH.</i>	67
FIGURE 17. INFLUENCE OF THE BIAS POTENTIAL ON THE IMPEDANCE OF AN SSE IN BLOCKING CONDITIONS IN DIFFERENT FREQUENCY REGIONS. A) ALL FREQUENCIES, B) MID FREQUENCIES AND C) HIGH FREQUENCIES. THE IMPACT OF THE BIAS POTENTIAL IS LIMITED TO MID AND LOW FREQUENCIES, WHICH ARE GENERALLY ASSOCIATED WITH SLOWER PROCESSES SUCH AS CHARGE ACCUMULATION AT INTERFACES. THE LINES SHOW THE FITS OF THE EEC TO THE DATA, SHOWING VERY GOOD AGREEMENT OF THE FIT RESULTS. <i>GRAPHS REPRINTED WITH PERMISSION FROM 231. COPYRIGHT 2021 AMERICAN CHEMICAL SOCIETY.</i>	71
FIGURE 18. PHYSICAL EEC FOR THE SSE IN BLOCKING CONDITIONS. A CENTRAL RESISTANCE, R_{BULK} , ACCOUNTS FOR THE ELECTROLYTE RESISTANCE AND IS IN SERIES TO THE SCL ELEMENTS AND THE COMPACT DOUBLE LAYER (Z_{dl}). IN PARALLEL, A GEOMETRIC CAPACITANCE AND A LEAKAGE RESISTANCE REPRESENT THE SSE AS A DIELECTRIC WITH SMALL ELECTRONIC LEAKAGE.	72
FIGURE 19. IMPEDANCE SPECTRA RECORDED FOR A) - C) 10 DIFFERENT TEMPERATURES AND D) - F) THREE DIFFERENT ELECTRODE METALS, SHOWN IN THREE DIFFERENT REGIONS FROM LOW TO HIGH FREQUENCIES, FROM LEFT TO RIGHT, RESPECTIVELY. <i>REPRINTED WITH PERMISSION FROM 231. COPYRIGHT 2021 AMERICAN CHEMICAL SOCIETY.</i>	74
FIGURE 20. EEC PARAMETERS FOR BIAS POTENTIALS BETWEEN -1 V AND 1 V WERE RECORDED AT ROOM TEMPERATURE (25 °C) WITH AN AU ELECTRODE. THE PROPERTIES OF THE BULK, NAMELY R_{B} AND C_{GEOM} , SHOWN IN A) AND B) ARE INDEPENDENT OF THE APPLIED BIAS POTENTIAL. A SYMMETRICALLY INCREASING DOUBLE LAYER CAPACITANCE, SHOWN IN C) , INDICATES THE FORMATION OF A THIN DL WITH A DECREASING THICKNESS. THE ELECTRONIC LEAKAGE, D) , STRONGLY DEPENDS ON THE APPLIED POTENTIAL AND SEEMS TO BE “ACTIVATED” BY THE APPLICATION OF A POTENTIAL. E), F) SHOW THE PROPERTIES OF THE SCL WITH A DECREASE IN CAPACITANCE (INDICATING A GROWING LAYER) AND AN ASYMMETRIC INCREASE IN RESISTANCE. <i>ADAPTED WITH PERMISSION FROM 231. COPYRIGHT 2021 AMERICAN CHEMICAL SOCIETY.</i>	76
FIGURE 21. A) COMPARISON OF SCL THICKNESSES DETERMINED USING SPECTROSCOPIC ELLIPSOMETRY AND ELECTROCHEMICAL IMPEDANCE SPECTROSCOPY. ALTHOUGH BOTH ARE ON THE SAME ORDER OF MAGNITUDE AND THE GENERAL TREND IS SIMILAR, THE PLATEAU FORMATION FOR HIGH POTENTIALS ($> \pm 0.5$ V) IS ONLY OBSERVED IN SPECTROSCOPIC ELLIPSOMETRY DATA. B) CORRECTED RELATIVE DIELECTRIC CONSTANT CALCULATED BASED ON THE THICKNESS DETERMINED WITH SPECTROSCOPIC ELLIPSOMETRY AND CAPACITANCE FROM EIS ANALYSIS. <i>DATA ADAPTED WITH PERMISSION FROM REF 231. COPYRIGHT 2021 AMERICAN CHEMICAL SOCIETY. DATA ADAPTED FROM ADV. MATER. 2021, 33, 2100585, © 2021 THE AUTHORS. ADVANCED MATERIALS PUBLISHED BY WILEY-VCH GMBH.</i>	77
FIGURE 22. PARAMETERS OF THE EVALUATION OF IMPEDANCE DATA WITH THE EEC SHOWN IN FIGURE 18. THE TWO BULK PROPERTIES, R_{BULK} AND C_{GEOM} IN A) AND B) SHOW A POTENTIAL INDEPENDENT BEHAVIOR WITH AN INCREASE IN BULK RESISTANCE WITH TEMPERATURE AS EXPECTED. THE INCREASE IN GEOMETRIC CAPACITANCE IS DUE TO AN INCREASE IN PERMITTIVITY. THE SPACE CHARGE LAYER PROPERTIES C_{SCL} & R_{SCL} QUALITATIVELY MATCH THE ROOM TEMPERATURE DATA SHOWN BEFORE WITH DECREASES IN BOTH RESISTANCE AND CAPACITANCES. HOWEVER, THE ASYMMETRY OF THE RESISTANCES IS MORE PRONOUNCED FOR HIGHER TEMPERATURES. <i>GRAPHS ADAPTED WITH PERMISSION FROM REF 241. COPYRIGHT 2022 AMERICAN CHEMICAL SOCIETY.</i>	80

FIGURE 23. SCL THICKNESS PLOTTED OVER BIAS POTENTIAL, **A)**, AND THE SQUARE ROOT OF TEMPERATURE CALCULATED BASED ON THE MEASURED CAPACITANCES AND DIELECTRIC CONSTANTS, **B)**. A PLATEAU FORMATION CAN BE OBSERVED FOR HIGHER TEMPERATURES AT HIGHER ABSOLUTE POTENTIALS. THE PROPORTIONALITY SUGGESTED BY THE DEBYE THEORY BETWEEN SCREENING LENGTH AND TEMPERATURE IS CONFIRMED IN **B)** FOR NEGATIVE APPLIED POTENTIALS. *GRAPH ADAPTED WITH PERMISSION FROM REF 241. COPYRIGHT 2022 AMERICAN CHEMICAL SOCIETY.*82

FIGURE 24. **A)** ARRHENIUS BEHAVIOR OF THE CONDUCTIVITY OBSERVED IN SCLs FORMED AT THE SSE/AU INTERFACE FOR THREE DIFFERENT BIAS POTENTIALS. THE OVERALL CONDUCTIVITY IS LOWER AT HIGHER BIAS POTENTIALS. **B)** ACTIVATION ENERGY CALCULATED FROM THE SLOPE OF THE ARRHENIUS PLOT AND A COMPARISON TO THE BULK ACTIVATION ENERGY (DASHED LINE). *DATA ADAPTED WITH PERMISSION FROM REF 241. COPYRIGHT 2022 AMERICAN CHEMICAL SOCIETY.*83

FIGURE 25. **A)** FORMATION OF THE SCL REPRESENTED BY THE DECREASE IN MOBILE CATION CONCENTRATION AS A FUNCTION OF BIAS POTENTIAL (GREEN SHADES) AND TEMPERATURE (BLUE TO RED). **B)** THE INCREASED ACTIVATION ENERGY OF THE FORMED SCL COMPARED TO THE BULK SSE OF 22 MEV. *DATA ADAPTED WITH PERMISSION FROM REF 241. COPYRIGHT 2022 AMERICAN CHEMICAL SOCIETY.*85

FIGURE 26. NUMERICAL CALCULATIONS OF THE IMS EQUATION (EQUATION 48). STANDARD VALUES ARE $cLi^+ = 1 \text{ MOL/M}^3$, $c_{MAX} = 2 \text{ MOL/M}^3$, $\phi_{Bi} = 0 \text{ V}$, AND $T = 300 \text{ K}$. VARIATION OF cLi^+ AND c_{MAX} LEADS TO AN ASYMMETRIC CHANGE IN THE SLOPE, SHOWN IN **A)** AND **B)**. THE OFFSET ALONG THE X-AXIS WITH THE VARIATION OF V_{Bi} CAN BE OBSERVED IN **C)**. *GRAPHS ADAPTED/REPRODUCED WITH PERMISSION FROM REFERENCE 254.*88

FIGURE 27. **A)** ROOM TEMPERATURE SPEIS MEASUREMENT IN A MOTT-SCHOTTKY PLOT WITH A SLIGHT ASYMMETRY FOR NEGATIVE AND POSITIVE POTENTIALS. OVERALL, THE FIT OF THE IMS EQUATION IS CLOSER TO THE DATA FOR POSITIVE POTENTIALS. **B)** MOTT-SCHOTTKY PLOTS OF SPEIS DATA FOR DIFFERENT TEMPERATURES, SOLID LINES ARE THE FITS OF THE IMS EQUATION. WHILE THE SSE USED FOR THE MEASUREMENTS WAS THE SAME, THE SAMPLES WERE IN A DIFFERENT ELECTROCHEMICAL STATE, GIVING RISE TO THE OFFSET IN THE MINIMUM OF THE CURVES, I.E., ϕ_{bi} . *GRAPHS REPRODUCED WITH PERMISSION FROM REFERENCE 254.*90

FIGURE 28. RESULTS OF KMC SIMULATIONS WITH STANDARD PARAMETERS, SEE **TABLE 8.** **A)** Li^+ CONCENTRATION ACROSS THE SIMULATED DEVICE. A CHANGE IN LOCAL CHARGE CONCENTRATION BUILDS UP TOWARDS THE INTERFACE WITH A WIDER ACCUMULATION COMPARED TO THE DEPLETION. THE NET CHARGE IS DISPLACED AWAY FROM THE MORE POSITIVE ELECTRODE TO THE NEGATIVE ELECTRODE. THE POTENTIAL DISTRIBUTIONS IN **B)** ARE BASED ON THE BOUNDARY CONDITIONS $\phi z = 0 = \phi_{bias}$, $\phi z = L_s = 0$. THE POTENTIAL DROPS OCCUR ASYMMETRICALLY IN THE SCLs, WITH A HIGHER POTENTIAL DROP IN THE ACCUMULATION LAYER. THE BULK STAYS ELECTRONEUTRAL, AND THEREFORE NO POTENTIAL DROP OCCURS.93

FIGURE 29. IMPACT OF THE SAMPLE LENGTH ON THE SPATIAL EXTENT OF THE SCLs. SIMULATION PARAMETERS ARE GIVEN IN **TABLE 8.** IN **A)** THE INDEPENDENCE OF THE SCLs THICKNESS ON THE DEVICE LENGTH IS SHOWN WITH THE DASHED LINES SHOWING THE GEOMETRICAL END OF THE DEVICES FOR DIFFERENT LENGTHS. IN THE POTENTIAL DISTRIBUTIONS, SHOWN IN **B)**, A SLIGHT DEVIATION OF THE ELECTRONEUTRALITY OF THE BULK IS RECOGNIZABLE, WHICH APPEARS TO BE CONSTANT REGARDLESS OF THE SSE LENGTH.95

FIGURE 30. INFLUENCE OF PHYSICAL INPUT PARAMETERS ON THE FORMATION OF SCLs. STANDARD PARAMETERS ARE GIVEN IN **TABLE 8.** FOR POSITIVE BIAS POTENTIALS, THE DEPLETION LAYER THICKNESS IS SHOWN, WHEREAS, FOR NEGATIVE POTENTIALS, THE THICKNESSES ARE THOSE OF THE ACCUMULATION LAYERS. THE THICKNESSES ARE CALCULATED BASED ON THE 10% CRITERIUM AS DESCRIBED IN THE TEXT. THE SIMULATIONS IN ONE ROW ARE OF EQUAL CATION CONCENTRATION ($cLi^+ = 5 \cdot 10^{17}, 3 \cdot 10^{18}, 10^{19}$, FOR **A)-C)**, **D)-F)**, AND **G)-I)**, RESPECTIVELY. THE GREY INSERTS ARE THE VACANCY CONCENTRATIONS, WHICH ARE 1.25, 1.5, AND 2 TIMES THE CATION CONCENTRATION FROM LEFT TO RIGHT, RESPECTIVELY.96

FIGURE 31. OVERVIEW OF SCL RESEARCH WITH THE RELATIVELY SMALL NUMBER OF RESEARCH GROUPS, NAMED BY THE PI, WHICH INVESTIGATE SOME ASPECTS OF SCL FORMATION IN SSEs RANGING FROM THEORETICAL TO EXPERIMENTAL WORKS IN THE FIELDS OF PHYSICS AND ELECTROCHEMISTRY. THE NUMBERS INDICATE THE STUDIES AND FINDINGS OF THIS WORK ACCORDING TO THE LIST ON THE RIGHT.98

11 Literature.

- ¹ Global Energy Review 2020, iea. <https://www.iea.org/reports/global-energy-review-2020/renewables>, last accessed 2.03.2022.
- ² Bloomberg NEF (2021), Global Energy Storage Outlook. *Bloomberg New Energy Finance*, 5, 4-6.
- ³ Nayak, P. K., Yang, L., Brehm, W., & Adelhelm, P. (2018). From lithium-ion to sodium-ion batteries: advantages, challenges, and surprises. *Angewandte Chemie International Edition*, 57(1), 102-120.
- ⁴ Benato, R., Cosciani, N., Crugnola, G., Sessa, S. D., Lodi, G., Parmeggiani, C., & Todeschini, M. (2015). Sodium nickel chloride battery technology for large-scale stationary storage in the high voltage network. *Journal of Power Sources*, 293, 127-136.
- ⁵ Nathan, M. (2010). Microbattery technologies for miniaturized implantable medical devices. *Current pharmaceutical biotechnology*, 11(4), 404-410.
- ⁶ Saxena, S., Sanchez, G., & Pecht, M. (2017). Batteries in portable electronic devices: A user's perspective. *IEEE Industrial Electronics Magazine*, 11(2), 35-44.
- ⁷ Gröger, O., Gasteiger, H. A., & Suchsland, J. P. (2015). Electromobility: Batteries or fuel cells?. *Journal of The Electrochemical Society*, 162(14), A2605.
- ⁸ Kamat, P. V. (2019). Lithium-ion batteries and beyond: celebrating the 2019 Nobel Prize in chemistry—a virtual issue. *ACS Energy Letters*, 4(11), 2757-2759.
- ⁹ Asenbauer, J., Eisenmann, T., Kuenzel, M., Kazzazi, A., Chen, Z., & Bresser, D. (2020). The success story of graphite as a lithium-ion anode material—fundamentals, remaining challenges, and recent developments including silicon (oxide) composites. *Sustainable Energy & Fuels*, 4(11), 5387-5416.
- ¹⁰ Whittingham, M. S. (2014). Ultimate limits to intercalation reactions for lithium batteries. *Chemical reviews*, 114(23), 11414-11443.
- ¹¹ Goodenough, J. B. (2018). How we made the Li-ion rechargeable battery. *Nature Electronics*, 1(3), 204-204.
- ¹² Nitta, N., Wu, F., Lee, J. T., & Yushin, G. (2015). Li-ion battery materials: present and future. *Materials today*, 18(5), 252-264.
- ¹³ Albertus, P., Babinec, S., Litzelman, S., & Newman, A. (2018). Status and challenges in enabling the lithium metal electrode for high-energy and low-cost rechargeable batteries. *Nature Energy*, 3(1), 16-21.
- ¹⁴ Xu, W., Wang, J., Ding, F., Chen, X., Nasybulin, E., Zhang, Y., & Zhang, J. G. (2014). Lithium metal anodes for rechargeable batteries. *Energy & Environmental Science*, 7(2), 513-537.
- ¹⁵ Bieker, G., Winter, M., & Bieker, P. (2015). Electrochemical in situ investigations of SEI and dendrite formation on the lithium metal anode. *Physical Chemistry Chemical Physics*, 17(14), 8670-8679.

-
- ¹⁶ Kasemchainan, J., Zekoll, S., Jolly, D. S., Ning, Z., Hartley, G. O., Marrow, J., & Bruce, P. G. (2019). Critical stripping current leads to dendrite formation on plating in lithium anode solid electrolyte cells. *Nature materials*, 18(10), 1105-1111.
- ¹⁷ Mayers, M. Z., Kaminski, J. W., & Miller III, T. F. (2012). Suppression of dendrite formation via pulse charging in rechargeable lithium metal batteries. *The Journal of Physical Chemistry C*, 116(50), 26214-26221.
- ¹⁸ Crowther, O., & West, A. C. (2008). Effect of electrolyte composition on lithium dendrite growth. *Journal of the Electrochemical Society*, 155(11), A806.
- ¹⁹ Yang, H., Yin, L., Shi, H., He, K., Cheng, H. M., & Li, F. (2019). Suppressing lithium dendrite formation by slowing its desolvation kinetics. *Chemical Communications*, 55(88), 13211-13214.
- ²⁰ Takeda, Y., Yamamoto, O., & Imanishi, N. (2016). Lithium dendrite formation on a lithium metal anode from liquid, polymer and solid electrolytes. *Electrochemistry*, 84(4), 210-218.
- ²¹ Ji, X., Hou, S., Wang, P., He, X., Piao, N., Chen, J. & Wang, C. (2020). Solid-State Electrolyte Design for Lithium Dendrite Suppression. *Advanced Materials*, 32(46), 2002741.
- ²² Duan, H., Yin, Y. X., Shi, Y., Wang, P. F., Zhang, X. D., Yang, C. P. & Wan, L. J. (2018). Dendrite-free Li-metal battery enabled by a thin asymmetric solid electrolyte with engineered layers. *Journal of the American Chemical Society*, 140(1), 82-85.
- ²³ Möbius, H. H. (1997). On the history of solid electrolyte fuel cells. *Journal of solid-state electrochemistry*, 1(1), 2-16.
- ²⁴ Jaiswal, N., Tanwar, K., Suman, R., Kumar, D., Upadhyay, S., & Parkash, O. (2019). A brief review on ceria based solid electrolytes for solid oxide fuel cells. *Journal of Alloys and Compounds*, 781, 984-1005.
- ²⁵ Aono, H., Sugimoto, E., Sadaoka, Y., Imanaka, N., & Adachi, G. Y. (1990). Ionic conductivity of solid electrolytes based on lithium titanium phosphate. *Journal of the Electrochemical Society*, 137(4), 1023.
- ²⁶ Porz, L., Swamy, T., Sheldon, B. W., Rettenwander, D., Frömling, T., Thaman, H. L. & Chiang, Y. M. (2017). Mechanism of lithium metal penetration through inorganic solid electrolytes. *Advanced Energy Materials*, 7(20), 1701003.
- ²⁷ Yoshinari, T., Koerver, R., Hofmann, P., Uchimoto, Y., Zeier, W. G., & Janek, J. (2019). Interfacial stability of phosphate-NASICON solid electrolytes in Ni-rich NCM cathode-based solid-state batteries. *ACS Applied Materials & Interfaces*, 11(26), 23244-23253.
- ²⁸ Chen, R., Li, Q., Yu, X., Chen, L., & Li, H. (2019). Approaching practically accessible solid-state batteries: stability issues related to solid electrolytes and interfaces. *Chemical Reviews*, 120(14), 6820-6877.
- ²⁹ Riegger, L. M., Schlem, R., Sann, J., Zeier, W. G., & Janek, J. (2021). Lithium-Metal Anode Instability of the Superionic Halide Solid Electrolytes and the Implications for Solid-State Batteries. *Angewandte Chemie*, 133(12), 6792-6797.

-
- ³⁰ Wu, Z., Xie, Z., Yoshida, A., Wang, Z., Hao, X., Abudula, A., & Guan, G. (2019). Utmost limits of various solid electrolytes in all-solid-state lithium batteries: A critical review. *Renewable and Sustainable Energy Reviews*, 109, 367-385.
- ³¹ Horowitz, Y., Schmidt, C., Yoon, D. H., Riegger, L. M., Katzenmeier, L., Bosch, G. M. & Golodnitsky, D. (2020). Between Liquid and All Solid: A Prospect on Electrolyte Future in Lithium-Ion Batteries for Electric Vehicles. *Energy Technology*, 8(11), 2000580.
- ³² Kanno, R., & Murayama, M. (2001). Lithium ionic conductor thio-LISICON: the $\text{Li}_2\text{S}-\text{GeS}_2-\text{P}_2\text{S}_5$ system. *Journal of the Electrochemical Society*, 148(7), A742.
- ³³ Nagao, M., Imade, Y., Narisawa, H., Kobayashi, T., Watanabe, R., Yokoi, T., & Kanno, R. (2013). All-solid-state Li-sulfur batteries with mesoporous electrode and thio-LISICON solid electrolyte. *Journal of Power Sources*, 222, 237-242.
- ³⁴ Sakuda, A., Hayashi, A., & Tatsumisago, M. (2013). Sulfide solid electrolyte with favorable mechanical property for all-solid-state lithium battery. *Scientific Reports*, 3(1), 1-5.
- ³⁵ Takada, K., Ohta, N., Zhang, L., Xu, X., Hang, B. T., Ohnishi, T., & Sasaki, T. (2012). Interfacial phenomena in solid-state lithium battery with sulfide solid electrolyte. *Solid State Ionics*, 225, 594-597.
- ³⁶ Lau, J., DeBlock, R. H., Butts, D. M., Ashby, D. S., Choi, C. S., & Dunn, B. S. (2018). Sulfide solid electrolytes for lithium battery applications. *Advanced Energy Materials*, 8(27), 1800933.
- ³⁷ Han, F., Yue, J., Zhu, X., & Wang, C. (2018). Suppressing Li dendrite formation in $\text{Li}_2\text{S}-\text{P}_2\text{S}_5$ solid electrolyte by LiI incorporation. *Advanced Energy Materials*, 8(18), 1703644.
- ³⁸ Chen, T., Zhang, L., Zhang, Z., Li, P., Wang, H., Yu, C. & Xu, B. (2019). Argyrodite solid electrolyte with a stable interface and superior dendrite suppression capability realized by ZnO co-doping. *ACS Applied Materials & Interfaces*, 11(43), 40808-40816.
- ³⁹ Fan, L., Chen, S., Zhu, J., Ma, R., Li, S., Podila, R. & Lu, B. (2018). Simultaneous suppression of the dendrite formation and shuttle effect in a lithium-sulfur battery by bilateral solid electrolyte interface. *Advanced Science*, 5(9), 1700934.
- ⁴⁰ Gordon, R. S., Miller, G. R., McEntire, B. J., Beck, E. D., & Rasmussen, J. R. (1981). Fabrication and characterization of Nasicon electrolytes. *Solid State Ionics*, 3, 243-248.
- ⁴¹ Hou, M., Liang, F., Chen, K., Dai, Y., & Xue, D. (2020). Challenges and perspectives of NASICON-type solid electrolytes for all-solid-state lithium batteries. *Nanotechnology*, 31(13), 132003.
- ⁴² Ravaine, D. (1980). Glasses as solid electrolytes. *Journal of Non-Crystalline Solids*, 38, 353-358.
- ⁴³ Anantharamulu, N., Koteswara Rao, K., Rambabu, G., Vijaya Kumar, B., Radha, V., & Vithal, M. (2011). A wide-ranging review on Nasicon type materials. *Journal of Materials Science*, 46(9), 2821-2837.
- ⁴⁴ Wolfenstine, J., Allen, J. L., Sakamoto, J., Siegel, D. J., & Choe, H. (2018). Mechanical behavior of Li-ion-conducting crystalline oxide-based solid electrolytes: a brief review. *Ionic*, 24(5), 1271-1276.

-
- ⁴⁵ Bucci, G., Talamini, B., Balakrishna, A. R., Chiang, Y. M., & Carter, W. C. (2018). Mechanical instability of electrode-electrolyte interfaces in solid-state batteries. *Physical Review Materials*, 2(10), 105407.
- ⁴⁶ Shimonishi, Y., Zhang, T., Imanishi, N., Im, D., Lee, D. J., Hirano, A., & Sammes, N. (2011). A study on lithium/air secondary batteries—Stability of the NASICON-type lithium ion conducting solid electrolyte in alkaline aqueous solutions. *Journal of Power Sources*, 196(11), 5128-5132.
- ⁴⁷ Chen, S., Xie, D., Liu, G., Mwizerwa, J. P., Zhang, Q., Zhao, Y. & Yao, X. (2018). Sulfide solid electrolytes for all-solid-state lithium batteries: structure, conductivity, stability, and application. *Energy Storage Materials*, 14, 58-74.
- ⁴⁸ Chen, A. N., Qu, C., Shi, Y., & Shi, F. (2020). Manufacturing Strategies for Solid Electrolyte in Batteries. *Frontiers in Energy Research*, 8, 226.
- ⁴⁹ Xiao, Y., Turcheniuk, K., Narla, A., Song, A. Y., Ren, X., Magasinski, A. & Yushin, G. (2021). Electrolyte melt infiltration for scalable manufacturing of inorganic all-solid-state lithium-ion batteries. *Nature Materials*, 1-7.
- ⁵⁰ Koerver, R. (2018). Interface Phenomena and Chemo-Mechanical Effects in All-Solid-State Batteries. In Physikalisch-Chemisches Institut, Justus-Liebig-Universität Gießen. Dissertation
- ⁵¹ Koerver, R., Aygün, I., Leichtweiß, T., Dietrich, C., Zhang, W., Binder, J. O. & Janek, J. (2017). Capacity fade in solid-state batteries: interphase formation and chemomechanical processes in nickel-rich layered oxide cathodes and lithium thiophosphate solid electrolytes. *Chemistry of Materials*, 29(13), 5574-5582.
- ⁵² Walther, F., Koerver, R., Fuchs, T., Ohno, S., Sann, J., Rohnke, M. & Janek, J. (2019). Visualization of the interfacial decomposition of composite cathodes in argyrodite-based all-solid-state batteries using time-of-flight secondary-ion mass spectrometry. *Chemistry of Materials*, 31(10), 3745-3755.
- ⁵³ Luo, W., Gong, Y., Zhu, Y., Li, Y., Yao, Y., Zhang, Y. & Hu, L. (2017). Reducing interfacial resistance between garnet-structured solid-state electrolyte and Li-metal anode by a germanium layer. *Advanced Materials*, 29(22), 1606042.
- ⁵⁴ Haruyama, J., Sodeyama, K., Han, L., Takada, K., & Tateyama, Y. (2014). Space-charge layer effect at interface between oxide cathode and sulfide electrolyte in all-solid-state lithium-ion battery. *Chemistry of Materials*, 26(14), 4248-4255.
- ⁵⁵ Gittleson, F. S.; El Gabaly, F. (2017). Non-Faradaic Li⁺ Migration and Chemical Coordination across Solid-State Battery Interfaces. *Nano Letters*, 17, 6974–6982
- ⁵⁶ Maier, J. (1995). Ionic conduction in space charge regions. *Progress in Solid State Chemistry*, 23(3), 171-263.
- ⁵⁷ Sheldon, B. W., & Shenoy, V. B. (2011). Space charge induced surface stresses: implications in ceria and other ionic solids. *Physical Review Letters*, 106(21), 216104.
- ⁵⁸ Avila-Paredes, H. J., Choi, K., Chen, C. T., & Kim, S. (2009). Dopant-concentration dependence of grain-boundary conductivity in ceria: A space-charge analysis. *Journal of Materials Chemistry*, 19(27), 4837-4842.

-
- ⁵⁹ Gödickemeier, M., & Gauckler, L. J. (1998). Engineering of solid oxide fuel cells with ceria-based electrolytes. *Journal of the Electrochemical Society*, 145(2), 414.
- ⁶⁰ Bai, S., Sun, Y., Yi, J., He, Y., Qiao, Y., & Zhou, H. (2018). High-power Li-metal anode enabled by metal-organic framework modified electrolyte. *Joule*, 2(10), 2117-2132.
- ⁶¹ Lewis, J. A., Cortes, F. J. Q., Boebinger, M. G., Tippens, J., Marchese, T. S., Kondekar, N., Liu, X., Chi, M., & McDowell, M. T. (2019). Interphase Morphology between a Solid-State Electrolyte and Lithium Controls Cell Failure. *ACS Energy Letters*, 4(2), 591–599.
- ⁶² Hartmann, P., Leichtweiss, T., Busche, M. R., Schneider, M., Reich, M., Sann, J., Adelhelm, P., & Janek, J. (2013). Degradation of NASICON-type materials in contact with lithium metal: Formation of mixed conducting interphases (MCI) on solid electrolytes. *Journal of Physical Chemistry C*, 117(41), 21064–21074.
- ⁶³ Kornyshev, A. A., & Vorotyntsev, M. A. (1978). Aspects of conductivity and space charge phenomena in solid electrolytes. *Electrochimica Acta*, 23(3), 267-270.
- ⁶⁴ Kornyshev, A. A., & Vorotyntsev, M. A. (1981). Conductivity and space charge phenomena in solid electrolytes with one mobile charge carrier species, a review with original material. *Electrochimica Acta*, 26(3), 303-323.
- ⁶⁵ Maier, J. (1995). Ionic conduction in space charge regions. *Progress in Solid State Chemistry*, 23(3), 171–263.
- ⁶⁶ Mariappan, C. R., Heins, T. P., & Roling, B. (2010). Electrode polarization in glassy electrolytes: Large interfacial capacitance values and indication for pseudocapacitive charge storage. *Solid State Ionics*, 181(19-20), 859-863.
- ⁶⁷ Yamamoto, K., Iriyama, Y., Asaka, T., Hirayama, T., Fujita, H., Fisher, C. A. & Ogumi, Z. (2010). Dynamic visualization of the electric potential in an all-solid-state rechargeable lithium battery. *Angewandte Chemie International Edition*, 49(26), 4414-4417.
- ⁶⁸ Yamamoto, K., Iriyama, Y., Asaka, T., Hirayama, T., Fujita, H., Nonaka, K., Miyahara, K., Sugita, Y., & Ogumi, Z. (2012). Direct observation of lithium-ion movement around an in-situ-formed- negative-electrode/solid-state-electrolyte interface during initial charge-discharge reaction. *Electrochemistry Communications*, 20(1), 113–116.
- ⁶⁹ Haruyama, J., Sodeyama, K., Han, L., Takada, K., & Tateyama, Y. (2014). Space-charge layer effect at interface between oxide cathode and sulfide electrolyte in all-solid-state lithium-ion battery. *Chemistry of Materials*, 26(14), 4248–4255.
- ⁷⁰ Haruta, M., Shiraki, S., Suzuki, T., Kumatani, A., Ohsawa, T., Takagi, Y. & Hitosugi, T. (2015). Negligible “negative space-charge layer effects” at oxide-electrolyte/electrode interfaces of thin-film batteries. *Nano Letters*, 15(3), 1498-1502.
- ⁷¹ Bates, J. B., Dudney, N. J., Neudecker, B., Ueda, A., & Evans, C. D. (2000). Thin-film lithium and lithium-ion batteries. *Solid State Ionics*, 135(1-4), 33-45.
- ⁷² Ohta, N., Takada, K., Zhang, L., Ma, R., Osada, M., & Sasaki, T. (2006). Enhancement of the high-rate capability of solid-state lithium batteries by nanoscale interfacial modification. *Advanced Materials*, 18(17), 2226-2229.

-
- ⁷³ Cheng, Z., Liu, M., Ganapathy, S., Li, C., Li, Z., Zhang, X. & Wagemaker, M. (2020). Revealing the impact of space-charge layers on the Li-ion transport in all-solid-state batteries. *Joule*, 4(6), 1311-1323.
- ⁷⁴ Nomura, Y., Yamamoto, K., Hirayama, T., Ouchi, S., Igaki, E., & Saitoh, K. (2019). Direct Observation of a Li-Ionic Space-Charge Layer Formed at an Electrode/Solid-Electrolyte Interface. *Angewandte Chemie*, 131(16), 5346-5350.
- ⁷⁵ Yamamoto, K., Kawajiri, I., Tanji, T., Hibino, M., & Hirayama, T. (2000). High precision phase-shifting electron holography. *Microscopy*, 49(1), 31-39.
- ⁷⁶ Fuller, E. J., Strelcov, E., Weaver, J. L., Swift, M. W., Sugar, J. D., Kolmakov, A. & Talin, A. A. (2021). Spatially Resolved Potential and Li-Ion Distributions Reveal Performance-Limiting Regions in Solid-State Batteries. *ACS Energy Letters*, 6(11), 3944-3951.
- ⁷⁷ Braun, S., Yada, C., & Latz, A. (2015). Thermodynamically Consistent Model for Space-Charge-Layer Formation in a Solid Electrolyte. *Journal of Physical Chemistry C*, 119(39), 22281–22288.
- ⁷⁸ de Klerk, N. J., & Wagemaker, M. (2018). Space-charge layers in all-solid-state batteries; important or negligible?. *ACS Applied Energy Materials*, 1(10), 5609-5618.
- ⁷⁹ Landstorfer, M., Funken, S., & Jacob, T. (2011). An advanced model framework for solid electrolyte intercalation batteries. *Physical Chemistry Chemical Physics*, 13(28), 12817-12825.
- ⁸⁰ Helmholtz, H. V. (1853). Ueber einige Gesetze der Vertheilung elektrischer Ströme in körperlichen Leitern, mit Anwendung auf die thierisch-elektrischen Versuche (Schluss.). *Annalen der Physik*, 165(7), 353-377.
- ⁸¹ Urban, F., & White, H. L. (2002). Application of the double layer theory of Otto Stern. *The Journal of Physical Chemistry*, 36(12), 3157-3161.
- ⁸² Kirchner, K., Kirchner, T., Ivaništšev, V., & Fedorov, M. V. (2013). Electrical double layer in ionic liquids: Structural transitions from multilayer to monolayer structure at the interface. *Electrochimica Acta*, 110, 762-771.
- ⁸³ Yan, J. W., Tian, Z. Q., & Mao, B. W. (2017). Molecular-level understanding of electric double layer in ionic liquids. *Current Opinion in Electrochemistry*, 4(1), 105-111.
- ⁸⁴ Tenhaeff, W. E., Rangasamy, E., Wang, Y., Sokolov, A. P., Wolfenstine, J., Sakamoto, J., & Dudney, N. J. (2014). Resolving the Grain Boundary and Lattice Impedance of Hot-Pressed Li₇La₃Zr₂O₁₂ Garnet Electrolytes. *ChemElectroChem*, 1(2), 375–378.
- ⁸⁵ Kataoka, K., Nagata, H., & Akimoto, J. (2018). Lithium-ion conducting oxide single crystal as solid electrolyte for advanced lithium battery application. *Scientific Reports*, 8(1), 13–15.
- ⁸⁶ Bauerle, J. E. (1969). Study of solid electrolyte polarization by a complex admittance method. *Journal of Physics and Chemistry of Solids*, 30(12), 2657-2670.
- ⁸⁷ Goswami, N., & Kant, R. (2019). Theory for impedance response of grain and grain boundary in solid state electrolyte. *Journal of Electroanalytical Chemistry*, 835, 227–238.

-
- ⁸⁸ Breuer, S., Prutsch, D., Ma, Q., Epp, V., Preishuber-Pflügl, F., Tietz, F., & Wilkening, M. (2015). Separating bulk from grain boundary Li ion conductivity in the sol-gel prepared solid electrolyte $\text{Li}_{1.5}\text{Al}_{0.5}\text{Ti}_{1.5}(\text{PO}_4)_3$. *Journal of Materials Chemistry A*, 3(42), 21343–21350.
- ⁸⁹ Fleig, J. (2002). The grain boundary impedance of random microstructures: numerical simulations and implications for the analysis of experimental data. *Solid State Ionics*, 150(1-2), 181-193.
- ⁹⁰ Fleig, J., & Maier, J. (1998). A finite element study on the grain boundary impedance of different microstructures. *Journal of the Electrochemical Society*, 145(6), 2081.
- ⁹¹ Fleig, J. (2000). The influence of non-ideal microstructures on the analysis of grain boundary impedances. *Solid State Ionics*, 131(1-2), 117-127.
- ⁹² Fleig, J., & Maier, J. (1999). The impedance of ceramics with highly resistive grain boundaries: validity and limits of the brick layer model. *Journal of the European Ceramic Society*, 19(6-7), 693-696.
- ⁹³ Armstrong, R. D., & Burnham, R. A. (1976). The effect of roughness on the impedance of the interface between a solid electrolyte and a blocking electrode. *Journal of Electroanalytical Chemistry and Interfacial Electrochemistry*, 72(3), 257-266.
- ⁹⁴ Wang, J. C., & Bates, J. B. (1986). Model for the interfacial impedance between a solid electrolyte and a blocking metal electrode. *Solid State Ionics*, 18, 224-228.
- ⁹⁵ Armstrong, R. D., & Burnham, R. A. (1976). The effect of roughness on the impedance of the interface between a solid electrolyte and a blocking electrode. *Journal of Electroanalytical Chemistry and Interfacial Electrochemistry*, 72(3), 257-266.
- ⁹⁶ Karthikeyan, A., Vinatier, P., & Levasseur, A. (2000). Study of lithium glassy solid electrolyte/electrode interface by impedance analysis. *Bulletin of Materials Science*, 23(3), 179-183.
- ⁹⁷ John Albery, W., & Andrew, R. (1994). Dual transmission line with charge-transfer resistance for conducting polymers. *Journal of the Chemical Society, Faraday Transactions*, 90(8), 1115-1119.
- ⁹⁸ Ariyoshi, K., Tanimoto, M., & Yamada, Y. (2020). Impact of particle size of lithium manganese oxide on charge transfer resistance and contact resistance evaluated by electrochemical impedance analysis. *Electrochimica Acta*, 364, 137292.
- ⁹⁹ Swamy, T., & Chiang, Y. M. (2015). Electrochemical charge transfer reaction kinetics at the silicon-liquid electrolyte interface. *Journal of The Electrochemical Society*, 162(13), A7129.
- ¹⁰⁰ Yu, C., Ganapathy, S., Eck, E. R. H. V., Wang, H., Basak, S., Li, Z., & Wagemaker, M. (2017). Accessing the bottleneck in all-solid-state batteries, lithium-ion transport over the solid-electrolyte-electrode interface. *Nature Communications*, 8(1), 1–9.
- ¹⁰¹ Vardar, G., Bowman, W. J., Lu, Q., Wang, J., Chater, R. J., Aguadero, A. & Yildiz, B. (2018). Structure, chemistry, and charge transfer resistance of the interface between $\text{Li}_7\text{La}_3\text{Zr}_2\text{O}_{12}$ electrolyte and LiCoO_2 cathode. *Chemistry of Materials*, 30(18), 6259-6276.

-
- ¹⁰² Gellert, M., Gries, K. I., Sann, J., Pfeifer, E., Volz, K., & Roling, B. (2016). Impedance spectroscopic study of the charge transfer resistance at the interface between a LiNi_{0.5}Mn_{1.5}O₄ high-voltage cathode film and a LiNbO₃ coating film. *Solid State Ionics*, 287, 8-12.
- ¹⁰³ Sastre, J., Chen, X., Aribia, A., Tiwari, A. N., & Romanyuk, Y. E. (2020). Fast charge transfer across the Li₇La₃Zr₂O₁₂ solid electrolyte/LiCoO₂ cathode interface enabled by an interphase-engineered all-thin-film architecture. *ACS Applied Materials & Interfaces*, 12(32), 36196-36207.
- ¹⁰⁴ Krauskopf, T., Mogwitz, B., Hartmann, H., Singh, D. K., Zeier, W. G., & Janek, J. (2020). The Fast Charge Transfer Kinetics of the Lithium Metal Anode on the Garnet-Type Solid Electrolyte Li₆.₂₅Al_{0.25}La₃Zr₂O₁₂. *Advanced Energy Materials*, 10(27), 2000945.
- ¹⁰⁵ Basappa, R. H., Ito, T., & Yamada, H. (2017). Contact between garnet-type solid electrolyte and lithium metal anode: influence on charge transfer resistance and short circuit prevention. *Journal of The Electrochemical Society*, 164(4), A666.
- ¹⁰⁶ Yamada, T., Ito, S., Omoda, R., Watanabe, T., Aihara, Y., Agostini, M. & Scrosati, B. (2015). All solid-state lithium–sulfur battery using a glass-type P₂S₅–Li₂S electrolyte: benefits on anode kinetics. *Journal of The Electrochemical Society*, 162(4), A646.
- ¹⁰⁷ Alexander, G. V., Indu, M. S., Kamakshy, S., & Murugan, R. (2020). Development of stable and conductive interface between garnet structured solid electrolyte and lithium metal anode for high performance solid-state battery. *Electrochimica Acta*, 332, 135511.
- ¹⁰⁸ Zhang, L. K., Jing, M. X., Yang, H., Liu, Q. Y., Chen, F., Yuan, W. Y. & Shen, X. Q. (2020). Highly Efficient Interface Modification between Poly (Propylene Carbonate)-Based Solid Electrolytes and a Lithium Anode by Facile Graphite Coating. *ACS Sustainable Chemistry & Engineering*, 8(46), 17106-17115.
- ¹⁰⁹ Moradabadi, A., & Kaghazchi, P. (2019). Defect chemistry in cubic Li₆.₂₅Al_{0.25}La₃Zr₂O₁₂ solid electrolyte: A density functional theory study. *Solid State Ionics*, 338, 74-79.
- ¹¹⁰ Krauskopf, T., Mogwitz, B., Hartmann, H., Singh, D. K., Zeier, W. G., & Janek, J. (2020). The Fast Charge Transfer Kinetics of the Lithium Metal Anode on the Garnet-Type Solid Electrolyte Li₆.₂₅Al_{0.25}La₃Zr₂O₁₂. *Advanced Energy Materials*, 10(27), 2000945.
- ¹¹¹ Sata, N., Eberman, K., Eberl, K., & Maier, J. (2000). Mesoscopic fast ion conduction in nanometre-scale planar heterostructures. *Nature*, 408(6815), 946-949.
- ¹¹² Huggins, R. A. (2002). Simple method to determine electronic conductivity and ionic components of the conductors in mixed a review. *Ionics*, 8(3–4), 300–313.
- ¹¹³ Chen, Hao Min, Chen Maohua, & Stefan Adams (2015). Stability and ionic mobility in argyrodite-related lithium-ion solid electrolytes. *Physical Chemistry Chemical Physics*, 17.25, 16494-16506.
- ¹¹⁴ Peng, J., Xiao, Y., Clarkson, D. A., Greenbaum, S. G., Zawodzinski, T. A., & Chen, X. C. (2020). A Nuclear magnetic resonance study of cation and anion dynamics in polymer–ceramic composite solid electrolytes. *ACS Applied Polymer Materials*, 2(3), 1180-1189.

-
- ¹¹⁵ Tikekar, M. D., Archer, L. A., & Koch, D. L. (2016). Stabilizing electrodeposition in elastic solid electrolytes containing immobilized anions. *Science advances*, 2(7), 1600320.
- ¹¹⁶ Landstorfer, M., Funken, S., & Jacob, T. (2011). An advanced model framework for solid electrolyte intercalation batteries. *Physical Chemistry Chemical Physics*, 13(28), 12817-12825.
- ¹¹⁷ Shishvan, S. S., Fleck, N. A., & Deshpande, V. S. (2021). The initiation of void growth during stripping of Li electrodes in solid electrolyte cells. *Journal of Power Sources*, 488, 229437.
- ¹¹⁸ Kataoka, K., Nagata, H., & Akimoto, J. (2018). Lithium-ion conducting oxide single crystal as solid electrolyte for advanced lithium battery application. *Scientific Reports*, 8(1), 13–15.
- ¹¹⁹ Fujiwara, Y., Hoshikawa, K., & Kohama, K. (2016). Growth of solid electrolyte $\text{Li}_x\text{La}_{(1-x)/3}\text{NbO}_3$ single crystals by the directional solidification method. *Journal of Crystal Growth*, 433, 48-53.
- ¹²⁰ Dawson, J. A., Canepa, P., Famprikis, T., Masquelier, C., & Islam, M. S. (2018). Atomic-scale influence of grain boundaries on Li-ion conduction in solid electrolytes for all-solid-state batteries. *Journal of the American Chemical Society*, 140(1), 362-368.
- ¹²¹ Hori, S., Kato, M., Suzuki, K., Hirayama, M., Kato, Y., & Kanno, R. (2015). Phase Diagram of the Li_4GeS_4 - Li_3PS_4 Quasi-Binary System Containing the Superionic Conductor $\text{Li}_{10}\text{GeP}_2\text{S}_{12}$. *Journal of the American Ceramic Society*, 98(10), 3352–3360.
- ¹²² Tenhaeff, W. E., Rangasamy, E., Wang, Y., Sokolov, A. P., Wolfenstine, J., Sakamoto, J., & Dudney, N. J. (2014). Resolving the Grain Boundary and Lattice Impedance of Hot-Pressed $\text{Li}_7\text{La}_3\text{Zr}_2\text{O}_{12}$ Garnet Electrolytes. *ChemElectroChem*, 1(2), 375–378.
- ¹²³ Andreas Mandelis. Theory of space-charge layer dynamics at oxide- semiconductor interfaces under optical modulation and detection by laser photo-carrier radiometry. *Journal of Applied Physics*, 97(8), 2005.
- ¹²⁴ Manuel Landstorfer, Stefan Funken, and Timo Jacob. An advanced model framework for solid electrolyte intercalation batteries. *Physical Chemistry Chemical Physics*, 13(28):12817–12825, 2011.
- ¹²⁵ Zendejas, M. A., & Thomas, J. O. (1990). Conduction mechanisms in solid electrolytes: Na^+ beta-alumina. *Physica Scripta*, 1990(T33), 235.
- ¹²⁶ Zhao, C. Z., Zhang, X. Q., Cheng, X. B., Zhang, R., Xu, R., Chen, P. Y. & Zhang, Q. (2017). An anion-immobilized composite electrolyte for dendrite-free lithium metal anodes. *Proceedings of the National Academy of Sciences*, 114(42), 11069-11074.
- ¹²⁷ Wu, N., Chien, P. H., Li, Y., Dolocan, A., Xu, H., Xu, B. & Goodenough, J. B. (2020). Fast Li^+ conduction mechanism and interfacial chemistry of a NASICON/polymer composite electrolyte. *Journal of the American Chemical Society*, 142(5), 2497-2505.
- ¹²⁸ Kittel, C., McEuen, P., & McEuen, P. (1996). Introduction to solid state physics (Vol. 8, pp. 105-130). *New York: Wiley*.

-
- ¹²⁹ Weinert, U., & Mason, E. A. (1980). Generalized nernst-einstein relations for nonlinear transport coefficients. *Physical Review A*, 21(2), 681.
- ¹³⁰ Dreyer, W., Guhlke, C., & Müller, R. (2013). Overcoming the shortcomings of the Nernst-Planck model. *Physical Chemistry Chemical Physics*, 15(19), 7075–7086.
- ¹³¹ Yochelis, A. (2014). Spatial structure of electrical diffuse layers in highly concentrated electrolytes: A modified poisson-nernst-planck approach. *Journal of Physical Chemistry C*, 118(11), 5716–5724.
- ¹³² Liu, Y., Ma, Y. B., Jaegermann, W., Hausbrand, R., & Xu, B. X. (2020). Interface equilibrium modeling of all-solid-state lithium-ion thin film batteries. *Journal of Power Sources*, 454, 227892.
- ¹³³ Wang, H., & Pilon, L. (2011). Accurate simulations of electric double layer capacitance of ultramicroelectrodes. *The Journal of Physical Chemistry C*, 115(33), 16711–16719.
- ¹³⁴ Famprikis, T., Canepa, P., Dawson, J. A., Islam, M. S., & Masquelier, C. (2019). Fundamentals of inorganic solid-state electrolytes for batteries. *Nature materials*, 18(12), 1278–1291.
- ¹³⁵ Balkanski, M., & Wallis, R. F. (2000). Semiconductor physics and applications (Vol. 8). *Oxford university press*.
- ¹³⁶ Ohno, T. R., Chen, Y., Harvey, S. E., Kroll, G. H., Weaver, J. H., Haufler, R. E., & Smalley, R. E. (1991). C 60 bonding and energy-level alignment on metal and semiconductor surfaces. *Physical Review B*, 44(24), 13747.
- ¹³⁷ Semiconductor Junction, Chapter 8, in Lecture Notes on Solar Energy. Open Course Ware, TU Delft, The Netherlands. Retrieved 12. Nov 2021
- ¹³⁸ Böer, K. W. (2010). Introduction to space charge effects in semiconductors (Vol. 37). *Berlin: Springer*.
- ¹³⁹ Albery, W. J., O'Shea, G. J., & Smith, A. L. (1996). Interpretation and use of Mott–Schottky plots at the semiconductor/electrolyte interface. *Journal of the Chemical Society, Faraday Transactions*, 92(20), 4083–4085.
- ¹⁴⁰ Kontogeorgis, G. M., Maribo-Mogensen, B., & Thomsen, K. (2018). The Debye-Hückel theory and its importance in modeling electrolyte solutions. *Fluid Phase Equilibria*, 462, 130–152.
- ¹⁴¹ Liu, J. L., & Li, C. L. (2019). A generalized Debye-Hückel theory of electrolyte solutions. *AIP Advances*, 9(1), 015214.
- ¹⁴² Tadmor, R., Hernández-Zapata, E., Chen, N., Pincus, P., & Israelachvili, J. N. (2002). Debye length and double-layer forces in polyelectrolyte solutions. *Macromolecules*, 35(6), 2380–2388.
- ¹⁴³ Smith, A. M., Lee, A. A., & Perkin, S. (2016). The electrostatic screening length in concentrated electrolytes increases with concentration. *The Journal of Physical Chemistry Letters*, 7(12), 2157–2163.
- ¹⁴⁴ Frensley, W. R., & Kroemer, H. (1977). Theory of the energy-band lineup at an abrupt semiconductor heterojunction. *Physical Review B*, 16(6), 2642.
- ¹⁴⁵ Wolfgang Dreyer, Clemens Guhlke, and Rüdiger Müller. Overcoming the short-comings of the Nernst-Planck model. *Physical Chemistry Chemical Physics*, 15(19):7075–7086, 2013.

-
- ¹⁴⁶ Yin, X., Goudriaan, J. A. N., Lantinga, E. A., Vos, J. A. N., & Spiertz, H. J. (2003). A flexible sigmoid function of determinate growth. *Annals of botany*, *91*(3), 361-371.
- ¹⁴⁷ Ezeafulukwe, U. A., Darus, M., & Fadipe-Joseph, O. (2018). On analytic properties of a sigmoid function. *Int. Journal of Mathematics and Computer Science*, *13*(2), 171-178.
- ¹⁴⁸ Sellers, M. C., & Seebauer, E. G. (2011). Measurement method for carrier concentration in TiO₂ via the Mott-Schottky approach. *Thin Solid Films*, *519*(7), 2103-2110.
- ¹⁴⁹ Cardon, F., & Gomes, W. P. (1978). On the determination of the flat-band potential of a semiconductor in contact with a metal or an electrolyte from the Mott-Schottky plot. *Journal of Physics D: Applied Physics*, *11*(4), L63.
- ¹⁵⁰ Gelderman, K., Lee, L., & Donne, S. W. (2007). Flat-band potential of a semiconductor: using the Mott-Schottky equation. *Journal of chemical education*, *84*(4), 685.
- ¹⁵¹ Grundmann, M. (2010). Physics of semiconductors (Vol. 11, pp. 401-472). Berlin. *Springer*.
- ¹⁵² Orazem, M. E., & Tribollet, B. (2008). Electrochemical impedance spectroscopy. *New Jersey*.
- ¹⁵³ Lvovich, V. F. (2012). Impedance spectroscopy: applications to electrochemical and dielectric phenomena. *John Wiley & Sons*.
- ¹⁵⁴ Macdonald, J. R. (2005). Impedance spectroscopy: Models, data fitting, and analysis. *Solid state ionics*, *176*(25-28), 1961-1969.
- ¹⁵⁵ Lasia, A. (2002). Electrochemical impedance spectroscopy and its applications. In *Modern aspects of electrochemistry* (pp. 143-248). Springer, Boston, MA.
- ¹⁵⁶ Middlemiss, L. A., Rennie, A. J., Sayers, R., & West, A. R. (2020). Characterisation of batteries by electrochemical impedance spectroscopy. *Energy Reports*, *6*, 232-241.
- ¹⁵⁷ Song, J. Y., Lee, H. H., Wang, Y. Y., & Wan, C. C. (2002). Two-and three-electrode impedance spectroscopy of lithium-ion batteries. *Journal of Power Sources*, *111*(2), 255-267.
- ¹⁵⁸ Cho, H. M., Park, Y. J., Yeon, J. W., & Shin, H. C. (2009). In-depth investigation on two-and three-electrode impedance measurements in terms of the effect of the counter electrode. *Electronic Materials Letters*, *5*(4), 169-178.
- ¹⁵⁹ Schiller, C. A., Richter, F., Gülzow, E., & Wagner, N. (2001). Validation and evaluation of electrochemical impedance spectra of systems with states that change with time. *Physical Chemistry Chemical Physics*, *3*(3), 374-378.
- ¹⁶⁰ Kaisare, N. S., Ramani, V., Pushpavanam, K., & Ramanathan, S. (2011). An analysis of drifts and nonlinearities in electrochemical impedance spectra. *Electrochimica acta*, *56*(22), 7467-7475.
- ¹⁶¹ Van Gheem, E., Pintelon, R., Vereecken, J., Schoukens, J., Hubin, A., Verboven, P., & Blajiev, O. (2004). Electrochemical impedance spectroscopy in the presence of non-linear distortions and non-stationary behaviour: Part I: Theory and validation. *Electrochimica Acta*, *49*(26), 4753-4762.

-
- ¹⁶² Szekeres, K. J., Vesztergom, S., Ujvári, M., & Láng, G. G. (2021). Methods for the Determination of Valid Impedance Spectra in Non-stationary Electrochemical Systems: Concepts and Techniques of Practical Importance. *ChemElectroChem*, *8*(7), 1233-1250.
- ¹⁶³ Zhang, S. S., Xu, K., & Jow, T. R. (2004). Electrochemical impedance study on the low temperature of Li-ion batteries. *Electrochimica acta*, *49*(7), 1057-1061.
- ¹⁶⁴ Huang, J., & Tong, B. (2017). Probing the reaction interface in Li-O₂ batteries using electrochemical impedance spectroscopy: dual roles of Li₂O₂. *Chemical Communications*, *53*(83), 11418-11421.
- ¹⁶⁵ Giner-Sanz, J. J., Ortega, E. M., & Pérez-Herranz, V. (2016). Harmonic analysis based method for linearity assessment and noise quantification in electrochemical impedance spectroscopy measurements: Theoretical formulation and experimental validation for Tafelian systems. *Electrochimica Acta*, *211*, 1076-1091.
- ¹⁶⁶ Carcione, J. M., Cavallini, F., Ba, J., Cheng, W., & Qadrouh, A. N. (2019). On the kramers-kronig relations. *Rheologica Acta*, *58*(1), 21-28.
- ¹⁶⁷ Orazem, M. E., Esteban, J. M., & Moghissi, O. C. (1991). Practical applications of the Kramers-Kronig relations. *Corrosion*, *47*(4), 248-259.
- ¹⁶⁸ Esteban, J. M., & Orazem, M. E. (1991). On the application of the Kramers-Kronig relations to evaluate the consistency of electrochemical impedance data. *Journal of the Electrochemical Society*, *138*(1), 67.
- ¹⁶⁹ Agarwal, P., Orazem, M. E., & Garcia-Rubio, L. H. (1995). Application of Measurement Models to Impedance Spectroscopy: III. Evaluation of Consistency with the Kramers-Kronig Relations. *Journal of the Electrochemical Society*, *142*(12), 4159.
- ¹⁷⁰ Kadan-Jamal, K., Sophocleous, M., Jog, A., Desagani, D., Teig-Sussholz, O., Georgiou, J. & Shacham-Diamand, Y. (2020). Electrical Impedance Spectroscopy of plant cells in aqueous biological buffer solutions and their modelling using a unified electrical equivalent circuit over a wide frequency range: 4Hz to 20 GHz. *Biosensors and Bioelectronics*, *168*, 112485.
- ¹⁷¹ Elvin, N. G., & Elvin, A. A. (2009). A general equivalent circuit model for piezoelectric generators. *Journal of Intelligent Material Systems and Structures*, *20*(1), 3-9.
- ¹⁷² Tamrakar, V., Gupta, S. C., & Sawle, Y. (2015, October). Study of characteristics of single and double diode electrical equivalent circuit models of solar PV module. In *2015 International Conference on Energy Systems and Applications* (pp. 312-317).
- ¹⁷³ Wang, Z., Zhao, T., Yao, J., Kishikawa, Y., & Takei, M. (2016). Evaluation of the electrochemical characterizations of lithium-ion battery (LIB) slurry with 10-parameter electrical equivalent circuit (EEC). *Journal of The Electrochemical Society*, *164*(2), A8.
- ¹⁷⁴ Liaw, B. Y., Nagasubramanian, G., Jungst, R. G., & Doughty, D. H. (2004). Modeling of lithium ion cells—A simple equivalent-circuit model approach. *Solid State Ionics*, *175*(1-4), 835-839.
- ¹⁷⁵ Zhang, X., Lu, J., Yuan, S., Yang, J., & Zhou, X. (2017). A novel method for identification of lithium-ion battery equivalent circuit model parameters considering electrochemical properties. *Journal of Power Sources*, *345*, 21-29.

-
- ¹⁷⁶ Brandstätter, H., Hanzu, I., & Wilkening, M. (2016). Myth and reality about the origin of inductive loops in impedance spectra of lithium-ion electrodes—a critical experimental approach. *Electrochimica Acta*, *207*, 218-223.
- ¹⁷⁷ Battistel, A., Fan, M., Stojadinović, J., & La Mantia, F. (2014). Analysis and mitigation of the artefacts in electrochemical impedance spectroscopy due to three-electrode geometry. *Electrochimica Acta*, *135*, 133-138.
- ¹⁷⁸ Orazem, M. E., Frateur, I., Tribollet, B., Vivier, V., Marcelin, S., Pébère, N. & Musiani, M. (2013). Dielectric properties of materials showing constant-phase-element (CPE) impedance response. *Journal of The Electrochemical Society*, *160*(6), C215.
- ¹⁷⁹ Jorcin, J. B., Orazem, M. E., Pébère, N., & Tribollet, B. (2006). CPE analysis by local electrochemical impedance spectroscopy. *Electrochimica Acta*, *51*(8-9), 1473-1479.
- ¹⁸⁰ Córdoba-Torres, P., Mesquita, T. J., & Nogueira, R. P. (2015). Relationship between the origin of constant-phase element behavior in electrochemical impedance spectroscopy and electrode surface structure. *The Journal of Physical Chemistry C*, *119*(8), 4136-4147.
- ¹⁸¹ Song, H. K., Jung, Y. H., Lee, K. H., & Dao, L. H. (1999). Electrochemical impedance spectroscopy of porous electrodes: the effect of pore size distribution. *Electrochimica Acta*, *44*(20), 3513-3519.
- ¹⁸² Niya, S. M. R., & Hoorfar, M. (2016). On a possible physical origin of the constant phase element. *Electrochimica Acta*, *188*, 98-102.
- ¹⁸³ Kim, C. H., Pyun, S. I., & Kim, J. H. (2003). An investigation of the capacitance dispersion on the fractal carbon electrode with edge and basal orientations. *Electrochimica Acta*, *48*(23), 3455-3463.
- ¹⁸⁴ Yezer, B. A., Khair, A. S., Sides, P. J., & Prieve, D. C. (2015). Use of electrochemical impedance spectroscopy to determine double-layer capacitance in doped nonpolar liquids. *Journal of colloid and interface science*, *449*, 2-12.
- ¹⁸⁵ Pajkossy, T. (2005). Impedance spectroscopy at interfaces of metals and aqueous solutions—Surface roughness, CPE and related issues. *Solid State Ionics*, *176*(25-28), 1997-2003.
- ¹⁸⁶ Zoltowski, P. (1998). On the electrical capacitance of interfaces exhibiting constant phase element behaviour. *Journal of Electroanalytical Chemistry*, *443*(1), 149-154.
- ¹⁸⁷ Muralidharan, V. S. (1997). Warburg impedance-basics revisited. *Anti-Corrosion Methods and Materials*.
- ¹⁸⁸ Gaddam, R. R., Katzenmeier, L., Lamprecht, X., & Bandarenka, A. S. (2021). Review on physical impedance models in modern battery research. *Physical Chemistry Chemical Physics*, *23*(23), 12926–12944.
- ¹⁸⁹ Gavriluk, A. L., Osinkin, D. A., & Bronin, D. I. (2017). The use of Tikhonov regularization method for calculating the distribution function of relaxation times in impedance spectroscopy. *Russian Journal of Electrochemistry*, *53*(6), 575-588.
- ¹⁹⁰ Schlüter, N., Ernst, S., & Schröder, U. (2020). Direct access to the optimal regularization parameter in distribution of relaxation times analysis. *ChemElectroChem*, *7*(16), 3445-3458.

-
- ¹⁹¹ Schmidt, J. P., Berg, P., Schönleber, M., Weber, A., & Ivers-Tiffée, E. (2013). The distribution of relaxation times as basis for generalized time-domain models for Li-ion batteries. *Journal of Power Sources*, 221, 70-77.
- ¹⁹² Zhu, J., Knapp, M., Liu, X., Yan, P., Dai, H., Wei, X., & Ehrenberg, H. (2020). Low-Temperature Separating Lithium-Ion Battery Interfacial Polarization Based on Distribution of Relaxation Times (DRT) of Impedance. *IEEE Transactions on Transportation Electrification*, 7(2), 410-421.
- ¹⁹³ Guo, D., Yang, G., Zhao, G., Yi, M., Feng, X., Han, X., & Ouyang, M. (2020). Determination of the Differential Capacity of Lithium-Ion Batteries by the Deconvolution of Electrochemical Impedance Spectra. *Energies*, 13(4), 915.
- ¹⁹⁴ Boukamp, B. A. (2004). Electrochemical impedance spectroscopy in solid state ionics: recent advances. *Solid State Ionics*, 169(1-4), 65-73.
- ¹⁹⁵ Boukamp, B. A., & Rolle, A. (2017). Analysis and application of distribution of relaxation times in solid state ionics. *Solid State Ionics*, 302, 12-18.
- ¹⁹⁶ Orazem, M. E., & Tribollet, B. (2008). Electrochemical impedance spectroscopy. *New Jersey*, 383-389.
- ¹⁹⁷ Huard, S. (1997). *Polarization of light* (p. 348). ISBN 0-471-96536-7. Wiley-VCH.
- ¹⁹⁸ Stone, J. A., & Stejskal, A. (2004). Using helium as a standard of refractive index: correcting errors in a gas refractometer. *Metrologia*, 41(3), 189.
- ¹⁹⁹ Sobral, H., & Peña-Gomar, M. (2015). Determination of the refractive index of glucose-ethanol-water mixtures using spectroscopic refractometry near the critical angle. *Applied Optics*, 54(28), 8453-8458.
- ²⁰⁰ Herrmann, P. P. (1980). Determination of thickness, refractive index, and dispersion of waveguiding thin films with an Abbe refractometer. *Applied Optics*, 19(19), 3261-3262.
- ²⁰¹ <https://refractiveindex.info>, last accessed on 10.02.2022.
- ²⁰² <https://www.filmetrics.com/refractive-index-database>, last accessed on 10.02.2022,
- ²⁰³ Niklasson, G. A., Granqvist, C. G., & Hunderi, O. (1981). Effective medium models for the optical properties of inhomogeneous materials. *Applied Optics*, 20(1), 26-30.
- ²⁰⁴ Khardani, M., Bouaïcha, M., & Bessaïs, B. (2007). Bruggeman effective medium approach for modelling optical properties of porous silicon: comparison with experiment. *Physica Status Solidi C*, 4(6), 1986-1990.
- ²⁰⁵ Feldman, A. (1988, February). Modeling refractive index in mixed component systems. In *Modeling of Optical Thin Films* (Vol. 821, pp. 129-132). International Society for Optics and Photonics.
- ²⁰⁶ Fried, M., Lohner, T., Jároli, E., Vizkelethy, G., Mezey, G., Gyulai, J. & Kerkow, H. (1984). Investigation of ion-implanted semiconductors by ellipsometry and backscattering spectrometry. *Thin Solid Films*, 116(1-3), 191-198.
- ²⁰⁷ Erman, M., Theeten, J. B., Chambon, P., Kelso, S. M., & Aspnes, D. E. (1984). Optical properties and damage analysis of GaAs single crystals partly amorphized by ion implantation. *Journal of Applied Physics*, 56(10), 2664-2671.

-
- ²⁰⁸ Adachi, S., Matsumura, T., & Suzuki, T. (1994). Optical Properties of Ion-Implanted Si layers Studied by Spectroscopic Ellipsometry. *Japanese Journal of Applied Physics*, 33(4R), 1931.
- ²⁰⁹ Gao, L., & Li, Z. (2003). Effective medium approximation for two-component nonlinear composites with shape distribution. *Journal of physics: Condensed Matter*, 15(25), 4397.
- ²¹⁰ Humlicek, J. (2013). Data analysis for nanomaterials: Effective medium approximation, its limits and implementations. In *Ellipsometry at the Nanoscale* (pp. 145-178). Springer, Berlin, Heidelberg.
- ²¹¹ Aspnes, D. E., Theeten, J. B., & Hottier, F. (1979). Investigation of effective-medium models of microscopic surface roughness by spectroscopic ellipsometry. *Physical Review B*, 20(8), 3292.
- ²¹² Yamamoto, M., & Arai, A. (1993). In situ ellipsometry of soft X-ray multilayer fabrication. *Thin Solid Films*, 233(1-2), 268-271.
- ²¹³ Theeten, J. B. (1980). Real-time and spectroscopic ellipsometry of film growth: Application to multilayer systems in plasma and CVD processing of semiconductors. *Surface Science*, 96(1-3), 275-293.
- ²¹⁴ Jellison Jr, G. E. (1993). Data analysis for spectroscopic ellipsometry. *Thin Solid Films*, 234(1-2), 416-422.
- ²¹⁵ Tompkins, H. G., & Hilfiker, J. N. (2015). *Spectroscopic Ellipsometry: Practical Application to Thin Film Characterization*. Momentum Press.
- ²¹⁶ <https://www.jawoollam.com/resources/ellipsometry-tutorial>, last accessed on 10.02.2022.
- ²¹⁷ Fujiwara, H. (2007). *Spectroscopic ellipsometry: principles and applications*. John Wiley & Sons.
- ²¹⁸ <https://www.oharacorp.com/lic-gc.html>, last accessed on 10.02.2022.
- ²¹⁹ <https://www.biologic.net/products/vsp-300/>, last accessed on 14.02.2022.
- ²²⁰ Bondarenko, A. S. (2012). Analysis of large experimental datasets in electrochemical impedance spectroscopy. *Analytica Chimica Acta*, 743, 41-50.
- ²²¹ Bandarenka, A. S. (2013). Development of hybrid algorithms for EIS data fitting, a book chapter. In *Lecture Notes on Impedance Spectroscopy. Measurement, Modeling and Applications*; Kanoun, O., Ed.; CRC Press, Taylor and Francis Group: London, 2013; Vol. 4, pp 29–36.
- ²²² <https://el-cell.com/products/test-cells/standard-test-cells/pat-cell/>, last accessed on 15.02.2022.
- ²²³ Katzenmeier, L., Carstensen, L., Schaper, S. J., Müller-Buschbaum, P. & Bandarenka, A. S. (2021). Characterization and Quantification of Depletion and Accumulation Layers in Solid-State Li + -Conducting Electrolytes Using In Situ Spectroscopic Ellipsometry. *Advanced Materials*. 2100585.
- ²²⁴ Losurdo, M., Bergmair, M., Bruno, G., Cattelan, D., Cobet, C., De Martino, A., Fleischer, K., Dohcevic-Mitrovic, Z., Esser., & Saxl, O. (2009). Spectroscopic ellipsometry and polarimetry for materials and systems analysis at the nanometer scale: State-of-the-art, potential, and perspectives. *Journal of Nanoparticle Research*, 11(7), 1521–1554.

-
- ²²⁵ Ogieglo, W., Wormeester, H., Eichhorn, K. J., Wessling, M., & Benes, N. E. (2015). In situ ellipsometry studies on swelling of thin polymer films: A review. *Progress in polymer science*, *42*, 42-78.
- ²²⁶ Von Keudell, A., & Jacob, W. (1996). Growth and erosion of hydrocarbon films investigated by in situ ellipsometry. *Journal of Applied Physics*, *79*(2), 1092-1098.
- ²²⁷ Morata, A., Siller, V., Chiabrera, F., Nunez, M., Trocoli, R., Stchakovsky, M., & Tarancón, A. (2020). Operando probing of Li-insertion into LiMn₂O₄ cathodes by spectroscopic ellipsometry. *Journal of Materials Chemistry A*, *8*(23), 11538-11544.
- ²²⁸ Gorni, G., Balda, R., Fernández, J., Velázquez, J. J., Pascual, L., Mosa, J. & Castro, Y. (2018). 80SiO₂-20LaF₃ oxyfluoride glass ceramic coatings doped with Nd³⁺ for optical applications. *International Journal of Applied Glass Science*, *9*(2), 208-217.
- ²²⁹ Jaglarz, J., & Reben, M. (2010). The influence of nanocrystallization process on thermal and optical parameter in oxyfluoride glasses. *Optica Applicata*, *40*(2), 439.
- ²³⁰ Reben, M., Wasylak, J., & Jaglarz, J. (2010). Changes of refractive index of tellurite glass. *Photonics Letters of Poland*, *2*(1), 13-15.
- ²³¹ Katzenmeier, L., Helmer, S., Braxmeier, S., Knobbe, E., & Bandarenka, A. S. (2021). Properties of the Space Charge Layers Formed in Li-Ion Conducting Glass Ceramics. *ACS Applied Materials & Interfaces*, *13*(4), 5853-5860.
- ²³² Myland, J. C., & Oldham, K. B. (2000). Uncompensated resistance. 1. The effect of cell geometry. *Analytical chemistry*, *72*(17), 3972-3980.
- ²³³ Krasnikova, I. V., Pogosova, M. A., Sanin, A. O., & Stevenson, K. J. (2020). Toward Standardization of Electrochemical Impedance Spectroscopy Studies of Li-Ion Conductive Ceramics. *Chemistry of Materials*, *32*(6), 2232-2241.
- ²³⁴ Tsai, C. L., Dashjav, E., Hammer, E. M., Finsterbusch, M., Tietz, F., Uhlenbruck, S., & Buchkremer, H. P. (2015). High conductivity of mixed phase Al-substituted Li₇La₃Zr₂O₁₂. *Journal of electroceramics*, *35*(1), 25-32.
- ²³⁵ Breuer, S., Prutsch, D., Ma, Q., Epp, V., Preishuber-Pflügl, F., Tietz, F., & Wilkening, M. (2015). Separating bulk from grain boundary Li ion conductivity in the sol-gel prepared solid electrolyte Li_{1.5}Al_{0.5}Ti_{1.5}(PO₄)₃. *Journal of Materials Chemistry A*, *3*(42), 21343-21350.
- ²³⁶ Braun, P., Uhlmann, C., Weber, A., Störmer, H., Gerthsen, D., & Ivers-Tiffée, E. (2017). Separation of the bulk and grain boundary contributions to the total conductivity of solid lithium-ion conducting electrolytes. *Journal of Electroceramics*, *38*(2), 157-167.
- ²³⁷ Thokchom, J. S., Gupta, N., & Kumar, B. (2008). Superionic Conductivity in a Lithium Aluminum Germanium Phosphate Glass-Ceramic. *Journal of The Electrochemical Society*, *155*(12), A915.
- ²³⁸ Kahlaoui, R., Arbi, K., Sobrados, I., Jimenez, R., Sanz, J., & Ternane, R. (2017). Cation Miscibility and Lithium Mobility in NASICON Li_{1+x}Ti_{2-x}Sc_x(PO₄)₃ (0 ≤ x ≤ 0.5) Series: A Combined NMR and Impedance Study. *Inorganic Chemistry*, *56*(3), 1216-1224.

-
- ²³⁹ Chebotin, V. N., Remez, I. D., Solovieva, L. M., & Karpachev, S. V. (1984). Electrical double layer in solid electrolytes—theory: oxide electrolytes. *Electrochimica acta*, 29(10), 1380-1388.
- ²⁴⁰ Watzele, S. A., Katzenmeier, L., Sabawa, J. P., Garlyyev, B., & Bandarenka, A. S. (2021). Temperature dependences of the double layer capacitance of some solid/liquid and solid/solid electrified interfaces. An experimental study. *Electrochimica Acta*, 391, 138969.
- ²⁴¹ Katzenmeier, L., Carstensen, L., Bandarenka A.S. (2022). Li⁺ conductivity of space charge layers formed at electrified interfaces between a model solid-state electrolyte and blocking Au-electrodes. *ACS Applied Materials and Interfaces*, 14, accepted.
- ²⁴² Bosman, A. J., & Havinga, E. E. (1963). Temperature dependence of dielectric constants of cubic ionic compounds. *Physical Review*, 129(4), 1593.
- ²⁴³ Braga, M. H., Murchison, A. J., Ferreira, J. A., Singh, P., & Goodenough, J. B. (2016). Glass-amorphous alkali-ion solid electrolytes and their performance in symmetrical cells. *Energy & Environmental Science*, 9(3), 948-954.
- ²⁴⁴ Hamam, K. J., & Salman, F. (2019). Dielectric constant and electrical study of solid-state electrolyte lithium phosphate glasses. *Applied Physics A*, 125(9), 1-11.
- ²⁴⁵ Janek, R. P., Fawcett, W. R., & Ulman, A. (1997). Impedance spectroscopy of self-assembled monolayers on Au(111): Evidence for complex double-layer structure in aqueous NaClO₄ at the potential of zero charge. *Journal of Physical Chemistry B*, 101(42), 8550–8558.
- ²⁴⁶ Armstrong, R. D., & Horrocks, B. R. (1997). The double layer structure at the metal-solid electrolyte interface. *Solid State Ionics*, 94(1-4), 181-187.
- ²⁴⁷ Luo, J. (2015). Interfacial engineering of solid electrolytes. *Journal of Materiomics*, 1(1), 22-32.
- ²⁴⁸ Shukla, S., Seal, S., Vij, R., & Bandyopadhyay, S. (2003). Reduced activation energy for grain growth in nanocrystalline yttria-stabilized zirconia. *Nano letters*, 3(3), 397-401.
- ²⁴⁹ Schulz, M. (1993). Coulomb energy of traps in semiconductor space-charge regions. *Journal of applied physics*, 74(4), 2649-2657.
- ²⁵⁰ Xu, W., Williams, M. D., & Angell, C. A. (2002). Novel polyanionic solid electrolytes with weak coulomb traps and controllable caps and spacers. *Chemistry of materials*, 14(1), 401-409.
- ²⁵¹ Xu, W., & Angell, C. A. (2002). Preparation and characterization of novel “polyMOB” polyanionic solid electrolytes with weak coulomb traps. *Solid State Ionics*, 147(3-4), 295-301.
- ²⁵² Tang, W., Goh, B. M., Hu, M. Y., Wan, C., Tian, B., Deng, X. & Loh, K. P. (2016). In situ Raman and nuclear magnetic resonance study of trapped lithium in the solid electrolyte interface of reduced graphene oxide. *The Journal of Physical Chemistry C*, 120(5), 2600-2608.
- ²⁵³ Vyalikh, A., Schikora, M., Seipel, K. P., Weigler, M., Zschornak, M., Meutzner, F. & Meyer, D. C. (2019). NMR studies of Li mobility in NASICON-type glass-ceramic ionic conductors with optimized microstructure. *Journal of Materials Chemistry A*, 7(23), 13968-13977.

-
- ²⁵⁴ Kaye, M. (2021), Mott-Schottky Analysis of Solid-State Electrolytes, Department of Physics, TU Munich.
- ²⁵⁵ Dreyer, W., Guhlke, C., & Müller, R. (2013). Overcoming the shortcomings of the Nernst–Planck model. *Physical Chemistry Chemical Physics*, 15(19), 7075-7086.
- ²⁵⁶ Liu, Y., Bai, Y., Jaegermann, W., Hausbrand, R., & Xu, B. X. (2021). Impedance Modeling of Solid-State Electrolytes: Influence of the Contacted Space Charge Layer. *ACS Applied Materials & Interfaces*, 13(4), 5895-5906.
- ²⁵⁷ Teng, K. W., & Li, S. S. (1985). Theoretical calculations of Debye length, built-in potential and depletion layer width versus dopant density in a heavily doped pn junction diode. *Solid-State Electronics*, 28(3), 277-285.
- ²⁵⁸ Almond, D. P., & West, A. R. (1983). Mobile ion concentrations in solid electrolytes from an analysis of ac conductivity. *Solid State Ionics*, 9, 277-282.
- ²⁵⁹ Lee, E. J., & Pyun, S. I. (1992). Analysis of nonlinear Mott-Schottky plots obtained from anodically passivating amorphous and polycrystalline TiO₂ films. *Journal of Applied Electrochemistry*, 22(2), 156-160.
- ²⁶⁰ Park, G., Kim, H., Oh, J., Choi, Y., Ovchinnikova, O. S., Min, S. & Hong, S. (2021). Quantitative Measurement of Li-Ion Concentration and Diffusivity in Solid-State Electrolyte. *ACS Applied Energy Materials*, 4(1), 784-790.
- ²⁶¹ Lee, E., Prinz, F. B., & Cai, W. (2010). Kinetic Monte Carlo simulations of oxygen vacancy diffusion in a solid electrolyte: Computing the electrical impedance using the fluctuation–dissipation theorem. *Electrochemistry Communications*, 12(2), 223-226.
- ²⁶² Modak, A. U., & Lusk, M. T. (2005). Kinetic Monte Carlo simulation of a solid-oxide fuel cell: I. Open-circuit voltage and double layer structure. *Solid State Ionics*, 176(29-30), 2181-2191.
- ²⁶³ Wu, B., Wang, S., Lochala, J., Desrochers, D., Liu, B., Zhang, W. & Xiao, J. (2018). The role of the solid electrolyte interphase layer in preventing Li dendrite growth in solid-state batteries. *Energy & Environmental Science*, 11(7), 1803-1810.
- ²⁶⁴ Yang, Y. N., Jiang, F. L., Li, Y. Q., Wang, Z. X., & Zhang, T. (2021). A Surface Coordination Interphase Stabilizes a Solid-State Battery. *Angewandte Chemie International Edition*, 60(45), 24162-24170.
- ²⁶⁵ Cheng, D., Wynn, T. A., Wang, X., Wang, S., Zhang, M., Shimizu, R & Meng, Y. S. (2020). Unveiling the stable nature of the solid electrolyte interphase between lithium metal and LiPON via cryogenic electron microscopy. *Joule*, 4(11), 2484-2500.
- ²⁶⁶ Zhu, Y., Gonzalez-Rosillo, J. C., Balaish, M., Hood, Z. D., Kim, K. J., & Rupp, J. L. (2021). Lithium-film ceramics for solid-state lithionic devices. *Nature Reviews Materials*, 6(4), 313-331.